Towards entanglement detection in nanotube Cooper pair splitters with disorder and spin-orbit coupling

PhD Thesis

Morten Canth Hels

Academic advisors:
Jesper Nygård & Kasper Grove-Rasmussen

Center for Quantum Devices
Niels Bohr Institute
University of Copenhagen
October 31, 2017

This thesis has been submitted to the PhD School of The Faculty of Science, University of Copenhagen

Dansk resume

Denne afhandling præsenterer resultater fra eksperimentelle og teoretiske studier af kulstofnanorør (CNT) implementeret i kvantekredsløb og målt ved kryogene temperaturer. Specielt undersøges opsplitning af Cooper pair (CPS) i CNT kredsløb med stråledeler-geometri og en central superledende elektrode.

Kulstofnanorør er velegnede til brug i kvantekredsløb på grund af deres eksotiske elektroniske og mekaniske egenskaber. Ét forslag til anvendelse af kulstofnanorør udnytter deres indbyggede spin-bane kobling som et spin-filter til at demonstrere den sammenfiltrede karakter af opsplittende Cooper pair. Et sådant kredsløb ville have anvendelser inden for hardware til kvantecomputere som en kilde af sammenfiltrede elektroner.

En model til beskrivelse af CNT spektret udvides til at inkludere koblingen mellem langsgående niveauer i en CNT kvantedot. Udvidelsen forudsætter en generalisering af det elektrostatiske potentiale langs tuben. Vi viser, at modellen stemmer godt overens med data indsamlet fra transport i et to-terminalt CNT kvantedotkredsløb.

Et fremstillet CNT CPS kredsløb tillader identificering af ikke-lineare spin-bane magnetiske felter i de to dele af kredsløbet. Dette er muligt fordi det kurvede kulstofnanorør udviser lav urenhed gennem dets lave værdi af forholdet mellem KK' spredning og spin bane-kobling $\Delta_{KK'}/\Delta_{\mathrm{SO}}$. Sådanne spin-bane magnetiske felter blev tidligere betragtet som svære at opnå uden anvendelse af specielle fremstillingsteknikker. Vi opgiver detaljer til fremstilling af kredsløbet, men noterer, at udbyttet for denne proces var lavt. Motiveret af ovenstående resultater, udvikles en teori til beskrivelse af effekten af KK' spredning på gennemførbarheden af forslaget nævnt ovenfor til at detektere sammenfiltring af opsplittende Cooper par.

I det samme CNT CPS kredsløb analyseres transportdata for at uddrage bidragene fra processerne Cooper par opsplitning og elastisk cotunnelering til den samlede strøm. Det forhold, at det ikke-lokale konduktans-signal forsvinder i endeligt magnetfelt indikerer, at en del af transportmekanismen involverer den superledende elektrode. Derudover viser beregninger af Q parameteren, som er nødvendig i ovennævnte forslag, at en test af sammenfiltring er robust i forhold til falske positive resultater.

Det er attraktivt at kunne kontrollere elektrode-dot koblingerne i et CPS kredsløb, fordi de har betydning for CPS effektiviteten. Transportdata fra et nanotråds-CPS kredsløb med bundelektroder præsenteres. De viser, at en given elektrode-dot kobling kan indstilles af dens tilsvarende bundelektrode uden at påvirke de andre koblinger nævneværdigt. Koblingernes afhængighed af bundelektrodernes spænding konkluderes at være eksponentiel, hvilket er konsistent med forudsigelser fra grundlæggende kvanteteori.

Resultaterne i denne afhandling giver nye indsigter i at bruge kulstofnanorør i Cooper par splitter kredsløb og sammenfiltringsdetektions-eksperimenter.

Abstract

This thesis presents results from experimental and theoretical investigations of carbon nanotube (CNT) quantum devices at cryogenic temperatures. Specifically, Cooper pair splitting (CPS) in CNT devices with beam-splitter geometries and a central superconducting electrode is investigated.

Carbon nanotubes are attractive to use in quantum devices because of their exotic electronic and mechanical properties. One proposal involving carbon nanotubes utilizes their intrinsic spin-orbit interaction as a spin filter to demonstrate the entangled nature of splitting Cooper pairs. Such a device would have applications for quantum computing hardware as a source of entangled electrons.

A model for the CNT spectrum is extended to include the coupling between longitudinal levels in a CNT quantum dot. The extension requires a generalization of the electrostatic potential along the nanotube. The model is shown to have god correspondence with transport data obtained from a two-terminal CNT quantum dot device.

A CNT CPS device is fabricated which allows identification of non-collinear spin-orbit magnetic fields in the two segments of the device. This is made possible because the curved nanotube exhibits low disorder as measured by its ratio of KK' scattering to spin-orbit coupling $\Delta_{KK'}/\Delta_{\mathrm{SO}}$. The spin-orbit magnetic fields obtained in this device were previously considered to be difficult to obtain without using special fabrication techniques. We provide the details for fabrication of the device, but note that the yield for this process was low. Motivated by the results above theory is developed to describe the effect of KK' scattering on the viability of the proposal mentioned above to demonstrate entanglement of splitting Cooper pairs.

In the same CNT CPS device transport data is analyzed to extract the contributions from Cooper pair splitting and elastic cotunneling processes to the overall current. The vanishing of the nonlocal conductance signal with magnetic field indicates that part of the transport mechanism involves the superconducting electrode. Additionally, calculations of the Q parameter, which are required in the above proposal, show that the test of entanglement is robust against false positive results.

Control of the electrode-dot couplings in CPS devices is desirable for CPS devices since it impacts the CPS efficiency. Transport data from a bottom gated nanowire CPS device is presented showing that a given electrode-dot coupling can be tuned by its corresponding bottom gate while leaving the other couplings essentially constant. The dependence of the couplings on the voltage on the bottom gates is found to be exponential consistent with predictions from basic quantum theory.

Overall, the results in this thesis give new insights into using carbon nanotubes for Cooper pair splitter devices and entanglement detection experiments.

Acknowledgements

First of all I would like to thank my supervisors Jesper and Kasper. Jesper, it has been a privilege to work in such a well-equipped lab with so much ambition and progress. Experimental physics is hard, but it's a little less hard when you've got a bunch of top-notch equipment at your disposal. I also appreciate that I have had so much freedom to choose my own hours and do pet projects as I wanted.

Kasper, thank you for not getting tired of my endless barrage of questions during my first year. I took it entirely for granted that someone would show me the ropes as I was starting out, but I've since learned that that's a luxury. Thank you both for giving me some space during the frustrating parts of the project.

I'm happy to have worked with Anders Jellinggaard during my project. It was a real inspiration to see how much can be done with programming when it's done right (that is, done by Anders). Anders also coded the software framework that I used during my PhD and which simplified data acquisition immensely.

Top-notch equipment is only as good as the people maintaining it. Thankfully, QDev has outstanding technical staff who keep the machines running around the clock. Without Shivendra Upadhyay, Claus Sørensen, Nader Payami and Pétur Hermannsson this thesis would not have been possible. Additionally, I would like to thank Shivendra Upadhyay for countless delightful conversations, both the insightful and not-so-insightful ones.

When I first started in QDev I was fortunate to be put in an office with Thorvald Larsen, Christian Olsen and Jerome Mlack. Thank you for being awesome office-mates during my first year.

QDev would not be QDev without Charlie Marcus. It was always an inspiration to see what was going on in the other subgroups in the lab.

Jens Paaske could always be counted on to provide the theoretical perspective for my project. He also gave me my first teaching opportunities which helped me grow tremendously.

I thank Jess Martin for showing me the best side of American outgoingness. I was always inspired by how naturally she were able to tie the group together socially and I hope I get to work with her again sometime. From the administrative team I should also mention Gitte Michelsen who is a genius problem-solver. No matter the entangledness of the problems I showed up with she was always able to sort them out.

I much enjoyed sharing the good and bad times of my project with my friends Kasper, Thomas, Mia, Maher, Tine, Ian, Jose, Bastian and many others. In particular, these last eight years would have been dramatically different if I had not had Kasper to constantly bounce ideas off of. Thank you all for putting up with my bad jokes and stubborn ideas about driving in the left lane.

I would not have gotten so far without the support of my parents. You tell me that I was always an easy child. For my part I must say that you have been easy parents.

For always making me happy and taking my mind off physics I thank my girlfriend Helene.

Contents

List of Figures

List of Tables

Glossary

A4 4% 950PMMA A resist in anisole. Produced by MicroChem.

A6 6% 950PMMA A resist in anisole. Produced by MicroChem.

AC Alternating current

AJA AJA evaporation chamber. Manufactured by AJA International Inc.

CNT Carbon nanotube.

CPS Cooper pair splitting/splitter.

CSAR4 Resist AR-P 6200.04 produced by Allresist.

EL6 6% Copolymer resist in ethyl lactate. Produced by MicroChem.

IPA isopropanol, 2-propanol

MIKB methyl isobutyl ketone

Nanotube See CNT.

NMP *N*-methyl-2-pyrollidone, chemical used for lift-off of resist.

Normal metal A metal which is not superconducting in the temperature and pressure range typically used in mesoscopic physics: 1 mK-300 K and 1×10^{-10} mbar-1 bar. Examples include Au, Cr, Pd, Ti.

NW (semiconducting) nanowire.

PMMA poly(methyl methacrylate)

Switch A sudden change in electrostatic potential which causes electrical measurements to exhibit discontinuities.

Ultra-clean A CNT device is "ultra-clean" if no fabrication has been performed following the placement of the nanotube on the device electrodes. This technique was introduced in ref. [1].

ZEP520A Resist produced by Zeon Corporation.

Chapter 1

Introduction

As Moore's law [2, 3] is starting to fail due to fundamental constraints candidates are being considered as replacements for traditional silicon computing [4]. Quantum computing is one of these candidates [5, 6].

Classical computers come up short when dealing with problems of a certain size or complexity such as simulating superconductors or protein folding. A quantum computer replaces the classical bit with a qubit (quantum bit). By doing so it enables the use of new and faster algorithms that are capable of dealing with larger and more complex problems than are classical computers.

A key element in these algorithms is the entangled state and being able to reliably generate entangled states is key to building a quantum computer. Given two qubits and two states $|0\rangle$ and $|1\rangle$ an entangled state is one which can not be written as a product of two single-qubit states. For instance,

$$|\psi\rangle = |0\rangle\,|0\rangle + |1\rangle\,|1\rangle \tag{1.1}$$

is an entangled state because products of single-particle states $|\phi\rangle = |0\rangle + |1\rangle$ inevitably includes cross-terms like $|0\rangle\,|1\rangle$.

A natural source of entangled pairs is the superconducting condensate. Cooling some metals to cryogenic temperatures causes some of its conduction electrons to rearrange into so-called Cooper pairs. The electrons in the Cooper pairs have opposite momentum and spin. According to BCS theory [7, 8, 9], the state of a Cooper pair can be expressed as

$$|\psi\rangle_{\,\mathrm{BCS}} = u\,|0\rangle\,|0\rangle + v\,|\mathbf{k}\uparrow\rangle\,|-\mathbf{k}\downarrow\rangle\,, \tag{1.2}$$

that is, the states $|\mathbf{k}\uparrow\rangle$ and $|-\mathbf{k}\downarrow\rangle$ must be simultaneously occupied. A Cooper pair is an entangled state which is hinted at by the similarity of its state above with (1.1). If the Cooper pair can be split into its constituent electrons we have, in principle, our entangled state.

In a quantum dot electrons are made to tunnel one-by-one through a constricted region by utilizing their mutual repulsion. A Cooper pair is not allowed in quantum dots because of this repulsion. Thus, if the Cooper

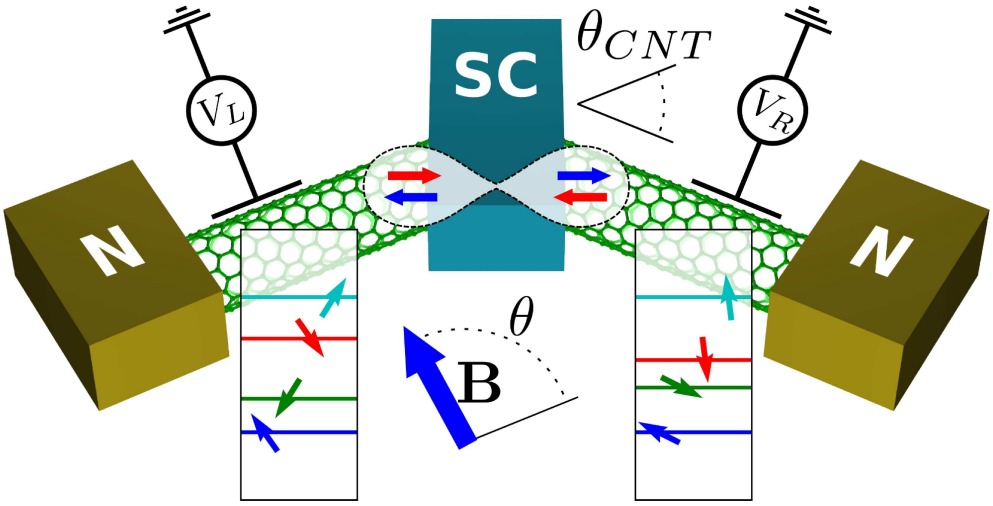

Figure 1.1: A schematic of the Braunecker proposal [10]. Cooper pairs are ejected from a central superconductor (SC) and cause a nonlocal current in the two nanotube quantum dots. The current depends on the overlap between the spin of the Cooper pair electrons (horizontal arrows) and the spin of the nanotube states (slanted arrows). Measuring the current for all 16 combinations of the states in the nanotube segments reveals whether the particles responsible for the current are entangled. In order to obtain dissimilar splittings of the levels in the two nanotube segments the nanotubes must be at an angle.

pair electrons were to leave the superconductor through a quantum dot they would have to separate and tunnel through different dots. Figure 1.1 shows this situation where carbon nanotubes play the role as quantum dots.

Experiments of this type have already been done by measuring a correlation in current between the two quantum dots. Also, Cooper pair splitting (CPS) in both carbon nanotubes [11, 12] and nanowires [13, 14, 15] has been demonstrated. What remains to be seen is that the electrons are actually entangled when they leave the superconductor.

This question is addressed in the proposal by Braunecker et al. [10] shown schematically in Figure 1.1. The idea is to use a curved carbon nanotube with spin-orbit coupling as spin-filters so that the current is suppressed for certain filter configurations. For instance, splitting a Cooper pair through two spin-up states in the nanotubes should yield a lower current than splitting it through states with opposite spin. This type of correlation test is called a Bell test. Carbon nanotubes are especially well suited for this purpose since the coupling between spin and orbital motion gives rise to a built-in magnetic field oriented parallel to the tube axis. When an external magnetic field is applied we can calculate the spin direction of the states in the nanotube and

orient the "filter" as we choose, thus enabling us to do controlled correlation measurements. It is essential the the nanotubes are at an angle so that their built-in magnetic fields are non-collinear.

We can sum up the requirements for the Braunecker proposal as follows:

1. The states in the carbon nanotube should be identifiable, that is, the quantum dot should exhibit four-fold periodicity.

2. A superconducting gap must be present in a bias spectroscopy plot to indicate that the central lead is superconducting.

3. The critical magnetic field B_{C} of the superconductor must not be much lower than the spin-orbit magnetic field. Otherwise the superconductor will be made normal before the field can appreciably alter the nanotube spectrum at a value of about $B \sim B_{\mathrm{SO}}$.

4. In order to have reasonably well-defined spin states we require that spin-orbit interaction dominates disorder: $\Delta_{\mathrm{SO}} > \Delta_{KK'}$.

5. The spin-orbit magnetic fields must not be parallel to ensure that the spin bases are not parallel. Consequently, the nanotube segments themselves must be at an angle.

6. Finally, the current should exhibit nonlocal correlations in a specific pattern.

Several of the requirements above have already been demonstrated previously in separate devices. Carbon nanotubes quantum dots exhibiting four-fold symmetry and with superconducting gaps are common and were first observed in [16]. Getting a high critical magnetic field is a matter of choosing the right material or making the superconducting film thin. Spin-orbit dominated nanotubes have been demonstrated in so-called "ultraclean" devices [17], but also in a regular "non-clean" device [18]. Some bent (or kinked) nanotubes have been measured previously, e.g. in ref. [19]. Cooper pair splitting has only been demonstrated recently [13, 11] and is a topic of current research [12, 14, 15, 20].

In this thesis we investigate experimentally and theoretically carbon nanotube quantum dot devices in various geometries with an emphasis on their utility for entanglement detection.

1.1 Outline of this thesis

The outline of this thesis is as follows

Chapter 2 describes basic theory on carbon nanotubes, quantum dots and superconductivity. We focus in particular on the spectrum of carbon

nanotubes and transport mechanisms in quantum dots. Bringing all of the above together the chapter closes with transport in hybrid normal metal-superconductor systems and the Cooper pair splitter geometry.

Chapter 3 outlines the experimental methods employed in this work which include nanofabrication and cryogenic electronic measurements. Note that the appendices contain additional, detailed information on, e.g., fabrication parameters and tricks, lock-in measurements, and data modeling and visualization.

Chapter 4 presents an analysis of a carbon nanotube quantum dot. Transport through the dot is measured at high magnetic fields which allows the hybridization of the nanotube shells to be observed and modelled. The insights gained in this study advance the understanding of the carbon nanotube spectrum. This understanding is important for realizing proposals such as the entanglement detection experiment.

Chapter 5 contains the central results in this thesis. We show that the requirements in the Braunecker proposal can realistically be satisfied in a carbon nanotube device processed with conventional methods. In addition, we analyze the effect of KK' scattering on the feasibility of the entanglement detection experiment. The results show that entanglement detection can be achieved with a finite amount of disorder.

Chapter 6 builds on the preceding chapter by analyzing nonlocal signals in the same device. The evolution of these signals with magnetic field indicates that they are, indeed, caused by splitting Cooper pairs. Calculations on experimental data indicate that the Q parameter is robust against false positive detection.

Chapter 7 shows that full control of the electrode-dot couplings can be achieved in a bottom gated nanowire device. The dependence of these couplings with the voltage applied to the bottom gates is exponential as predicted by basic quantum theory.

This PhD thesis is written as part of the so-called "integrated" (4+4) PhD program. Thus, some of the material presented in this thesis also appears in the author's master thesis (reference [21]). Specifically, Chapter 1, sections 2.1, 2.2, Chapter 3, the experimental data in Chapter 5 and Chapter A appear in the author's master thesis in shorter forms as material has been added in the present thesis. We note that this practice is consistent with the spirit and regulations of the integrated PhD program.

1.2 Publications

The work described in this thesis has resulted in the following publications

- M. C. Hels, K. Grove-Rasmussen, T. S. Jespersen, and J. Nygård, *to be submitted in Physical Review B.* Chapter 4.

- M. C. Hels, B. Braunecker, K. Grove-Rasmussen, and J. Nygård. Non-collinear spin-orbit magnetic fields in a carbon nanotube double quantum dot. Phys. Rev. Lett., 117:276802, Dec 2016. Reference [22]. Chapter 5.

- M. Kühnel, M. Overgaard, M. C. Hels, T. Vosch, B. W. Laursen and K. Nørgaard, *to be submitted* [23]. The manuscript is not included in this thesis.

Chapter 2

Theory

2.1 Carbon Nanotubes

In this section we present an overview of the electronic structure of carbon nanotubes. Focus will be on the effects that will be discussed in the data which means that, e.g., strain and torsion effects will not be considered. A more complete treatment can be found in [24] which also serves as inspiration for the present section.

2.1.1 Physical Structure

A carbon nanotube (CNT) is a cylinder made of carbon atoms bonded in a hexagonal structure.

For analyzing both physical and electronic properties the nanotube can be thought of as a rolled-up graphene sheet as shown in Figure 2.1. The graphene unit cell consists of two inequivalent carbon atoms, A and B. The translation vectors are $\mathbf{a}_1$ and $\mathbf{a}_2$. We can form a cylinder from the sheet by defining the chiral vector

$$\mathbf{C}_h = n\mathbf{a}_1 + m\mathbf{a}_2 \tag{2.1}$$

and rolling the sheet along it until the start and end points of the chiral vector touch. Examples of the resulting cylinder are shown in Figure 2.2. In the general case the tube will be chiral so that its mirror image represents a different structure which can not be obtained from rotation. Using the short-hand notation $\mathbf{C}_h = (n, m)$ we see that two cases have a special symmetry: $(n, 0)$ (zig-zag) and (n, n) (arm-chair). These tubes are non-chiral, i.e., mirroring yields an equivalent structure.

The angle θ between a_1 and the chiral vector $\mathbf{C}_h$ is important for the properties of the CNT. It is given by

$$\cos\theta = \frac{\mathbf{C}_h \cdot \mathbf{a}_1}{|\mathbf{C}_h||\mathbf{a}_1|} = \frac{2a + b}{2\sqrt{a^2 + ab + b^2}} \tag{2.2}$$

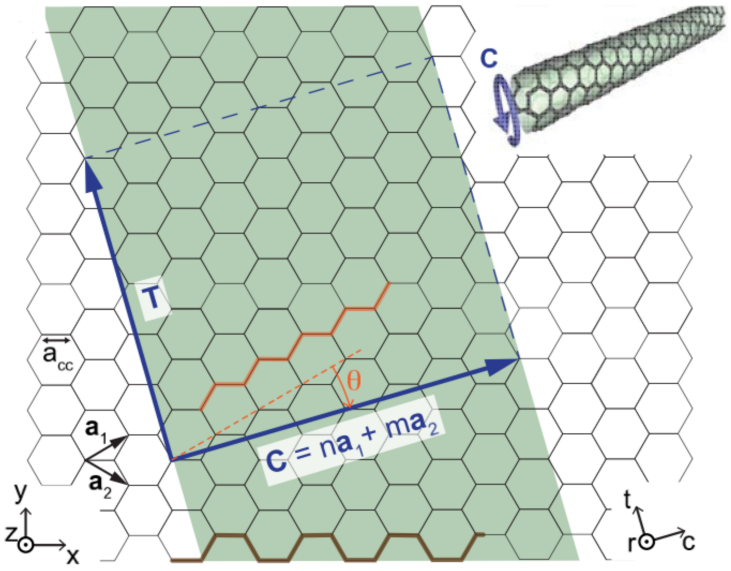

Figure 2.1: A nanotube is obtained from a sheet of graphene by "rolling" the sheet along **C**. The area defined by the **T** and **C** vectors define the surface of the nanotube. The chiral vector **C** determines various properties of the nanotube through the angle θ. Since a nanotube exhibits cylindrical symmetry the graphene coordinates x, y, z are transformed into t, r, c coordinates for the nanotube, denoting the axial, radial and circumferential direction, respectively. Figure adapted from [25, 26, 27]

For the zig-zag and armchair structures $\theta = 0°$ and $30°$, respectively.

In graphene the distance between nearest neighbors $a_{\mathrm{CC}} = 0.142\,\mathrm{nm}$. The diameter D of the CNT can be calculated with

$$D = \frac{\sqrt{3}a_{\mathrm{CC}}}{\pi}\sqrt{a^2 + ab + b^2} \tag{2.3}$$

which also equals $|\mathbf{C}_h|/\pi$. Typical nanotube diameters are 1 nm to 6 nm.

2.1.2 Electronic Structure

The starting point for the CNT band structure is the graphene spectrum which we'll review first, before going into the corrections necessary for nanotubes. The important part of the graphene spectrum are the Dirac cones which are located at the Dirac points $\mathbf{K}, \mathbf{K}' = (0, \mp)4\pi/3a_{\mathrm{CC}}$. The Dirac points **K** and **K′** are a time-reversed pair, so by Kramers' theorem they must have the same energy as long as time-reversal symmetry is not broken. Near the Dirac points the dispersion is approximately linear so with E_{F} as the zero-point of energy and measuring $\boldsymbol{\kappa}$ from a Dirac point we can write

$$E = \pm\hbar v_{\mathrm{F}}|\boldsymbol{\kappa}|. \tag{2.4}$$

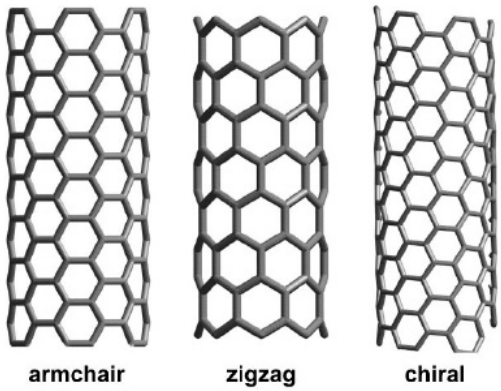

Figure 2.2: The chiral vector $\mathbf{C}_h$ defines the chirality of the CNT as either armchair, zigzag or chiral. Armchair: $\mathbf{C}_h = (n, n)$, zigzag: $\mathbf{C}_h = (n, 0)$. All other vectors give chiral nanotubes. Adapted from [28].

Here v_F is the Fermi velocity of graphite which is about $8 \times 10^5\,\mathrm{m/s}$.

For the purposes of this thesis we consider the following perturbations to the graphene spectrum:

1. Quantization of the circumferential k-component $k_\perp$ which confines the spectrum to lines in the graphene spectrum.
2. Curvature-induced shift of the Dirac cones.
3. Application of an external magnetic field.
4. Spin-orbit coupling between the spin of an electron and its motion around the nanotube.
5. A disorder term $\Delta_{KK'}$ which mixes the circumferential modes K and K'.

Quantization of $k_\perp$ Rolling up a graphene sheet puts restrictions on $k_\perp$ which is unrestricted in graphene. For the wave function to be single-valued we require that it does not change its value upon completing one revolution around the nanotube:

$$\exp(i\mathbf{kr}) = \exp(i\mathbf{k}(\mathbf{r} + \mathbf{C})) \Rightarrow \mathbf{k} \cdot \mathbf{C} = 2\pi p \Rightarrow k_\perp = 2p/D \qquad (2.5)$$

where p is an integer. Restricting $k_\perp$ in this way yields a spectrum consisting of line cuts through the graphene spectrum as shown in Figure 2.3.

Depending on whether the cuts miss the Dirac points or pass through them the low-energy dispersion will be either linear or hyperbolic. In the latter case a gap opens up since the conduction and valence bands don't touch at $|\kappa_\parallel| = 0$. When $k_\perp$ is quantized the dispersion takes the form

$$E = \pm\sqrt{\hbar^2 v_\mathrm{F}^2 \kappa_\parallel^2 + E_\mathrm{G}^2/4} \qquad (2.6)$$

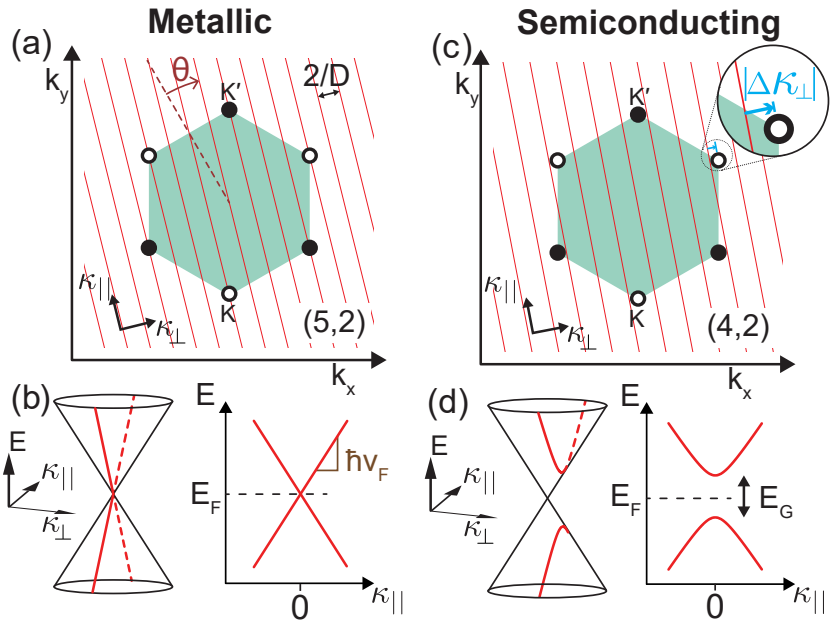

Figure 2.3: **(a), (c)** By quantizing the wave number $k_\perp$ around the nanotube circumference the 1D dispersion of a nanotube is obtained as shown in **(b), (d)**. If the red quantization lines pass through a Dirac point (circles) the nanotube is nominally metallic, while a band gap E_G opens in the opposite case. Figure adapted from [24].

Metallic nanotubes have linear dispersions and are gapless while semiconducting nanotubes have hyperbolic dispersions and show gaps of

$$E_\mathrm{G} = 4\hbar v_\mathrm{F}/3D \approx 700\,\mathrm{meV}/D[\mathrm{nm}]. \tag{2.7}$$

Anticipating its use for quantum dots we replace $\hbar v_\mathrm{F}\kappa_\parallel$ in (2.6) by the confinement energy E_conf:

$$E = \pm\sqrt{E_\mathrm{conf}^2 + E_\mathrm{G}^2/4} \tag{2.8}$$

In quantum dots the longitudinal motion is confined which leads to quantized values for $\kappa_\parallel$ and hence E_conf. States that have the same E_conf are said to belong to the same shell.

In Figure 2.3 we see that a quantization line that passes close to a **K** point will also pass close to a **K′** point in the same distance. The states on these lines close to the **K** and **K′** points constitute the low-energy dispersion. It is convenient to classify them as K or K' states according to which type of point they are close to. This enables us to make the intuitive interpretation that K and K' states in the same band (conduction or valence) circulate the nanotube in opposite directions because they are time-reversal conjugates. The direction of circulation is opposite for states in the conduction and valence bands since $v_\perp \propto \partial E/\partial k_\perp$ has opposite signs in the conduction and valence bands.

The K and K' points are collectively known as the *valley* quantum number. We'll use $\tau = \pm 1$ to refer to the valley quantum number where $\tau = +1$ (-1) corresponds to K (K').

The K states are time-reversed partners of the K' states so they are degenerate when time-reversal symmetry is not broken. This makes the total degeneracy in nanotubes equal to four since the states are also spin-degenerate.

Curvature-induced displacement of Dirac cones Another consequence of rolling up a graphene sheet is that the orbital overlaps of the carbon atoms change. This displaces the Dirac cones by a vector $\mathbf{\Delta}\kappa^{\mathrm{cv}}$ which is opposite for K and K'. In some metallic nanotubes this displacement causes the quantization line to no longer go through the Dirac points. These nanotubes are thus no longer gapless but exhibit gaps of [24]

$$E_{\mathrm{G}}^{\mathrm{cv}} = 2\hbar v_{\mathrm{F}} |\Delta\kappa_{\perp}^{\mathrm{cv}}| \tag{2.9}$$

where the cv superscript stands for curvature. Nanotubes that change character in this way are called narrow-gap nanotubes. The magnitude of the curvature band gap is about

$$E_{\mathrm{G}}^{\mathrm{cv}} \sim \frac{50\,\mathrm{meV}}{D[\mathrm{nm}]^2} \cos 3\theta \tag{2.10}$$

which is always smaller than the quantization band gap in (2.7) so that semiconducting nanotubes remain semiconducting. Armchair nanotubes remain metallic with the curvature perturbation since in their case $\mathbf{\Delta}\kappa^{\mathrm{cv}}$ is parallel to the quantization lines and $k_{\perp}^{\mathrm{cv}} = 0$.

Behavior in Magnetic Fields A magnetic field interacts with an electron orbiting a CNT in two ways: By coupling to the electron spin (Zeeman effect) and by coupling to the circumferential motion around the nanotube.

The Zeeman energy in a magnetic field oriented parallel to the nanotube axis is

$$E_{\mathrm{Z}} = \frac{1}{2} g_{\mathrm{s}} \mu_{\mathrm{B}} s B_{\parallel} \tag{2.11}$$

where $s = \pm 1$ denotes spin parallel or anti-parallel to the nanotube axis.

To find the energy of the coupling between the circumferential motion and the magnetic field we use the following classical argument: The nanotube cross-section has an area $A = \pi D^2/4$ and the electron carries a current $I = |e| v_{\mathrm{F}}/\pi D$ by orbiting the tube. This gives for the magnitude of the orbital magnetic moment

$$\mu_{\mathrm{orb}} = IA = |e| \frac{v_{\mathrm{F}}}{\pi D} \cdot \pi D^2/4 = |e| v_{\mathrm{F}} D/4. \tag{2.12}$$

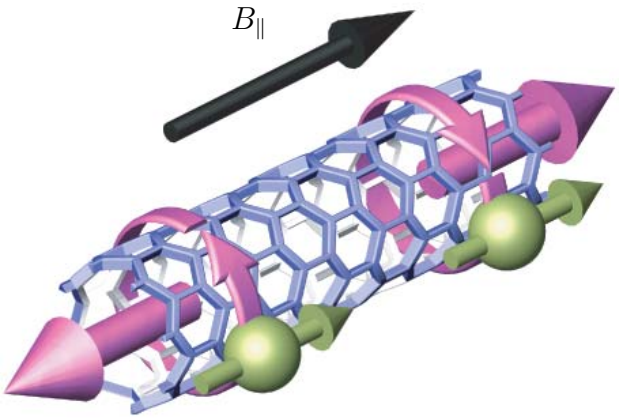

Figure 2.4: Schematic showing orbital angular momentum (purple), spin angular momentum (green) and applied $B_\parallel$-field. Adapted from [17].

To obtain the orbital magnetic moment for a specific state we multiply by τ which determines the direction of circulation. Applying a magnetic field parallel $B_\parallel$ as in Figure 2.4 thus increases the energy of the electron by

$$E_{\text{orb}} = \mp\tau\mu_{\text{orb}}B_\parallel. \tag{2.13}$$

where the minus (plus) is for the conduction (valence) band. This equation fixes our convention regarding valley interaction with a magnetic field: K states ($\tau = +1$) in the conduction band *decrease* in energy with *increasing* parallel magnetic field. By defining an orbital g-factor[1]

$$g_{\text{orb}} = \mu_{\text{orb}}/\mu_{\text{B}} = \frac{1}{4}Dev_{\text{F}} \approx 3.5 \times D[\text{nm}] \tag{2.14}$$

we can write

$$E_{\text{orb}} = \mp\tau g_{\text{orb}}\mu_{\text{B}}B_\parallel \tag{2.15}$$

so that the total energy E_{mag} due to a parallel magnetic field is given by

$$E_{\text{mag}} = E_{\text{Z}} + E_{\text{orb}} = (sg_{\text{s}} \mp \tau g_{\text{orb}})\mu_{\text{B}}B_\parallel. \tag{2.16}$$

A rigorous derivation of the orbital interaction involves the Aharonov-Bohm flux through the nanotube cross section. The result obtained in this way is the same as the one above, though.

In a magnetic field with arbitrary orientation the spin-up and spin-down states are mixed by the perpendicular field, but only within a valley.

The nanotube spectrum as a function of perpendicular and parallel magnetic field is shown in Figure 2.5. In a parallel field sg_{s} and τg_{orb} add to give four slopes. Two doubly-degenerate lines are visible for a perpendicular field because it does not break the valley degeneracy.

[1] Sometimes g_{orb} is defined as $g_{\text{orb}} = 2\mu_{\text{orb}}/\mu_{\text{B}}$ so that we get the same factor of 1/2 as in (2.11) in the expression for E_{orb}.

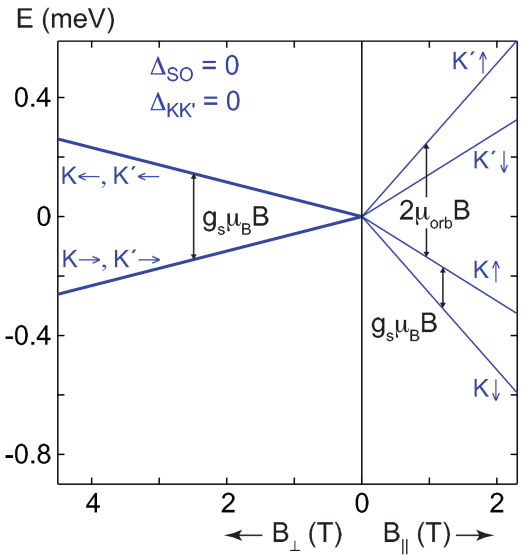

Figure 2.5: Nanotube spectrum without spin-orbit coupling or disorder effects. In a parallel magnetic field the states split up according to their combined g-factor $sg_s \mp \tau g_{orb}$. A perpendicular field only affects the spin because the orbital motion is perpendicular to the field. Figure adapted from [24].

Spin-orbit Coupling The interaction between the spin of an electron and the orbit in which it moves is called spin-orbit coupling. For instance, an electron moving with velocity $\mathbf{v}$ in the electric field $\mathbf{E}$ of an atomic nucleus will experience a magnetic field

$$\mathbf{B} = -\frac{1}{c^2}(\mathbf{v} \times \mathbf{E}). \tag{2.17}$$

This magnetic field then couples with the electron spin. For this electron the "orbit" in spin-orbit coupling is an actual orbit around the atomic nucleus.

In carbon nanotubes the "orbit" is the motion around the circumference of the tube. In cylindrical coordinates this motion is in the azimuthal direction while the average electric field from the nanotube atoms is in the radial direction for symmetry reasons. Thus, an electron orbiting a nanotube experiences a magnetic field which is directed parallel to the nanotube axis. This property is important for the Braunecker proposal.

A closer theoretical treatment reveals that there are two types of spin-orbit coupling in carbon nanotubes: A Zeeman-like contribution which shifts the Dirac cones up or down by an amount

$$\Delta E^{\mathrm{SO,Z}}(\tau, s) = \Delta^0_{\mathrm{SO}} \tau s, \tag{2.18}$$

and an orbital-like contribution which shifts the Dirac cones horizontally by

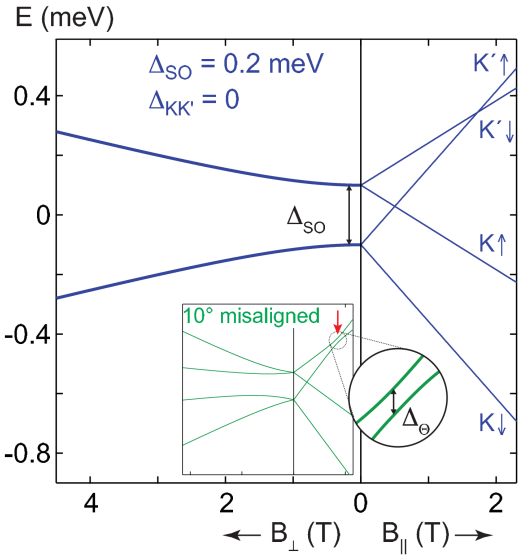

Figure 2.6: Nanotube spectrum including spin-orbit interaction. The nanotube states split according to their combined g-factor as before, but the spin-orbit coupling now acts to align orbital and spin magnetic moments, even at zero field. The zero-field splitting Δ_{SO} motivates the definition of a spin-orbit magnetic field $B_{\mathrm{SO}} = \Delta_{\mathrm{SO}}/g_{\mathrm{s}}\mu_{\mathrm{B}}$. By slanting the magnetic field away from parallel spin-up and spin-down states are mixed as shown by the anti-crossing in the inset. Figure adapted from [24].

an amount

$$\Delta\kappa_{\perp}^{\mathrm{SO,orb}}(s) = -s\frac{\Delta_{\mathrm{SO}}^{1}}{\hbar v_{\mathrm{F}}}. \tag{2.19}$$

The Zeeman-like term is simply added to the Hamiltonian while the orbital-like contribution is added to the curvature shift of the Dirac cones.

At zero magnetic field with only spin-orbit coupling present the splitting of the four states is given by

$$\Delta_{\mathrm{SO}} \equiv 2\left(\Delta_{\mathrm{SO}}^{0} \mp \Delta_{\mathrm{SO}}^{1}\frac{g_{\mathrm{orb}}}{g_{\mathrm{orb}}^{0}}\right). \tag{2.20}$$

The data presented in this thesis does not allow distinguishing the two types of spin-orbit coupling so we will be using only the Δ_{SO} parameter. We can also define a spin-orbit magnetic field $\mathbf{B}_{\mathrm{SO}}$ by taking Δ_{SO} as the Zeeman splitting of this field:

$$\Delta_{\mathrm{SO}} = g_{\mathrm{s}}\mu_{\mathrm{B}}B_{\mathrm{SO}} \Rightarrow B_{\mathrm{SO}} = \frac{\Delta_{\mathrm{SO}}}{g_{\mathrm{s}}\mu_{\mathrm{B}}}. \tag{2.21}$$

The spin-orbit magnetic field is directed along the axis of the nanotube.

Figure 2.6 shows the spectrum with spin-orbit coupling included. Comparing to Figure 2.5 we see the zero-field degeneracy of 4 is split into 2: a

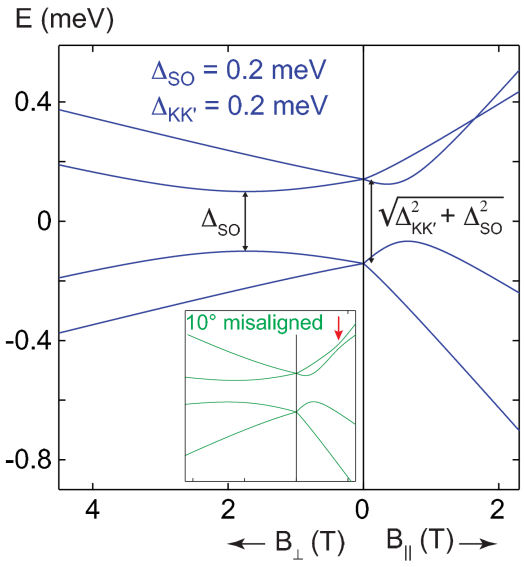

Figure 2.7: Nanotube spectrum including both spin-orbit coupling and disorder. Neither spin nor valley are good quantum numbers if spin-orbit and disorder effects are taken into account. Disorder $\Delta_{KK'}$ causes an anti-crossing of the $K'\uparrow$ and $K\downarrow$ states and also contributes to the zero-field splitting. Figure adapted from [24].

pair which has spin and orbital magnetic moments aligned ($K'\uparrow$ and $K\downarrow$) and one that has them anti-aligned. The slopes are the same as before.

Note that the state labels have been removed from the perpendicular part of the spectrum because valley and spin are not good quantum numbers in this case.

The inset shows how misaligning the magnetic field relative to the nanotube axis changes the spectrum. A considerable change is seen in the perpendicular part since the magnetic field now also couples to the orbital motion. For a parallel field the $K'\downarrow$ and $K'\uparrow$ states exhibit an anti-crossing due to their spins being mixed. This gap has a magnitude

$$\Delta_\Theta = |\Delta_{SO}| \tan\Theta \tag{2.22}$$

where Θ is the misalignment angle.

Disorder in the nanotube Impurities and dislocations are included in the spectrum by a disorder term $\Delta_{KK'}$ which mixes K and K' states with the same spin. It is a phenomenological parameter that is not derived from first principles. Figure 2.7 shows the spectrum with both spin-orbit coupling and disorder. The crossing of the $K\uparrow$ and $K'\uparrow$ states is now an anti-crossing due to K and K' being mixed. Neither spin nor valley are good quantum numbers.

The complete Hamiltonian Combining the contributions above involves setting up a Hamiltonian in $A-B$ subspace[2] for parallel magnetic field and without disorder and diagonalizing it. While it does provide some physical insight it is outside the scope of this thesis. We simply give the result in the approximation

$$E_{\mathrm{G}}^{0} \gg |\Delta_{\mathrm{SO}}^{1}|, \mu_{\mathrm{orb}}^{0}|B_{\parallel}| \tag{2.23}$$

where μ_{orb}^{0} is the orbital magnetic moment of the (electron or hole) shell closest to the band gap. This is justified for typical semiconducting and narrow-gap nanotubes. It does not hold for true metallic nanotubes, though, since they have no band gap.

We will use the definition

$$E_{\tau,s}^{\pm} \approx E_{0}^{\pm} + s\tau\frac{\Delta_{\mathrm{SO}}}{2} + \left(\mp\tau g_{\mathrm{orb}} + \frac{1}{2}sg_{\mathrm{s}}\right)\mu_{\mathrm{B}}B_{\parallel} \tag{2.24}$$

where

$$E_{0}^{\pm} = \pm\sqrt{E_{\mathrm{conf}}^{2} + (E_{\mathrm{G}}^{0})^{2}/4} \tag{2.25}$$

and E_{G}^{0} is the combined quantization and curvature band gap. The magnetic field is expressed as

$$\mathbf{B} = (B_{\parallel}, B_{\perp}) = B(\cos\theta, \sin\theta) \tag{2.26}$$

where θ is the angle between the nanotube axis and the magnetic field. In the basis $(K\uparrow, K'\downarrow, K\downarrow, K'\uparrow)$ we end up with

$$\begin{aligned} H = &\begin{pmatrix} E_{1,1}^{\pm} & 0 & 0 & \Delta_{KK'}/2 \\ 0 & E_{-1,-1}^{\pm} & \Delta_{KK'}/2 & 0 \\ 0 & \Delta_{KK'}/2 & E_{1,-1}^{\pm} & 0 \\ \Delta_{KK'}/2 & 0 & 0 & E_{-1,1}^{\pm} \end{pmatrix} \\ &+\frac{1}{2}g_{\mathrm{s}}\mu_{\mathrm{B}}B\begin{pmatrix} 0 & 0 & \sin\theta & 0 \\ 0 & 0 & 0 & \sin\theta \\ \sin\theta & 0 & 0 & 0 \\ 0 & \sin\theta & 0 & 0 \end{pmatrix}. \end{aligned} \tag{2.27}$$

Note that in this basis the Hamiltonian is diagonal if no perpendicular magnetic field is applied and no disorder is present. In this case the energies can simply be obtained from (2.24).

The $E_{0}^{\pm}$ term does not change within a shell. If we define this quantity as the zero of energy for a given shell we should be able to reproduce its spectrum using only the parameters $\Delta_{\mathrm{SO}}, g_{\mathrm{orb}}$, $\Delta_{KK'}$ and the angle of the nanotube axis.

For the $N=2$ state electron-electron interactions can be included which are sometimes important. Hence, the $N=2$ states include an additional parameter J for the exchange coupling. We will not discuss the spectrum for $N=2$ states here, but refer to [29].

[2] Recall that the graphene unit cell contains two inequivalent carbon atoms, A and B.

2.2 Quantum Dots

In this section we will briefly review the basics of quantum dots before describing cotunneling processes in more detail. The latter will play an important role for data analysis in chapters 5 and 4. For a more in-depth treatment of quantum dots we refer to [30].

2.2.1 Quantum dot basics

A quantum dot consists of a microscopic region typically of the order of hundreds of nanometers in which electrons are confined by potential barriers. Two requirements are made of the barriers: They must be high enough that the number of electrons is a good quantum number and they must not be so high as to prevent tunneling altogether.

In the following we will use the constant interaction model for the quantum dot. The energy of the quantum dot E is determined by the number of electrons on the dot N, the voltages and capacitances of nearby gates V_i, C_i and the energies of the quantum mechanical levels ϵ_i

$$E = \frac{1}{2C}\left(-|e|(N - N_0) + \sum_i C_i V_i\right)^2 + \sum_i^N \epsilon_i \tag{2.28}$$

where C is the self-capacitance of the dot, typically approximated by $C = \sum_i C_i$.

Using E we can get an expression for the addition energy E_{add}, i.e., the energy for adding an electron given N electrons already on the dot:

$$\begin{aligned} E_{\text{add}} &= \mu_{N+1} - \mu_N = (E_{N+1} - E_N) - (E_N - E_{N-1}) \\ &= \frac{e^2}{C} + \Delta E \equiv U + \Delta E \end{aligned} \tag{2.29}$$

where μ_N is the chemical potential for adding the N'th electron. The charging energy U and the level spacing ΔE are key quantities for the quantum dot.

We can approximate these quantities specifically for a nanotube: The capacitance should be linear in L if the nanotube is much longer than it is wide. Thus, the charging energy can be estimated for a nanotube of length L by making the crude assumption

$$C \approx \epsilon_0 \epsilon_{\text{r}} L \tag{2.30}$$

so that

$$U \approx \frac{e^2}{\epsilon_0 \epsilon_{\text{r}} L} \approx \frac{4.5\,\text{meV}}{L[\mu\text{m}]}. \tag{2.31}$$

where we have used the SiO_2 value for ϵ_r of 4.

The level spacing is only added to the charging energy when a longitudinal level in the dot is filled. In the simplest case the energy of the longitudinal levels is simply given by a particle-in-a-box calculation. Taking $E(k_\parallel) = \hbar v_F k_\parallel$ for a Dirac cone and $k_{\parallel,n} = n\pi/L$ for a 1D particle in a box with hard-wall boundary conditions we get

$$\Delta E = \hbar v_F (k_{\parallel,n} - k_{\parallel,n-1}) = \frac{h v_F}{2L} \approx \frac{1.7\,\mathrm{eV}}{L[\mu\mathrm{m}]} \tag{2.32}$$

Longitudinal levels are often called shells to emphasize the similarity between quantum dots and atoms. As discussed in the previous section carbon nanotube shells are four-fold degenerate in contrast to most other systems (e.g., nanowires,2-dimensional electron gases etc.) which only exhibit two-fold degeneracy.

2.2.2 Transport in a quantum dot

To describe transport through the quantum dot we define the Hamiltonian H for the system consisting of a dot and two metal leads

$$H = H_D + H_L + H_R + H_T \tag{2.33}$$

where the first three terms determine the energy levels of the dot and the left and right leads. We denote this non-interacting part of the Hamiltonian by H_0. The last term is the transfer term which transfers electrons between the leads and dot. It can be split into parts concerning either lead

$$H_T = H_{TL} + H_{TR} \tag{2.34}$$

Transport through the quantum dot can be described by using a transfer matrix T which is given self-consistently as [31]

$$T = H_T + H_T \frac{1}{E_i - H_0} T \tag{2.35}$$

where E_i is the energy of the initial state.

The transition rate of electrons $\Gamma_{\beta\alpha}$ from state α to state β is then given by

$$\Gamma_{\beta\alpha} = \frac{2\pi}{\hbar} \left|\langle\beta| T |\alpha\rangle\right|^2 \delta(E_\beta - E_\alpha) \tag{2.36}$$

where the delta function δ ensures energy conservation. Sequential tunneling is the first-order contribution to this rate. Take, for instance, the first-order term of the rate for the transition between α and β which moves one electron from the left lead onto the dot:

$$\Gamma^{1st,L}_{\beta\alpha} = \frac{2\pi}{\hbar} \left|\langle\beta| H_{TL} |\alpha\rangle\right|^2 \delta(E_\beta - E_\alpha) \tag{2.37}$$

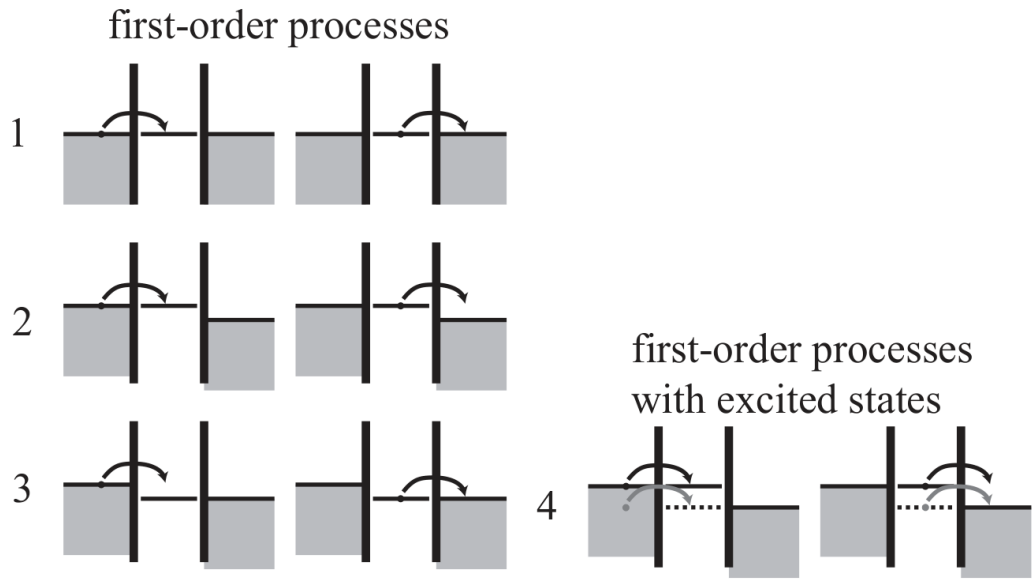

Figure 2.8: Sequential tunneling in a quantum dot. This type of transport is first-order in the lead couplings Γ_i and is only possible when a transition in the dot is in the bias window defined by the leads. **(1)-(3)** Transporting an electron across the dot requires two sequential tunneling events. **(4)** By increasing the bias window excited states can also be used for transport. Adapted from [32].

To transport an electron from the left lead to the right lead we need two of the above processes: left lead $\rightarrow$ dot and dot $\rightarrow$ right lead. That is, transport occurs in separate steps. This is shown in Figure 2.8. Sequential tunneling is also possible through excited states as shown in panel 4 in the same figure.

A standard result for sequential tunneling through a single quantum dot level is the Breit-Wigner shape of the resulting conductance [33]

$$G_{\mathrm{BW}} = \frac{e^2}{h}\frac{\Gamma_L\Gamma_R}{\Gamma_L+\Gamma_R}\frac{\Gamma}{(\epsilon/\hbar)^2+(\Gamma/2)^2} \tag{2.38}$$

where $\Gamma_{L,R}$ are couplings between left and right lead and the dot, $\Gamma = \Gamma_L+\Gamma_R$ and ϵ is the detuning of the level. An important point in eq. (2.38) is that when the level is on resonance $\epsilon = 0$ and the couplings are equal $\Gamma_L = \Gamma_R$ the conductance is e^2/h.

If only sequential tunneling is considered a current can only flow when the chemical potential of a transition (say, $\mu_{N\leftrightarrow N+1}$ from N to $N+1$) is positioned between the Fermi energy of the leads:

$$\mu_L > \mu_{N\leftrightarrow N+1} > \mu_R. \tag{2.39}$$

Transitions that are between the chemical potentials of the two leads are said to be in the bias window. In this situation the dot occupation oscillates like

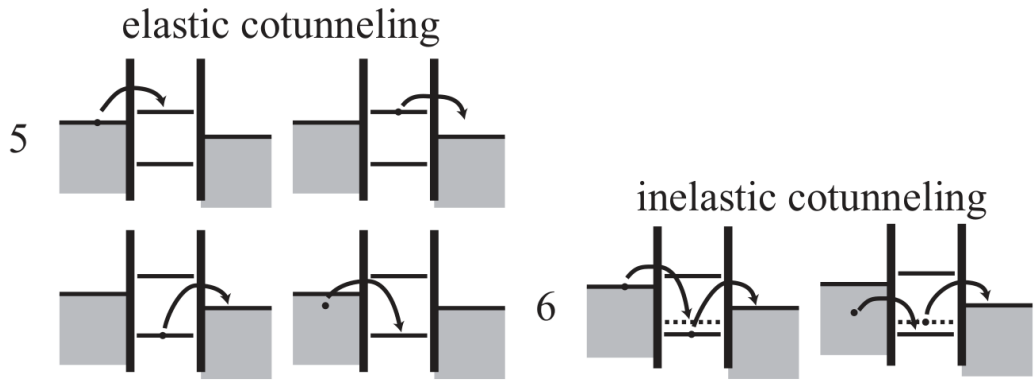

Figure 2.9: Cotunneling in a quantum dot. These second-order processes transport an electron across the dot via an intermediate state with a classically forbidden energy. **(5)** In elastic cotunneling processes the initial and final energy of the dot are the same, although the state of the dot electrons need not be. **(6)** If the final and initial states of the dot do not have the same energy the process is inelastic. The extra energy must be provided from somewhere else, in this case the source-drain bias. Adapted from [32].

$N \to N+1 \to N$. If no transition satisfies this condition no current flows, i.e., the dot is in Coulomb blockade.

Cotunneling is the second-order contribution to $\Gamma_{\beta\alpha}$. Second-order processes transport electrons all the way from the left to the right lead (they may also transport electrons from a lead onto the dot and then into the initial lead again, but these processes do not contribute to the current). Consider a second-order process that takes an electron from the left lead and puts it in the right lead via the intermediate state $H_{TL}\left|\alpha\right\rangle$.

$$\Gamma^{\text{2nd}}_{\beta\alpha} = \frac{2\pi}{\hbar}\left|\left\langle\beta\right| H_{TR}\frac{1}{E_\alpha - H_0}H_{TL}\left|\alpha\right\rangle\right|^2 \delta(E_\beta - E_\alpha) \tag{2.40}$$

Here, the states α and β differ by one electron in the leads.

Cotunneling processes are shown in Figure 2.9. They are either elastic or inelastic: In elastic cotunneling the initial and final state of the dot have the same energy, i.e. an electron transfers onto the dot and the same electron tunnels out again. In inelastic cotunneling an electron is removed from a level that is different from the one that was tunneled into by the first electron. In the latter case the energy difference between the initial and final state of the dot is provided by, e.g., the source-drain voltage or microwave radiation. In this project we will only consider source-drain voltage as the energy provider for cotunneling. Inelastic cotunneling spectroscopy was first used to probe the discrete spectrum of the quantum dot by De Franceschi et al. [34].

Let's rewrite (2.40) a bit to gain some intuition. Letting H_0 act on $\left|\alpha'\right\rangle \equiv$

$H_{TL}\,|\alpha\rangle$ gives $E_{\alpha'}$ so the fraction above becomes

$$\frac{1}{E_\alpha - H_0}\,|\alpha'\rangle = \frac{1}{E_\alpha - E_{\alpha'}}\,|\alpha'\rangle \tag{2.41}$$

The transfer Hamiltonians $H_{L,R}$ contain the tunneling amplitudes $t_{L,R}$ between the leads and the dot, so, leaving out the details, $\Gamma^{\mathrm{2nd}}_{\beta\alpha}$ becomes

$$\Gamma^{\mathrm{2nd}}_{\beta\alpha} \propto \frac{|t_{\mathrm{R}}|^2|t_{\mathrm{L}}|^2}{(E_\alpha - E_{\alpha'})^2} \tag{2.42}$$

The quantity $E_\alpha - E_{\alpha'}$ is the difference between the initial configuration and the configuration in which one electron in moved from the lead onto the dot. If state α has N electrons on the dot this energy difference is

$$E_\alpha - E_{\alpha'} = \epsilon_L - \mu_{N+1} \tag{2.43}$$

where ϵ_L is the energy of the electron in the lead that was transferred.

Let's restate (2.42) as[3]

$$\frac{|t_{\mathrm{R}}|^2|t_{\mathrm{L}}|^2}{(\epsilon_L - \mu_{N+1})^2} \propto \frac{\tau^2_{\alpha'}}{\tau_R\tau_L} \tag{2.44}$$

This fraction sets the amplitude for the cotunneling process. In order to have an appreciable amplitude $\tau_R\tau_L$ should be of the same order or smaller than $\tau^2_{\alpha'}$. Intuitively this means that the electron must be able to tunnel through the left and right barriers in a time comparable to or smaller than the time $\tau_{\alpha'}$ it's allowed to be in the virtual state α'. Thus, cotunneling is expected to be stronger in dots with strong tunnel couplings.

Elastic cotunneling is only limited by the amplitude (2.44) so it can occur even when the dot is in Coulomb blockade. Inelastic cotunneling has the further limitation that the source-drain voltage must match the energy difference between two levels in the quantum dot. Thus, when the current is dominated by cotunneling (i.e., in Coulomb blockade) *the current increases sharply when the source-drain voltage matches the energy difference between two energy levels in the dot.* Using this property of cotunneling to gain knowledge about the spectrum of the dot is called excitation spectroscopy. We will use excitation spectroscopy to determine the parameters of the nanotube in the Results and Discussion section

The condition above also means that no inelastic cotunneling current is possible before $|e|V_{\mathrm{SD}}$ is equal to the energy difference between the lowest two levels in the dot Δ_1. For $|V_{\mathrm{SD}}| > \Delta_1/|e|$ the current depends linearly on

[3] We're using $|t|^2 \propto 2\pi|t|^2 d = \Gamma \sim h/\tau$ where d is the density of states which is assumed constant. In a rigorous treatment the density of states is obtained from integration over initial and final states. $\tau_{\alpha'} = h/(\epsilon_L - \mu_{N+1})$ is the characteristic time that the system is allowed to virtually occupy the intermediate state α'.

source-drain bias because increasing V_{SD} allows more states in the leads to participate in the transport.

Finally, when the leads are superconducting and not metallic we should take into account the superconducting gap Δ_{SC} and the fact that the superconducting density of states is different from that in a metal. In the absence of in-gap states no transport is allowed before the source-drain bias is raised above Δ_{SC} since no quasiparticle states are available in the leads. This superconducting density of states may change the magnitude of the inelastic cotunneling current, but we will not consider such effects here.

2.2.3 Kondo physics in a quantum dot

The conventional Kondo effect arises from a magnetic impurity embedded in a metal [35]. Conduction electrons screen the spin of the impurity and form a many-body state with a characteristic energy $k_{\mathrm{B}}T_{\mathrm{K}}$. This causes scattering of the conduction electrons and increases the resistance once the temperature drops below T_{K}, the *Kondo temperature*.

A quantum dot with an odd number of electrons has a net spin-$\frac{1}{2}$. The occupied state with the highest energy will be doubly degenerate if time-reversal symmetry is not broken. We can now imagine cotunneling processes like above in which the dot electron with, say, spin up tunnels out and a conduction electron with spin down tunnels in. The net result is a spin flip of the dot electron. Summing all processes of this type again results in a many-body "Kondo" state between conduction electrons in the lead and the dot electron. Rather than suppress current as in a metal the Kondo state actually enhances current since it provides a spatially extended state at zero bias where the dot would normally be Coulomb blockaded. For a degeneracy of 2 this effect is known as the SU(2) Kondo effect which again has a characteristic energy of T_{K} (if we drop the k_{B}). Its effect is to increase the conductance at zero bias, ideally to a maximum of $2e^2/h$ when $T \ll T_{\mathrm{K}}$ rather than the standard e^2/h for sequential transport through a single level [36, 37]. The Kondo effect is only observed when the lead couplings are large since it relies on cotunneling processes.

We can imagine the same processes in a carbon nanotube, but in this system the level degeneracy is four rather than two. If the carbon nanotube levels are not too split relative to the lead couplings we can potentially get an SU(4) Kondo effect which involves all four levels. In analogy with the SU(2) case this gives rise to an ideal maximum conductance at zero bias of $4e^2/h$ [38, 39]. Thus, depending on the value of the lead couplings we can observe both the SU(2) and SU(4) Kondo effect in a carbon nanotube.

2.3 Superconductor-quantum dot systems

In a normal metal electrons can to a good approximation be treated as if they do not feel each other's repulsion. In a superconducting metal that is not so. Here, electrons attract each other through an interaction mediated by the positive ions in the lattice of the material. The result is that some electrons pair up into Cooper pairs which are named after Leon Cooper. He developed the BCS theory of superconductors with John Bardeen and John Schrieffer in three seminal papers [7, 8, 9]. This section describes the properties of superconductors from the point of view of BCS theory. We apply this theory in the data analysis in Chapter 6.

This section draws on the excellent textbook by Michael Tinkham [40].

2.3.1 BCS Theory

The defining property of superconductors is the ability to conduct a finite current with zero voltage drop. This dissipationless transport is only possible below certain *critical* values of temperature T_{C}, magnetic field B_{C} and current I_{C}. In temperature-magnetic field-current space we can speak of the *critical surface* below which the metal carries the current with no voltage drop.

Suppose we add a pair of electrons to a metal with a filled Fermi sea at $T = 0$. Further, suppose the paired electrons have opposite momenta $\mathbf{k}$ and $-\mathbf{k}$ and are in a spin singlet configuration to ensure that their wave function is anti-symmetric as required when fermions are exchanged[4]. We can write the state containing the Fermi sea and an additional electron pair as

$$|\psi\rangle = \sum_{k>k_{\mathrm{F}}} g_{\mathbf{k}} c^{\dagger}_{\mathbf{k}\uparrow} c^{\dagger}_{-\mathbf{k}\downarrow} |F\rangle \tag{2.45}$$

Here, $g_{\mathbf{k}}$ is a weight that determines how much a given $\mathbf{k}$-state contributes. By doing so it also ensures, e.g., that states with infinite momentum and energy are not occupied. All states with momentum smaller than the Fermi momentum $k < k_{\mathrm{F}}$ are filled by definition so unfilled states have $k > k_{\mathrm{F}}$. The creation (annihilation) operator $c^{\dagger}_{\mathbf{k}\sigma}$ ($c_{\mathbf{k}\sigma}$) creates (annihilates) an electron with momentum $\mathbf{k}$ and spin $\sigma =\uparrow,\downarrow$. Finally, $|F\rangle$ denotes the Fermi sea where all states up to k_{F} are filled with electrons.

Let us check that the pairs are actually in spin singlet configurations. Note that for a specific $\mathbf{k}_0$ with $k_0 > k_{\mathrm{F}}$ the sum in eq. (2.45) includes both

[4] Some superconductors host paired electrons whose momenta are not opposite and this allows for other spin configuration than the spin singlet [41, 42, 43]. In the following we deal only with *s*-type superconductors, where the paired electrons are always in spin singlet configurations. Furthermore, we will also restrict ourselves to type-I superconductors which have more basic magnetic properties than type-II superconductors.

$\mathbf{k}_0$ and $-\mathbf{k}_0$. Writing out both the $\mathbf{k}_0$ and $-\mathbf{k}_0$ term and requiring $g_{\mathbf{k}} = g_{-\mathbf{k}}$ we get for the part of $|\psi\rangle$ that concerns $\mathbf{k}_0$

$$\begin{aligned} |\mathbf{k}_0\rangle &= (g_{\mathbf{k}_0} c^\dagger_{\mathbf{k}_0\uparrow} c^\dagger_{-\mathbf{k}_0\downarrow} + g_{-\mathbf{k}_0} c^\dagger_{-\mathbf{k}_0\uparrow} c^\dagger_{\mathbf{k}_0\downarrow}) \, |F\rangle \\ &= g_{\mathbf{k}_0} (c^\dagger_{\mathbf{k}_0\uparrow} c^\dagger_{-\mathbf{k}_0\downarrow} - c^\dagger_{\mathbf{k}_0\downarrow} c^\dagger_{-\mathbf{k}_0\uparrow}) \, |F\rangle \end{aligned} \tag{2.46}$$

where we have used the fermion anti-commutator $\{c^\dagger_{\mathbf{k}\sigma}, c^\dagger_{\mathbf{k}'\sigma'}\} = 0$. The state in eq. (2.46) is, indeed, a spin singlet as required above. Being a singlet it is also an *entangled* state meaning that at least part of the state cannot be written as the product of two single-particle states. Moreover, it is a *maximally* entangled state since it consists solely of terms that cannot be written as the product of two single-particle states.

By inserting (2.45) into the Schrödinger equation it can be shown that the energy of the pair is lower than $2E_{\mathrm{F}}$ for reasonable assumptions. Thus, the pair forms spontaneously because it has lower energy than the two separate electrons.

The next step is to allow *all* conduction electrons in the metal to form pairs. In this case the wave function for N electrons can be expressed as

$$|\psi_N\rangle = \sum g(\mathbf{k}_i, \ldots, \mathbf{k}_t) c^\dagger_{\mathbf{k}_i\uparrow} c^\dagger_{-\mathbf{k}_i\downarrow} \cdots c^\dagger_{\mathbf{k}_l\uparrow} c^\dagger_{-\mathbf{k}_l\downarrow} \, |\phi_0\rangle \tag{2.47}$$

where $|\phi_0\rangle$ is the empty state containing no electrons whatsoever. This wave function is an educated guess. Its justification lies in whether or not it can be used to predict properties of superconducting metals. Proceeding as above, we extract these predictions by inserting (2.47) into the Schödinger equation. Below we summarize the predictions we obtain.

In a normal metal in three dimensions the electron density of states $N(E)$ goes as $\sqrt{E}$ [44]. Here, E is measured from the Fermi energy. Around a sufficiently small interval around E_{F} we can approximate the density of states by a constant $N(0)$. In a superconductor single-particle states are pushed away from the Fermi energy. We can see this in the density of states

$$\frac{N_s(E)}{N(0)} = \begin{cases} \frac{E}{(E^2-\Delta^2)^{1/2}}, & E > \Delta \\ 0, & E < \Delta \end{cases} \tag{2.48}$$

where E is the energy of independent (non-paired) particles and $N_s(E)$ is the superconducting density of states. In Figure 2.10 we compare the density of states of a superconductor with that of a normal metal. The square root divergence at $E = \Delta$ in the density of states of the superconductor is important for quantum transport because an electrical current depends on the density of states. $N_s(E)$ approaches the value of the normal metal far away from E_{F}. Equation (2.48) says that in the interval $-\Delta < E < \Delta$ no single-particle states exist in the superconductor. Outside this interval

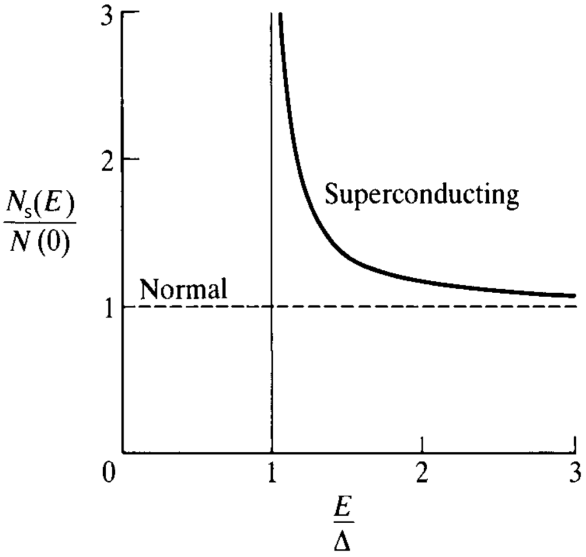

Figure 2.10: Comparison of density of states in a superconductor $N_s(E)$ and a normal metal $N(0)$. The density of states for the normal metal is approximated by the constant $N(0)$ which is reasonable because the energy scale of the interval $2\Delta \sim$ meV is small compared to changes in $N(E)$ which typically occur on the order of eV. The energy E is measured from the Fermi energy E_{F}. Adapted from [40].

single-particle excitations are typically called *bogoliubons* or *quasiparticles*[5].

In practice superconductors may show deviations from the ideal density of states outlined above. Recently, the distinction has been made in mesoscopic physics between a "soft" gap if the bogoliubon states "leak" into the gap and a "hard" gap if the gap more closely resembles the ideal case [46].

Our approach of eq. (2.47) hinges on idea that electrons pair up in a metal. The attraction that causes this pairing is not infinitely strong so we should expect the pairs to break up as we increase thermal fluctuations. Indeed, this can be observed in the temperature dependence of Δ which for the simple superconductors discussed here takes the form

$$\frac{\Delta(T)}{\Delta(T=0)} \approx 1.74 \left(1 - \frac{T}{T_{\mathrm{C}}}\right)^{1/2}, \qquad T \approx T_{\mathrm{C}} \tag{2.49}$$

[5] The latter terminology may lead to confusion since the term "quasiparticle" also denotes many-body states in quantum physics in general. Indeed, being the result of many-body interactions a Cooper pair may arguably be regarded as a quasiparticle itself (quasiparticle in the sense of a many-body state, not quasiparticle in the sense of a bogoliubon)! To be clear, in the terminology of superconductors, "bogoliubons" and "quasiparticles" both refer to single-particle excitations, while a Cooper pair can only be called a quasiparticle in the broad many-body meaning of the word (and even in that case it may be more suitable to call Cooper pairs "collective excitations" since they are bosons, see Mattuck pages 10, 227 [45]).

where $\Delta(T)$ is the magnitude of the gap at temperature T and T_C is the *critical* temperature at which the superconductor transitions into a normal metal. For temperatures much lower than T_C there is little variation in Δ because few extra bogoliubons are excited by an increase in temperature.

Similarly, we can derive an expression for the gap dependence on magnetic field [47]

$$\frac{\Delta(B)}{\Delta(B=0)} = \sqrt{1-(B/B_C)^2} \tag{2.50}$$

where $\Delta(B)$ is the magnitude of the gap at magnetic field B and B_C is the critical magnetic field at which the superconductor transitions into a normal metal. Actually, it is the magnetic flux through the superconductor that affects this change. Thus, for the thin film superconductors used in mesoscopic physics it is important to know how the magnetic field is oriented relative to the film.

The paired electrons have a characteristic spatial extent which is termed the *coherence length*. It is defined as

$$\xi = \frac{\hbar v_F}{\pi \Delta(T=0)}. \tag{2.51}$$

Note that ξ is inversely proportional to Δ meaning that superconductors with larger gaps have smaller coherence lengths.

All these predictions are consistent with experimental results which indicates that (2.47) is a good representation of the underlying physical system.

2.3.2 Transport in hybrid superconductor systems

Suppose we want to run a current through a superconductor coupled to a different system, e.g., a metal, an insulator or a quantum dot. In the simple case of a metal we already run into problems: The superconductor has no single-particle states at E_F for the metal electrons to go into. What happens instead is that the incoming metal electron is transferred to the superconductor while a hole is reflected from the interface to the superconductor. The net transfer is two electrons which pair up to form a Cooper pair in the superconductor. This is illustrated in Figure 2.11a). This process is called an *Andreev reflection* (AR) and the hole is said to be retro-reflected. If the hole is ejected into a different piece of metal electrode than that of the incoming electron the process is called a *crossed* Andreev reflection (CAR) (shown in Figure 2.11). Both processes can occur in reverse, that is, the superconductor ejects a Cooper pair so that the constituent electrons go into the same or separate metals. A reverse CAR is commonly referred to as *Cooper pair splitting* (CPS).

A schematic of a Cooper pair splitter device is shown in Figure 2.12. A

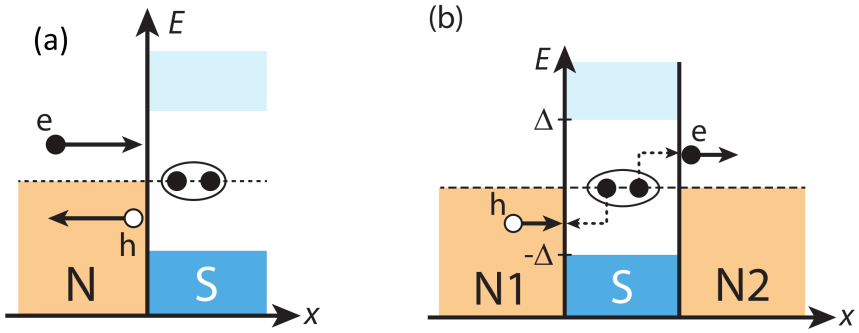

Figure 2.11: Schematics of a) an Andreev reflection and b) a crossed Andreev reflection. S (N) denotes superconductor (normal metal). In an Andreev reflection an electron impinging on a N-S interface is retro-reflected as a hole, thus transferring two electrons to the superconductor. A crossed Andreev reflection process proceeds along the same lines as an Andreev reflection, except that the retro-reflected hole is ejected into a different metal than the one of the impinging electron. As such, a CAR can be seen as the splitting of the Cooper pair such that its constituent bogoliubons go into different metals. Adapted from [48].

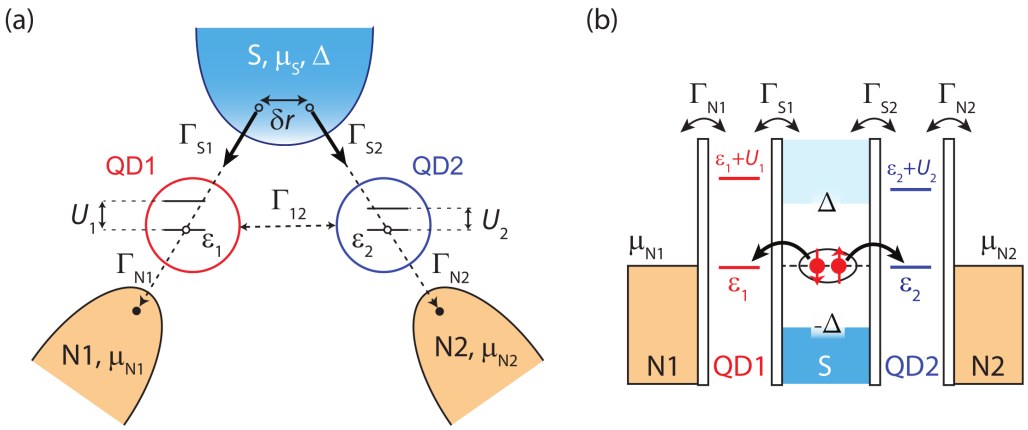

Figure 2.12: a) Schematic showing parameters of the Cooper pair splitter system with superconducting (S) and normal (N) leads and two quantum dots (QD1,2). The leads have chemical potentials μ and couplings Γ to the quantum dots which have a mutual coupling Γ_{12}. The energy of the quantum dot levels is given by $\varepsilon_{1,2}$ and the charging energies are $U_{1,2}$. δr is the spatial separation between the tunneling points. If δr is larger than the coherence length I_{CPS} is exponentially suppressed. The level spacing between spin-degenerate levels ΔE is not shown in the figure. b) Energy diagram of the Cooper pair splitter system. The black arrows show the process for the Cooper pair splitting current I_{CPS}. Adapted from [49, 48].

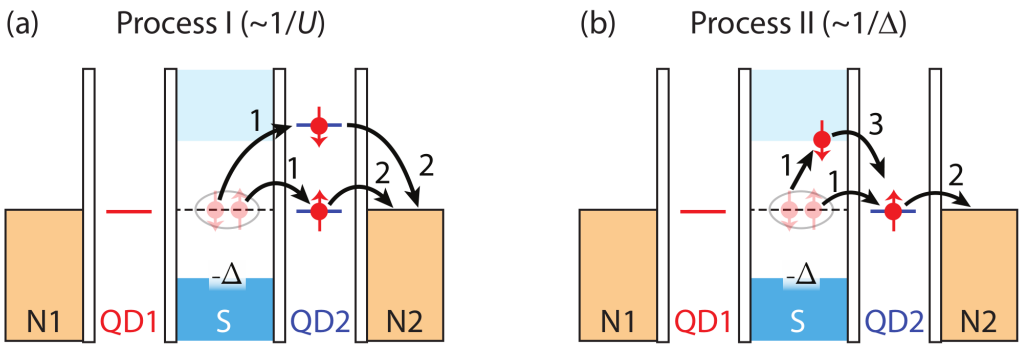

Figure 2.13: Schematics of elastic cotunneling process involving virtual occupation of intermediate states in a) QD2 and b) the superconductor. Process I is suppressed as $1/U$ and process II is suppressed as $1/\Delta$. Consequently, in order to suppress the current due to cotunneling I_{EC} large U and Δ are required. Adapted from [48].

central superconductor is connected to two quantum dots which are in turn connected to normal metal leads. The charging energies U_1 and U_2 on the dots suppress tunneling of Cooper pairs into the same dot.

The purpose of the Cooper pair splitter is to separate Cooper pairs. An interesting feature of the split Cooper pairs is that their constituent bogoliubons remain entangled as they travel on in either lead. Thus, the Cooper pair splitter can be regarded as a rough electronic analog to experiments on EPR pair generation in quantum optics [50, 51, 52]. Note, however, that while entanglement experiments in optics deal with single pair detection the electronic Cooper pair splitter has current as observable. Except in the case where an additional dot senses the charge transport [53] the current measurement is an average over many splitting pairs. Generating entangled particles is also important for quantum computing algorithms [54].

Multiple transport processes are possible in a Cooper pair splitter apart from CAR. In the following we will briefly review the theoretical results of the analysis of transport by Recher et al. [49] of the CPS system.

The splitting of Cooper pairs is identified by current measurements. The benchmark of the Cooper pair splitter can be defined as the ratio between the current due to Cooper pair splitting I_{CPS} and that due to other (elastic cotunneling) processes I_{EC}. Figure 2.12b) shows the desired Cooper pair splitting transport process and Figure 2.13 shows unwanted elastic cotunneling transport processes. In Figure 2.13a) the intermediate cotunneling state is the next level in the quantum dot, while in Figure 2.13b) the intermediate state is the lowest bogoliubon. The former is suppressed as $1/U$ and the latter is suppressed as $1/\Delta$ by the same arguments as in section 2.2.2 so it is desirable to have U and Δ larger than the applied bias $|eV_{\mathrm{SD}}| = |\mu_S - \mu_{N1,2}|$.

The Cooper pair cannot split if one dot is occupied and the other is not. Thus, the dot-lead couplings should be larger than the superconductor-dot

couplings to increase the probability that both dots are unoccupied.

The level spacing ΔE is required to be larger than $|eV_{\rm SD}|$ to avoid processes where an electron with spin σ jumps onto the dot and another electron with opposite spin jumps back. Such processes destroy the entanglement of the bogoliubons in the Cooper pair. Similarly, we require that $\Gamma_{N1}, \Gamma_{N2} < |eV_{\rm SD}|$ to avoid spin-flip processes into and out of the leads. Finally, the thermal energy $k_{\rm B}T$ must be smaller than $|eV_{\rm SD}|$ in order for the voltage excitation not to be dominated by thermal fluctuations.

The conditions for the largest $I_{\rm CPS}/I_{\rm EC}$ ratio can be summarized as

$$\Delta, U, \Delta E > |eV_{\rm SD}| > \Gamma_{N1}, \Gamma_{N2}, k_{\rm B}T, \qquad \Gamma_{N1}, \Gamma_{N2} > \Gamma_S. \tag{2.52}$$

Apart from conditions on energy scales we should also require that the S-QD tunneling points δr are not separated by more than the coherence length ξ. Otherwise $I_{\rm CPS}$ will be exponentially suppressed with increasing δr. Keep in mind that these results are only strictly valid for a superconductor with a hard gap.

The first experimental observations of CAR in metal-superconductor junctions is by Beckmann et al. [55]. In Beckmann's work two ferromagnetic metal electrodes are connected to an Al superconductor via oxide barriers. A current is sourced across one of the barriers and the voltage across the other barrier is measured. The central finding is that the latter voltage depends on whether the magnetizations of the ferromagnetic leads are parallel or anti-parallel. This is consistent with CAR processes since having anti-parallel magnetizations increases the probability of joining two electrons with opposite spins. Soon after, Russo et al. [56] were able to quantify the relative contributions of EC and CAR to the transport of the same configuration.

The configuration described above lacks control over the splitting process. Such control was demonstrated at about the same time in a nanowire CPS [13] and a carbon nanotube CPS [11]. In the former work Hofstetter and coworkers showed that the magnitude and sign of the nonlocal signal depended strongly on the tuning of the quantum dot as shown in Figure 2.14. Later work on Cooper pair splitters has explored, e.g., the effect of finite bias [57], the possibility of high efficiency splitting [12] and detection with noise measurements [14].

To characterize Cooper pairs splitters two figures of merit are commonly used: efficiency ϵ and visibility η. In this thesis we will use the definitions by Schindele et al. [12]

$$\epsilon = \frac{2G_{\rm CPS}}{G_1 + G_2}, \qquad \eta = \eta_1\eta_2 = \frac{\Delta G_1}{G_1}\frac{\Delta G_2}{G_2} \tag{2.53}$$

where G_i is the differential conductance in dot i, ΔG_i is the additional conductance in dot i due to the Cooper pair splitting process and $G_{\rm CPS}$ is the additional conductance identifiable in *both* dots due to the Cooper pair splitting process: $G_{\rm CPS} = \min(\Delta G_1, \Delta G_2)$. In this thesis we will sometimes refer

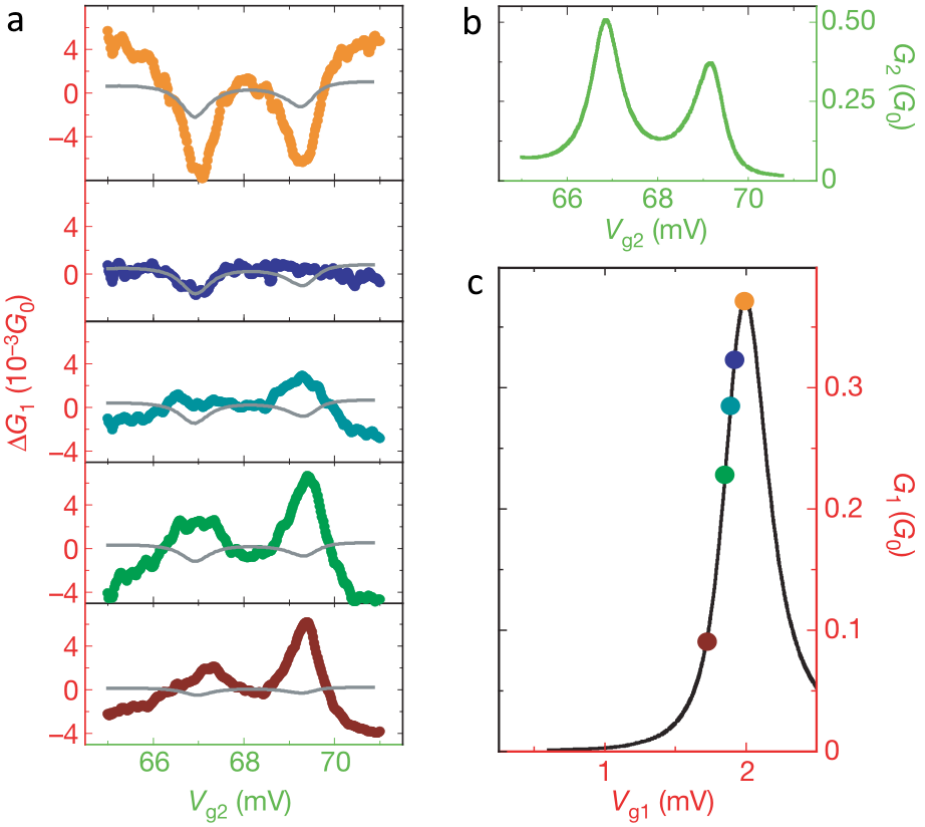

Figure 2.14: Standard measurement of the nonlocal signal in a Cooper pair splitter. The gate voltage V_{g2} on dot 2 is swept (panel a) while the gate voltage V_{g1} on dot 1 is held constant at various points (detunings) on a Coulomb peak in dot 1 (panel c). Panel b shows the Coulomb peaks in dot 2. Clearly, the detuning in dot 1 affects the magnitude and sign of the nonlocal signal ΔG_1. Adapted from Hofstetter et al. [13].

to η as the *global* visibility and $\eta_{1,2}$ as *local* visibilities. The additional signal ΔG will sometimes be referred to as the *nonlocal* signal. We note that other definitions of efficiency exists, e.g., in reference [58].

In addition, the theoretical proposal by Braunecker et al. [10] suggests using the parameter Q in a Bell-like test [51] to determine whether the splitting Cooper pair are entangled:

$$Q = \left| C_{\mathbf{a}_K,\mathbf{b}_K} + C_{\mathbf{a}_K,\mathbf{b}_{K'}} + C_{\mathbf{a}_{K'},\mathbf{b}_K} - C_{\mathbf{a}_{K'},\mathbf{b}_{K'}} \right| \leq 2 \tag{2.54}$$

where the spin-spin correlator

$$C_{\mathbf{a}_\tau,\mathbf{b}_{\tau'}} = \frac{\sum_{\nu,\nu'=\pm} \nu\nu' G_{\nu a_\tau,\nu' b_{\tau'}}}{\sum_{\nu,\nu'=\pm} G_{\nu a_\tau,\nu' b_{\tau'}}}. \tag{2.55}$$

for spin polarization axes $\mathbf{a}$ and $\mathbf{b}$ and $G_{\nu a_\tau,\nu' b_{\tau'}}$ is the conductance product $G_1 G_2$ integrated over a suitable region centered on a resonance crossing. We will discuss the Q parameter in Chapter 5.

Chapter 3

Fabrication and Experimental setup

3.1 Fabrication

Device fabrication on the nanoscale requires use of multiple advanced techniques, all of which have a number of tunable parameters that must be just right in order for the fabrication to be successful. Part of the present project has been to figure out the right combination of parameters for the fabrication of carbon nanotube devices with arbitrary geometries, i.e. figuring out the fabrication recipe. An overview of this development process as well as the final recipe are available in Appendix A.

Carbon nanotube devices with Cooper pair splitter (CPS) geometries were a specific focus in this project. One such device is shown in Figure 3.1. The CPS geometry consists of a central superconducting lead with two normal leads placed symmetrically on either side of it. The side gates can be on either side of the nanotube. This geometry defines two quantum dots in the carbon nanotube that can be tuned with the side gates. This thesis presents data from one CPS device in chapters 5 and 6. We will refer to this device as devA in the following. Chapter 4 presents data from a 2-terminal carbon nanotube device. Details for the fabrication process for this device can also be found in Chapter 4.

The normal (i.e., non-superconducting) leads on devA consist of 50 nm Au (thermally evaporated). Typically, a thin layer (≈ 5 nm) of titanium or chromium is deposited below the Au to "stick" the Au to the surface of the chip since Au peels off easily by itself. Due to fabrication irregularities this sticking layer was not deposited on devA which means that the nanotube is in direct contact with the Au.

The superconducting lead on devA is 5/15 nm Ti/Al (e-beam evaporated). A thin layer was chosen for the aluminium to give a high critical in-plane field in the superconducting state. The standard value for the crit-

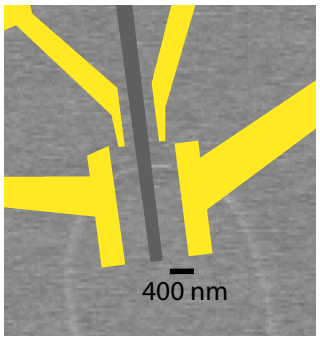

Figure 3.1: Scanning electron microscope (SEM) image of the nanotube in devA with metal leads overlaid digitally. The gold areas are 50 nm Au and the dark grey area is 5/15 nm Ti/Al. The image was taken before metal leads were deposited which is why they are overlaid instead. To avoid the risk of damaging the nanotube no SEM image has been taken of the device after metal leads were deposited.

ical magnetic field of bulk aluminium at 0 K is 10.5 mT [44]. This value is too low to change the energy levels in a typical carbon nanotube appreciably which is required for the Braunecker proposal.

For the nanotube growth we decided to use few lithographically defined catalyst islands rather than spreading smaller catalyst particles over the full chip. Having precisely defined catalyst islands provides spatial control with the nanotubes thus making it easier to avoid stray tubes shorting electrodes. However, having less catalyst may also lead to fewer nanotubes overall.

A 1×1 cm chip would typically have 16 catalyst islands, each with diameters of about 10 µm. The diameter was increased from about 3 µm early in the process since the smaller diameter islands tended to be removed in the lift-off step. The 10 µm islands were remarkably robust when defined with a double resist layer of A6 as done in ref. [59]. It was not uncommon for a base chip with 32 islands to have 100% yield after the catalyst deposition step. Alignment marks were placed at the corners of a 100×100 µm square for accurate alignment of the inner features. An example of an inner square before processing electrodes is shown in Figure 3.2. The nanotube yield in this figure was typical in this project. It is ideal for fabricating devices since only one or two tubes are long enough to extend a significant distance ($\gtrsim 1$ µm) from the catalyst island. Fewer or shorter nanotubes cause cramped designs because of proximity to the catalyst island. Avoiding stray nanotubes becomes a problem if the tubes are longer and more numerous. In perhaps 10% of the growths either zero or thousands of nanotubes would form, rendering the chip useless. We did not investigate this issue, since a new growth could easily be made after removing the nanotubes with plasma ashing [60].

Figure 3.2 demonstrates that the nanotubes readily position themselves in advantageous geometries for fabricating Cooper pair splitters. The cross-

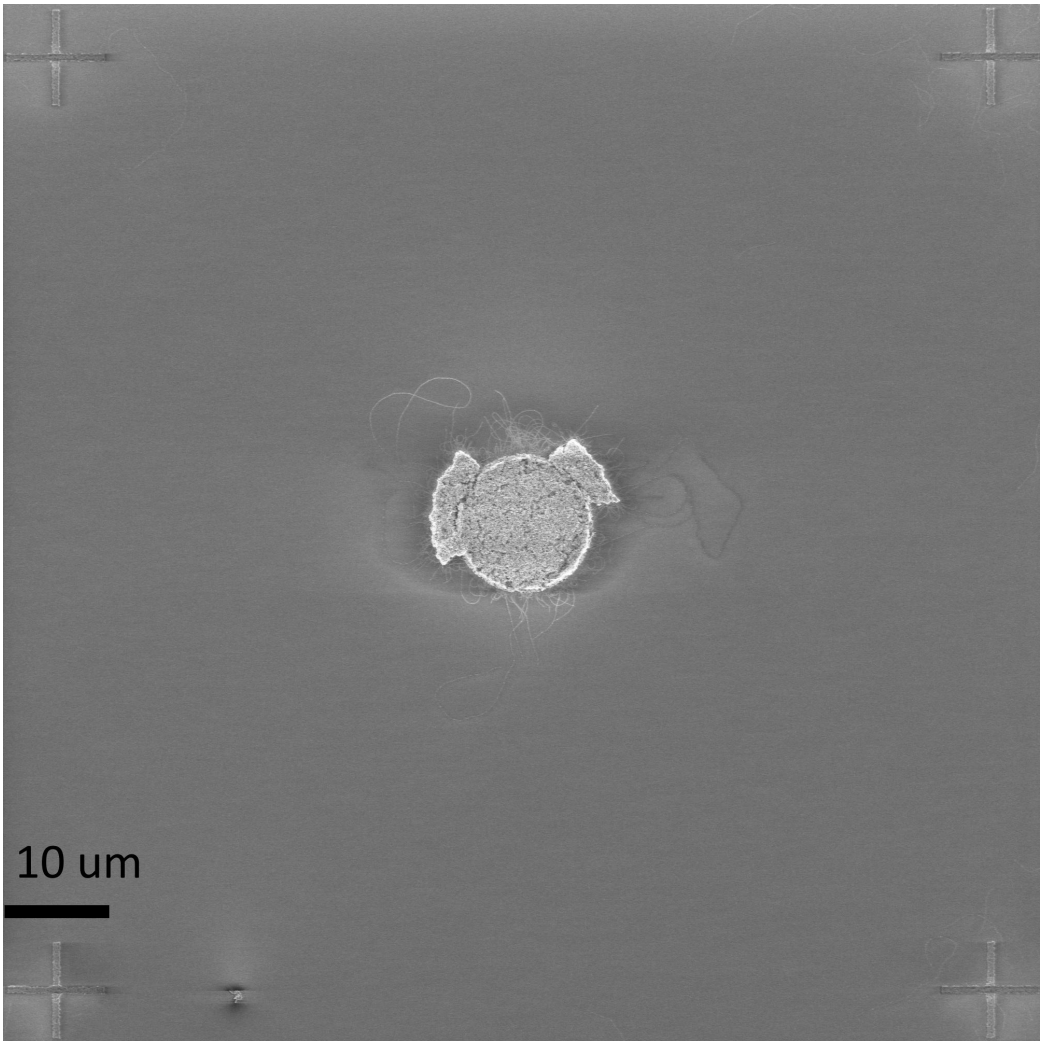

Figure 3.2: Central $100 \times 100\,\mu$m area of a carbon nanotube chip after CVD growth. Carbon nanotubes (dark and light grey lines) are seen "sprouting" from the central catalyst island. The island is defined lithographically to be a perfect circle, but it typically ended up somewhat smaller or larger as seen here. Alignment marks for accurate alignment of electrodes to the nanotubes are seen in the corners.

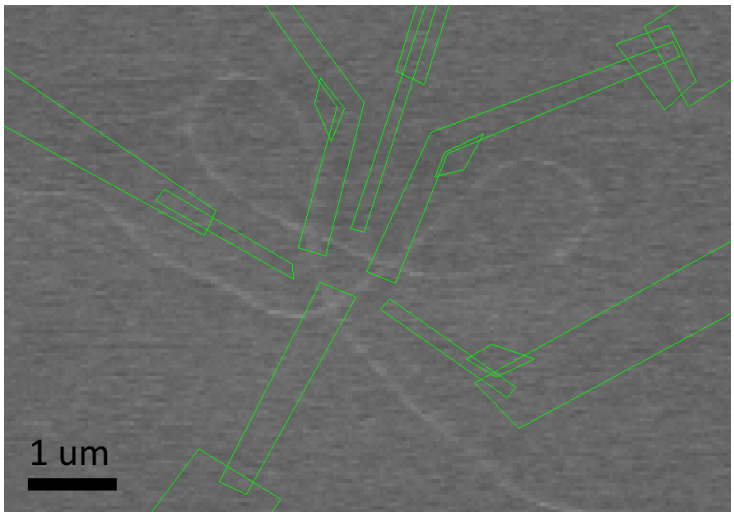

Figure 3.3: Close-up of a nanotube (light grey line) curved into a complex geometry. Electrodes (green) have been overlaid graphically on the device, forming three side-gated quantum dots.

ing nanotube to the upper left of the catalyst island is one example of this. One explanation for this self-arrangement of the tubes is that they grow perpendicular to the chip and collapse onto the substrate while entangling once they become too long to sustain themselves [61]. At the substrate van der Waals forces prevent them from disentangling. The nanotubes often twisted into even more interesting geometries as shown in Figure 3.3. Although this particular nanotube geometry was the most spectacular encountered in this project similar geometries were observed in about 1 out of 16 islands, or roughly one per $1 \times 1\,\mathrm{cm}$ chip. Such tube geometries could be used to implement, e.g., a Shiba molecule [62], in this case with three Shiba "atoms". Unfortunately, the final device exhibited low conductance at room temperature, indicating that it would not have formed a well-behaved dot at low temperatures.

3.1.1 Fabrication challenges

Although devA exhibits a clean electronic structure, which is desirable for carbon nanotube devices, it should be noted that only a few high-quality devices were fabricated out of hundreds of attempts. The chip containing devA had a yield of $\approx 40\%$ for Cooper pair-splitter geometries and was one of the earliest fabricated in this project. Despite great efforts to replicate the exact process for this chip the yield never increased beyond 5% in subsequent attempts. Thus, despite the quality of the devA chip the overall yield for the fabrication process described here and in Appendix A is still in the single digits percent. Specifically, the issue was obtaining conducting nanotubes at room temperature. Low temperature properties were rarely measured be-

cause of the low room temperature conductance. In the following we outline some of the measures that were taken to combat this issue. Please refer to section A.4 for more details

One concern about the fabrication process was the necessity of imaging the carbon nanotubes with a SEM after growth in order to design device geometries on them. We were concerned that the SEM electron beam would damage the nanotubes and alter its electronic properties. Although some devices with carbon nanotubes of high quality have been fabricated in this project it is unknown whether the yield would have been higher if the nanotubes had not been imaged. It is the impression of this author, though, that the adverse effects of imaging are negligible compared to the type of metal used in the leads, the width of the metal leads, how well resist is removed in the development step before depositing metal leads and the pressure and procedure of metal evaporation.

When a normal metal is brought into contact with a semiconductor a Schottky barrier is formed. The height of the barrier depends on the difference in the work functions in the metal and semiconductor. This has recently been discussed in the context of carbon nanotubes in ref. [28]. A high barrier may cause the metal-CNT junction to block all electron transport so the typical approach is to choose a metal with a work function close to the $\approx 4.7 - 4.8$ eV found in CNTs [28]. Gold (5.1 eV), chromium (4.5 eV), palladium (4.25 eV), rhodium (4.98 eV) and titanium (4.33 eV) [63] are often used. In this project gold (both thermal and e-beam evaporation), titanium and palladium (both from the Copenhagen lab and the Laboratoire Pierre Aigrain run by Professor Takis Kontos) were used with no observable and/or consistent difference in conductance of the final devices.

If a suitable metal is selected and the Schottky barrier is low enough to allow transport the metal-CNT interface may still be degraded by impurities. This is especially true for typical nanofabrication processes where resist is repeatedly applied to and stripped from the substrate. It is standard practice to plasma ash the substrate after development to remove any resist residues. This is not an option for CNTs since plasma ashing damages the tubes [60]. Instead, efforts have been made towards "ultra-clean" nanotube devices [1] where nanotube placement is the last step in the fabrication process. The issue of resist contamination has been treated recently by Samm and coworkers at the University of Basel in ref. [64]. They find that substituting the PMMA resist for ZEP520A results in better yield. The fabrication process is described in great detail in ref. [65]. Despite following the process above no difference in conductance was observed in this project indicating the presence of at least one other issue.

Another potential cause for contamination of the metal-CNT interface is using an inadequate dose when exposing the electrodes. In the same vein, an inadequate lift-off can leave residues behind. Dose tests and lift-off tests were

conducted to investigate this. The results showed that the electrodes themselves have a wide margin of error before breaking because of underexposure or fusing together to short-circuit. A factor of two between the clearing dose and the fusing dose was not unusual. However, varying the dose or the lift-off process did not yield observable differences for the nanotube conductance.

One interpretation of the low nanotube device conductance is that the metal-CNT contact is mediated by point-like uncontaminated spots. If a given piece of the nanotube has a high probability of being covered by contaminants, one could argue that high conductance devices are those where a point-like uncontaminated metal-CNT interface exists, not those with low general contamination. To investigate this we conducted tests where the electrode width was varied since wider electrodes would increase the probability of hitting an uncontaminated point on the nanotube with the electrode. This test also did not show observable or consistent increased conductance.

An interesting approach to avoiding contamination is to use ice as a novel type of resist for CNT devices. Although "ice lithography" yields clean devices and minimizes resist residue it also requires major modifications to e-beam lithography equipment [66, 67, 68, 69]. Also, to our knowledge no low-temperature studies have been made yet of CNT devices fabricated using ice lithography. Such studies could provide further insights into the influence of resist on nanotube device quality.

Of course, the nanotubes themselves may be of low quality. For instance, defects and oxygen functionalization have been found to heavily impact CNT conductivity [60, 70]. Varying the gas flows and durations of the growth process in the Copenhagen lab did not yield an observable difference in nanotube conductance. However, the CVD tube itself, which may also be a source of contamination, was not changed during the process. The strongest test of the hypothesis that the nanotubes are low quality is to obtain nanotubes that are known to work from other laboratories. Nanotube samples from University of Basel and Laboratoire Pierre Aigrain did not show observably increased conductance, however. Processing the samples from University of Basel was made difficult by the fact that their surface had become hydrophilic which effectively prevented resist spinning. The usual treatment for this issue, plasma ashing, was not available because of its detrimental effects on the structure of CNTs [60].

In summary, although one batch of high-quality devices was successfully fabricated no general method for obtaining such devices was developed. Improving the nanofabrication scheme as attempted above certainly has the potential to yield high-quality devices as attested by the high-quality devices in the literature. However, it is the author's opinion that in order to efficiently employ nanotubes in devices with advanced geometries or materials while maintaining low disorder (that is, $\Delta_{\mathrm{SO}} > \Delta_{KK'}$) it is necessary to explore novel fabrication schemes. Such schemes could include ice lithography

or in-situ screening of nanotubes at cryogenic temperatures [71, 72].

3.2 Experimental Setup

All measurements were done in a Oxford Instruments Triton200 dilution refrigerator at a base temperature of 30 mK unless otherwise specified. The base temperature is calibrated at installation by Oxford Instruments engineers using ^{60}Co nuclear orientation thermometry. During standard operation the base temperature is measured using a RuO_2 sensor. The electron temperature was not measured in this project but it is typically ~ 100 mK [73, 74].

Temperatures in the tens of millikelvins range are achieved by dilution refrigerators by letting ^{3}He cross a phase boundary between a pure ^{3}He phase (the concentrated phase) and a ^{3}He-^{4}He phase (the dilute phase). In doing so the ^{3}He extracts energy from the system. This process occurs continuously in a mixing chamber. Pumping on the dilute phase preferentially removes ^{3}He which prevents the phases in the mixing chamber from reaching equilibrium. The ^{3}He is then recycled and eventually enters the concentrated phase again where the process is repeated. The Triton200 refrigerator is cryogen free, meaning that the ^{3}He-^{4}He mixture is kept in a closed loop. Having a closed loop is advantageous because liquid ^{4}He and especially ^{3}He are rather expensive.

The refrigerator is fitted with a superconducting vector magnet powered by a Mercury iPS. The magnet can reach (nominally) 3 T in the x-direction and 8.5 T in the z-direction. The magnet is unable to set a field in the y-direction. Cylindrical polar coordinates can also be used which allows the magnetic field to be set at an arbitrary angle within 3 T in the x-z plane. The sample itself is also in the x-z plane so no out-of-plane magnetic field can be applied.

The electrical setup is as shown in Figure 3.4. All DC lines in the cryostat go through an RF filter to prevent high frequency noise. All lines also go through an RC filter for low-frequency filtering, but only the lines connecting the side gates have resistances in the RC filter. For the remaining lines the resistance was removed from the RC filter to make correlation measurements easier. The specific instrument models used are as follows: DAC: DecaDAC custom-built by Jim MacArthur at Harvard. Lock-in amplifiers: Stanford Research Systems SR830. Multimeters: Agilent 34401A. Current amplifiers: Ithaco DL1211. Voltage source: Keithley 2614B.

The figure also shows the couplings between the normal leads and the nanotube Γ_{NL} and Γ_{NR}, and the coupling between the superconducting lead and the nanotube Γ_{SL} and Γ_{SR}.

The current amplifier has two inequivalent output connections. One which passes the signal through a low-pass filter with a variable time constant

and one in which the signal is not filtered. The first output is configured to a time constant of $\sim 100\,\mathrm{ms}$ and sent to a multimeter for measuring DC current. The second signal is sent to a lock-in amplifier for measuring differential conductance using standard techniques.

The differential conductance $\mathrm{d}I/\mathrm{d}V_{\mathrm{SD}}$ is obtained using either the lock-in signal or numerically differentiated DC current which is in some cases less noisy. The second derivative of the current $\mathrm{d}^2I/\mathrm{d}V_{\mathrm{SD}}^2$ is obtained either by numerically differentiating the lock-in signal by V_{SD} or directly from the lock-in (see Appendix C.1).

Data acquisition was done with the matlab-qd framework for Matlab written by Anders Jellinggaard[1].

[1] The framework is available here `https://github.com/qdev-dk/matlab-qd`. Special thanks go to Anders for supplying this code which simplified data acquisition immensely.

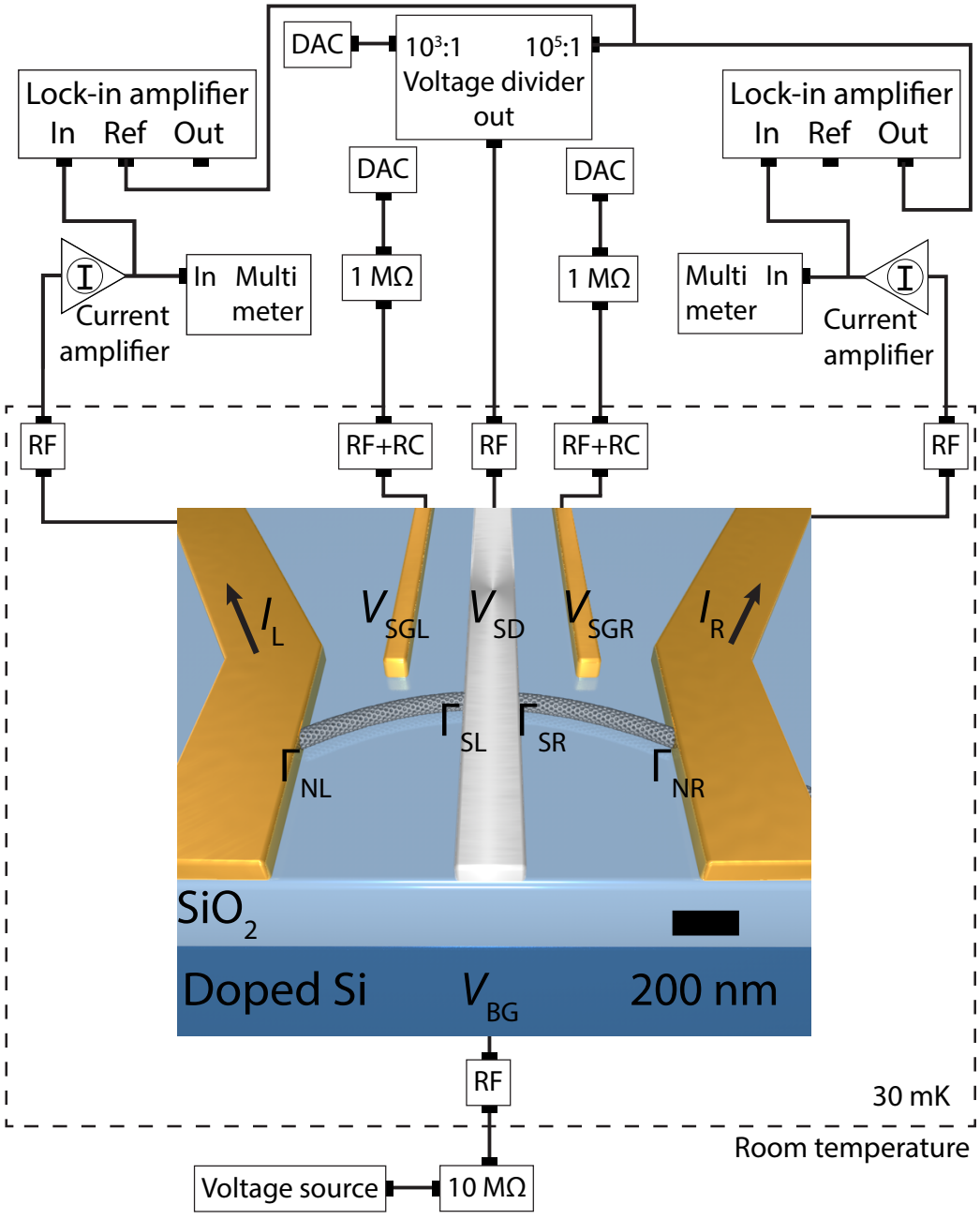

Figure 3.4: Setup for measuring devA. A DC and AC voltage is applied to the central superconducting lead and the corresponding DC and AC current through each nanotube segment is measured two-terminally. Couplings $\Gamma_{(S/N)i}$, currents I_i, bias voltage V_{SD} and side gate voltages V_{SGi} are shown on the device. Note that 1 and 2 are sometimes used in place of L and R for the currents, couplings and side gates. The makes of the instruments are specified in the main text. See also Figure 5.1.

Chapter 4

Coupling of shells in a carbon nanotube quantum dot

This chapter is planned for submission in the journal Physical Review B as

M. C. Hels, T. S. Jespersen, J. Nygård, and K. Grove-Rasmussen. Coupling of shells in a carbon nanotube quantum dot.

The device investigated in this chapter was fabricated and measured by K. Grove-Rasmussen and T. S. Jespersen. The rest of the work was done primarily by M. C. Hels with input from the other authors.

Abstract

We systematically study the coupling of longitudinal modes (shells) in a carbon nanotube quantum dot. Inelastic cotunneling spectroscopy is used to probe the excitation spectrum in parallel, perpendicular and rotating magnetic fields. The data is compared to a theoretical model including coupling between shells, induced by atomically sharp disorder in the nanotube. The calculated excitation spectra show excellent correspondence with experimental data.

Introduction

Carbon nanotube (CNT) quantum devices have been the basis for many studies of, e.g., quantum information processing [18, 75, 76, 77], spintronics [78] and coupling of mechanical and electronic degrees of freedom [79, 80]. CNTs are attractive because their electronic behavior is well-understood and can be accurately described with a single-particle model. This sets them apart from other more complex systems such as 2DEGs and nanowires. The basic behavior can be captured in a simple four-level model for spin $s = \uparrow, \downarrow$ and valley $\tau = K, K'$ degrees of freedom. Advances in fabrication have produced high quality nanotube devices [1, 71] which enable measurements

of more exotic properties such as, e.g., spin-orbit interaction [17, 81, 82, 83]. The additional valley degeneracy increases the total degeneracy from two to four in CNT quantum dot longitudinal modes (shells) [16, 84, 85]. So far, the coupling of nanotube shells has not been examined in detail since the level spacing between shells in carbon nanotubes is typically so high that this coupling can be safely neglected.

In this paper, we systematically study the coupling of three shells in a CNT quantum dot and show that it can be adequately described with a minimal extension of the existing model [24]. The nanotube spectrum is probed experimentally with inelastic cotunneling spectroscopy [86] which yields the differences between energy levels in the nanotube quantum dot. The evolution of the energy level differences for various fillings of a nanotube shell is measured as a function of parallel, perpendicular and rotation of the magnetic field. The quality of the model is assessed by calculating the excitation spectrum and fitting it to the obtained data. We find that the model fits the data well given two sets of parameters describing fillings of 0, 1 and 2, 3 and 4, respectively.

Model

For the states in shell ν we will use an effective four-level model [24, 81, 82, 83, 87, 88] for a carbon nanotube quantum dot in an applied magnetic field with magnitude B and angle θ measured from the nanotube axis:

$$\begin{aligned} H_\nu =& g_\mathrm{s}\mu_\mathrm{B}B(\cos\theta\sigma_z\tau_0 + \sin\theta\sigma_x\tau_0) \\ &+ g^\nu_\mathrm{orb}\mu_\mathrm{B}B\cos\theta\sigma_0\tau_z + \Delta^\nu_\mathrm{SO}\sigma_z\tau_z \end{aligned} \tag{4.1}$$

where τ_i and σ_i are Pauli matrices in valley (K, K') and spin space, g_s the electron spin g-factor and μ_B the Bohr Magneton. The effect of the magnetic field on the circumferential motion is opposite for K and K' and is set by the orbital angular moment g^ν_orb. Δ^ν_SO sets the magnitude and sign of the spin-orbit interaction which couples spin and valley states. Each shell ν has its own set of parameters as indicated by the superscript. This is justified by experimental studies which show that the parameters may change significantly between shells, but rarely change within a shell [81, 22].

Both shell index ν, valley index τ and spin s are conserved quantities in H_ν so we can label the eigenstates as $|\nu\tau s\rangle$. When imposing periodic boundary conditions along the circumference and hard-wall boundary conditions at the nanotube-electrode interfaces we get the following wave functions for a metallic nanotube [83, 88]

$$\Psi_{\nu\tau s}(\phi, z) = \langle \mathbf{r}|\nu\tau s\rangle = \frac{1}{\sqrt{\pi L}} e^{i\tau q\phi}\sin(\nu z\pi/L)\,|s\rangle\,. \tag{4.2}$$

Here $\nu = 1, 2, \ldots$, $\tau = \pm 1$ for K, K'. The nanotube quantum dot segment has length L, $\mathbf{r}$ is the position vector for the electron, z lies along the nanotube axis, and ϕ is along the circumferential direction. The orbital quantum number q is defined by the chiral vector indices n_1, n_2 as $q = (n_1 - n_2)/2$ which is an integer for metallic nanotubes. Note that the nanotube is only nominally metallic as it may still exhibit a (smaller) bandgap induced by curvature [24].

We now introduce a perturbation H' to couple K and K' states motivated by disorder in the nanotube and interaction with the substrate

$$H' = V(z)\delta(\phi). \tag{4.3}$$

Here $V(z)$ is an atomically smooth perturbation in the longitudinal z direction and $\delta(\phi)$ is an atomically sharp perturbation along the circumference. Note that H' can only couple K and K' states if it contains an atomically sharp part [24]. H' leads to the following matrix elements

$$\langle \nu m s | \, H' \, | \nu' m' s' \rangle = \Delta_{KK'}^{\nu\nu'} \delta_{ss'} \tag{4.4}$$

where

$$\Delta_{KK'}^{\nu\nu'} = \frac{1}{\pi L} \int_0^L V(z) \sin(\nu z \pi / L) \sin(\nu' z \pi / L) dz. \tag{4.5}$$

Hence, this perturbation mixes all states in shell ν with all states in shells ν', except states with opposite spin. Note that eq. (4.5) implies $\Delta_{KK'}^{\nu\nu'} = \Delta_{KK'}^{\nu'\nu}$.

For a constant $V(z) = V_0$ we get for the coupling of shell ν with itself

$$\langle \nu m s | \, H' \, | \nu m' s' \rangle = \Delta_{KK'}^{\nu} \equiv \Delta_{KK'}^{\nu\nu} \delta_{ss'} = \frac{V_0}{2} \sigma_0 (\tau_0 + \tau_x) \tag{4.6}$$

The τ_0 term is often ignored when considering only a single shell because it simply amounts to a shift in energy which can be absorbed in the level spacings. The remaining τ_x describes the usual KK' mixing. Here, we extend the standard model described above by allowing terms in the expansion of $V(z)$ which are first-order and above in z. These terms lead to the same structure as eq. (4.6), but they are off-diagonal in shell space.

In the following we will restrict ourselves to three shells labeled $\nu = 0, 1, 2$ and separated by level spacings $\Delta E_{\nu\nu'}$, so that the full 12-dimensional Hamiltonian becomes in ν-space

$$H = \begin{pmatrix} H_0 & 0 & 0 \\ 0 & H_1 + \Delta E_{01} & 0 \\ 0 & 0 & H_2 + \Delta E_{12} \end{pmatrix} + \Delta_{KK'}^{\nu\nu'} \delta_{ss'} \tag{4.7}$$

Each shell has three intrinsic parameters, g_{orb}, Δ_{SO} and $\Delta_{KK'}$, and there are three shell coupling parameters $\Delta_{KK'}^{\nu\nu'}$. This makes for a total of 14 independent parameters.

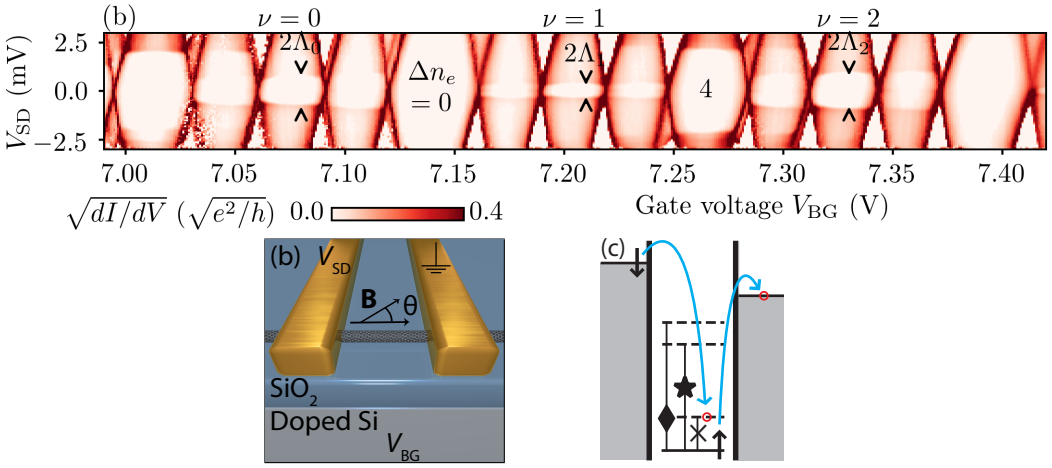

Figure 4.1: (a) Bias spectroscopy data in the conductance band. Diamond heights exhibit four-fold periodicity indicating filling of spin and valley degenerate shells whose indices are shown with ν. The magnitude of the zero-field Kramers doublet splittings can be identified from the onset of inelastic cotunneling, highlighted as $\Lambda_\nu = \sqrt{(\Delta^\nu_{\mathrm{SO}})^2 + (\Delta^\nu_{KK'})^2}$. The colormap is shown as $\sqrt{dI/dV}$ rather than dI/dV to emphasize these onsets whose conductance jumps are small relative to sequential tunneling conductance. (b) Schematic of device (not to scale). (c) Schematic of inelastic cotunneling spectroscopy which is used to probe the spectrum of the nanotube quantum dot. Markers refer to Fig. 4.2 at 5 T.

In summary, the model describes three shells, each with two Kramers doublets. Parameters or excitations that involve more than one shell (Kramers doublet) are termed inter-shell (inter-Kramers). Correspondingly, we use intra-shell (intra-Kramers) within a shell (Kramers doublet).

Methods

Fig. 4.1(b) shows the simple two-terminal geometry of the device. The nanotube is grown using chemical vapor deposition (CVD)[89] on a doped Si chip with a 500 nm capping layer of SiO_2. Subsequently, electrodes are defined with electron-beam lithography so that they are bridged by the nanotubes at random. The electrodes consist of Au/Pd (40/10 nm).

Rotation of the magnetic field in the x-z plane was achieved using a piezoelectric rotator. Standard lock-in techniques were used to obtain dI/dV. The lock-in conductance was differentiated numerically to obtain d^2I/dV^2. Measurements were done at a temperature of 100 mK in a ^{3}He/^{4}He dilution refrigerator.

The CNT spectrum was probed with inelastic cotunneling spectroscopy to obtain the excitation spectrum. In this technique the applied voltage V_{SD} is increased at a fixed magnetic field with the device in Coulomb blockade

until it matches the energy difference between two levels. At this voltage a second-order tunneling process such as the one sketched in Fig. 4.1(c) is allowed which causes an increase in conductance. Numerically taking the derivative of the conductance subsequently yields peaks where V_{SD} matches energy differences.

Experimental Results

Initial characterization of the device using bias spectroscopy is shown in Fig. 4.1(a). We plot $\sqrt{dI/dV}$ rather than dI/dV to highlight the onset of inelastic cotunneling. The heights and widths of the Coulomb diamonds are seen to be approximately four-fold periodic, reflecting the filling of Kramers doublets in the nanotube shells. We label the electron filling of the dot by $\Delta n_e \equiv n_e - n_{e,0}$ and estimate $n_{e,0} \approx 40$. At half-filling of shell ν ($\Delta n_e = 2$) the onset of inelastic cotunneling is marked on the figure as $\Lambda_\nu = \sqrt{(\Delta^\nu_{\mathrm{SO}})^2 + (\Delta^\nu_{KK'})^2}$. We estimate the charging energies $U = 7$–8 meV and level spacings $\Delta E = 2$–4 meV.

In order to investigate the shell couplings of the nanotube spectrum we do inelastic cotunneling spectroscopy in shell $\nu = 1$ for various fillings, magnetic field strengths and angles. The model in (4.7) is fitted to the data by manually iterating the parameters and visually inspecting the goodness-of-fit. The bias spectroscopy data in Fig. 4.1(a) fixes some parameters and/or constrains the parameter space by providing Λ_ν and level spacings. Additionally, some intra-shell parameters are determined as in previous studies [22] from data at low magnetic field where inter-shell couplings are negligible. We find parameter values consistent with those previously reported [17, 18, 81, 19, 90, 91]. Since $\Delta_{\mathrm{SO}} \ll \Delta_{KK'}$ in all shells we can treat spin as an approximately good quantum number. This means that the two time-reversed states in a Kramers doublet have approximately opposite spin.

For fillings $\Delta n_e = 0, 1$ the obtained spectrum and data for parallel magnetic field are shown in Fig. 4.2. In the calculated spectrum in Fig. 4.2(a) occupied (empty) energy levels are indicated by solid (dashed) lines. Thus, the spectrum corresponds to a filling of $\Delta n_e = 1$ as noted in the top left corner of the figure. Excitations are shown with vertical lines and a marker, but only between occupied and empty levels. This means that some excitations for, e.g., $\Delta n_e = 0$ are not shown in Fig. 4.2(a) because they involve two filled or two empty levels. The parameters for the spectrum can be found in Table 4.1. Note that all three panels in Fig. 4.2 share the same set of parameter values.

The experimental excitations in Fig. 4.2(b),(c) are all captured accurately by the model. At low magnetic field in Fig. 4.2(c) ($\Delta n_e = 1$) the expected excitations are observed: The intra-Kramers excitation starts at zero energy due to the required degeneracy at $B = 0$ and the two inter-Kramers excita-

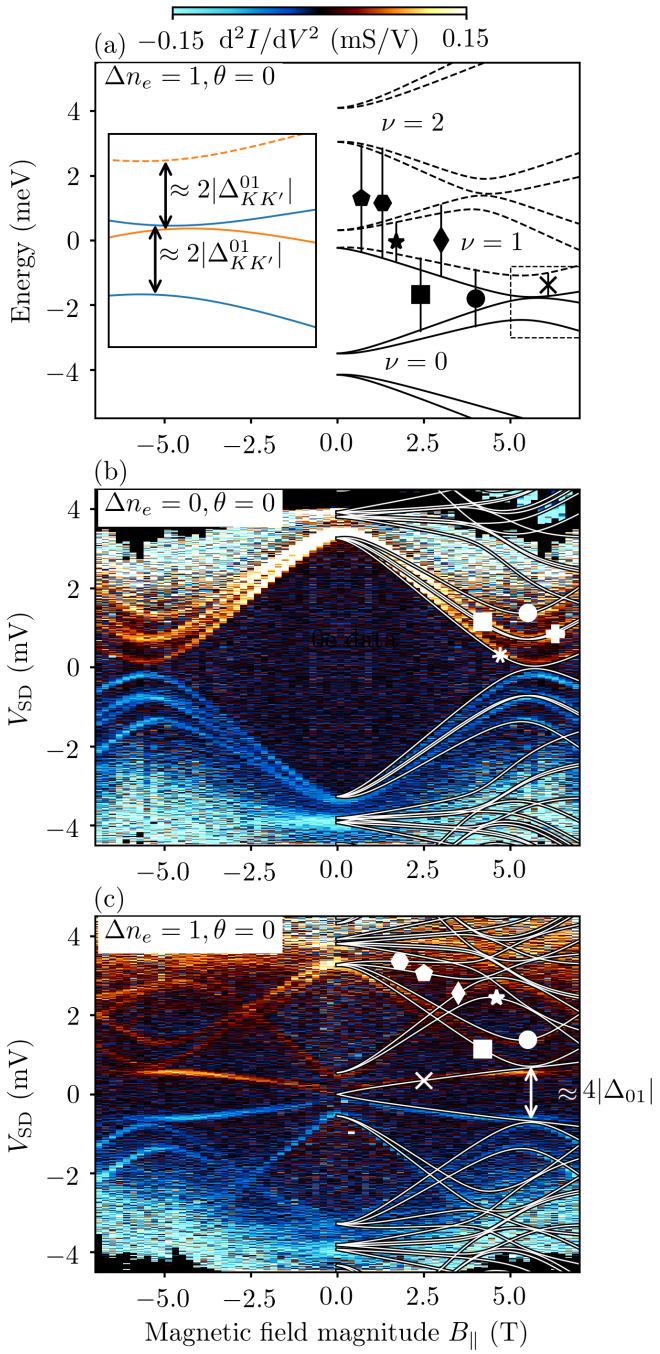

Figure 4.2: (a) Spectrum of the three nanotube shells as a function of magnetic field strength obtained from fitting (b) and (c) to the model in eq. (4.7). Solid (dashed) lines indicate filled (empty) states. The inset shows how the $\nu = 0, 1$ anticross magnitude depends on the inter-shell parameter Δ_{01}. (b) and (c) Inelastic cotunneling spectroscopy in the center of Coulomb diamonds $\Delta n_e = 0e, 1$ as a function of magnetic field strength. The excitation spectrum is calculated from level differences in (a) and overlaid on the data. Excitations are identified by markers for easy comparison between model and data. Note that markers for high-energy excitations are left out for clarity.

Table 4.1: Parameters obtained from fitting inelastic cotunneling data in figures 4.2, 4.3 and 4.4. The parameters for 0 and 1 electrons in shell 1 are different from those for 2, 3 and 4 electrons. This can be explained by a change in the electrostatic potential along the nanotube. All values are in meV except $g_{\rm orb}$-values which are dimensionless.

shell	$\nu=0$			$\nu=1$			$\nu=2$		
parameter	$\Delta_{\rm SO}$	$\Delta_{KK'}$	$g_{\rm orb}$	$\Delta_{\rm SO}$	$\Delta_{KK'}$	$g_{\rm orb}$	$\Delta_{\rm SO}$	$\Delta_{KK'}$	$g_{\rm orb}$
$\Delta n_e = 0,1$	0.0	0.9	-6.4	0.07	0.45	-5.5	0.0	0.9	-8.7
$\Delta n_e = 2,3,4$	0.0	0.9	-6.4	0.07	0.45	-6.2	0.0	0.9	-6.2
difference	–	–	–	–	–	-0.7	–	–	$+2.5$

shell	Inter-shell parameters				
parameter	ΔE_{01}	ΔE_{12}	$\Delta^{01}_{KK'}$	$\Delta^{12}_{KK'}$	$\Delta^{02}_{KK'}$
$\Delta n_e = 0,1$	3.7	3.5	0.4	0.2	0.4
$\Delta n_e = 2,3,4$	3.7	2.9	0.5	0.25	0.75
difference	–	-0.6	$+0.1$	$+0.05$	$+0.35$

tions initially at Λ_1 split with approximately the electron g-factor. The fact that $\Delta_{\rm SO}$ is finite can be deduced by comparing the lowest excitation in Fig. 4.2(c) ($\Delta n_e = 1$) with the one in Fig. 4.3(c) ($\Delta n_e = 3$). The former is convex while the latter is concave.

Conversely, at low magnetic field no low-energy, intra-shell excitations are available for a $\Delta n_e = 0$ in Fig. 4.2(b) since all states in the $\nu = 1$ shell are empty and the lowest excitation energy must therefore include a level spacing. By increasing the magnetic field the upper (lower) Kramers doublet in shell $\nu = 0$ ($\nu = 1$) are gradually brought closer until they anticross at $B_\parallel \approx 6$ T. In Fig. 4.2(c) the same behavior for inter-shell excitations (square and circle) is observed. In fact, the square and circle excitations have exactly the same energy in Fig. 4.2(b) as in (c) since the parameters do not change between these two panels.

The anticross between shells $\nu = 0$ and $\nu = 1$ is shown in detail in the inset of Fig. 4.2(a). Blue levels anticross with blue, and orange with orange. Blue levels do *not* anticross with orange levels since they have opposite spin. This prediction is confirmed by the data in Fig. 4.2(c) and Fig. 4.3(c) where the square and cross excitations do not repel each other to within the spectroscopic linewidth which is much smaller than the relevant inter-shell couplings $\Delta^{01}_{KK'} = 0.4$ meV and $\Delta^{12}_{KK'} = 0.2$ meV. The same behavior is shown in the model at $B_\parallel \approx 5.5$ in Fig. 4.3(a), but this transition cannot be observed in the data because of noise. The anticross magnitude is proportional to $|\Delta^{01}_{KK'}|$ as indicated by arrows. This magnitude is directly observable as $\approx 4|\Delta^{01}_{KK'}|$ in the data in Fig. 4.2(c) at $B_\parallel \approx 5.5$ T. Due to the finite spin-orbit coupling $\Delta^{\nu=1}_{\rm SO} \neq 0$ the anticrosses occur at slightly different magnetic fields.

The anticross between shells $\nu = 1$ and $\nu = 2$ is predicted by the spectrum in Fig. 4.2(a) to be similar to the $\nu = 0, 1$ one. Since all excitations involving the $\nu = 1, 2$ shell anticrosses are high in energy we cannot directly confirm

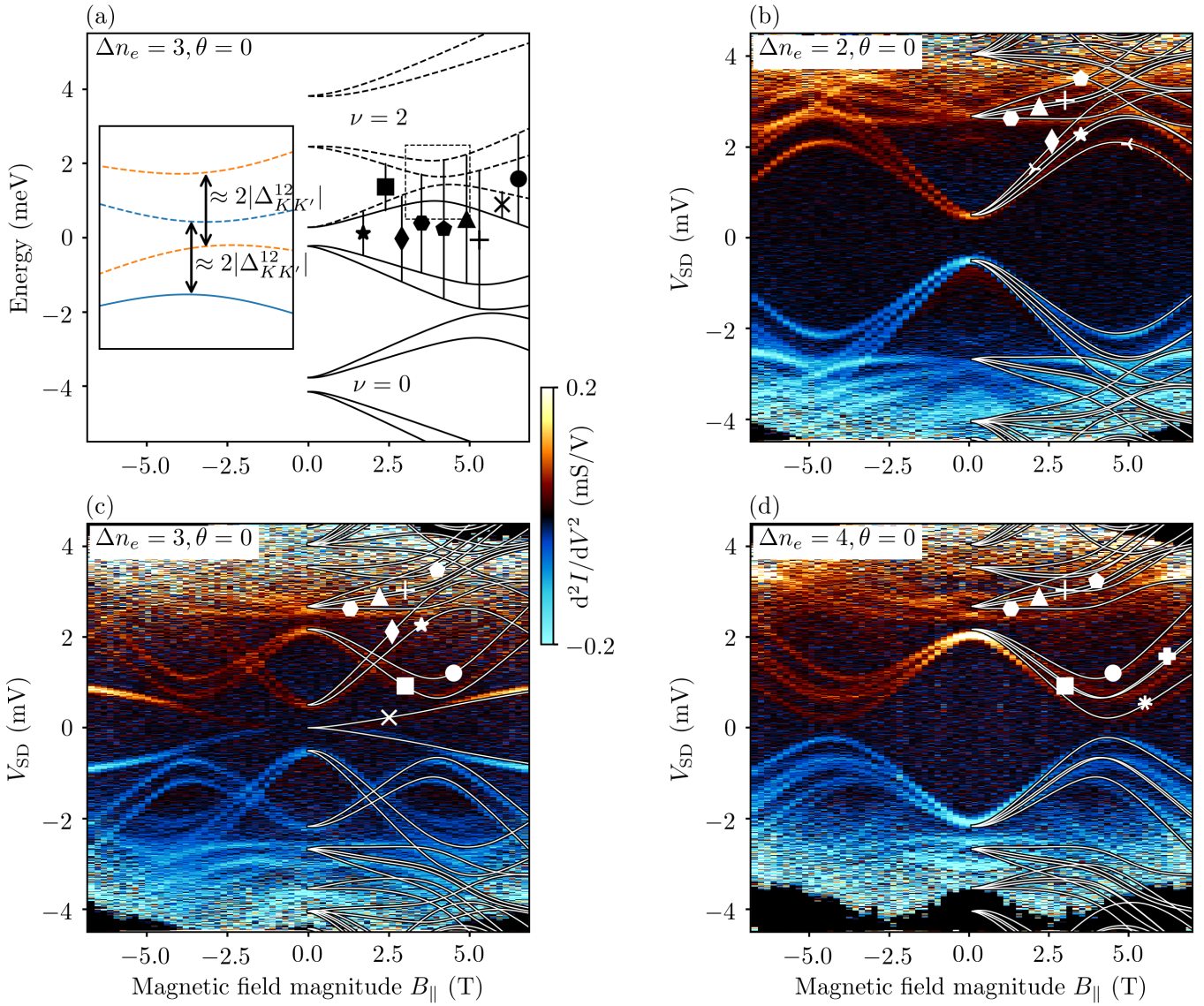

Figure 4.3: Same as Fig. 4.2 for $\Delta n_e = 2, 3$ and 4 in shell 1. Note that in (a) only excitations between filled and empty states for a filling of 3 electrons are marked. This means that some marks in (b) and (d) are not found in (a).

this in the data due to noise and smearing at high V_{SD}. Thus, in Fig. 4.3 we repeat the procedure for fillings $\Delta n_e = 2, 3, 4$. Markers have been retained between Fig. 4.2 and Fig. 4.3 for the excitations that are present in both figures. The agreement between theory and data is again good, although we find that some parameters must be adjusted for these new fillings to provide a good fit. The parameters for Fig. 4.3 are shown in Table 4.1 along with the difference in parameter values between the two shells. Most notable is the change in $g_{\mathrm{orb}}^{\nu=2}$ of +2.5 and $\Delta_{KK'}^{02}$ of +0.35 meV. Adding electrons to the dot may change the electrostatic potential along the tube. This may explain the change in inter-shell parameters which are determined by $V(z)$. The changes in g_{orb} can be explained by a shift in the wave function density along the tube so that the electron spends more time in a segment of the tube with a larger diameter.

Two features in the data in Fig. 4.3 are unaccounted for in the model: At low magnetic field in Fig. 4.3(b) ($\Delta n_e = 2$) at $V_{\mathrm{SD}} \approx 2$ mV a faint excitation is visible, gradually fading out below $B_{\parallel} = 1$ T. This excitation looks like the square and circle excitations from Figs. 4.3(c),(d) but it should not be present in the $\Delta n_e = 2$ excitation spectrum since the corresponding states are all empty.

The other unexplained feature concerns the diamond and asterisk intra-Kramers excitations in Fig. 4.3. These excitations arise from taking an electron from either occupied state in the lower Kramers doublet and putting them in the unoccupied state in the upper Kramers doublet. These excitations arise from tunneling processes where an electron tunnels out of either occupied state in the lower Kramers doublet and an electron tunnels into either unoccupied state in the upper Kramers doublet. Thus, only two excitations are possible which is consistent with the data up to about $B_{\parallel} \approx 2.5$ T. Here, however, the degenerate excitations split in energy to reveal three excitations, the lowest of which is not captured in the model (this is most visible at negative V_{SD}).

To further verify the extracted parameters Fig. 4.4 shows excitation spectroscopy data for perpendicular orientation of the magnetic field (Fig. 4.4(a),(c)) and rotation of the magnetic field (Fig. 4.4(b),(d)), both for a filling of $2e$. The parameters used are the same as in Fig. 4.3. Again, the correspondence between data and theory is good. We highlight the good correspondence of the ♦ excitation in Fig. 4.4. This excitation involves two levels with approximately opposite spin so their separation is expected to increase proportional to g_{s}. Although g_{s} is not a free parameter in the model the fit is still good.

The splitting of the states in Fig. 4.4(a),(c) is smaller than in previous figures since a perpendicular magnetic field does not couple to the orbital motion around the nanotube. Consequently, no shell anticrosses are visible and we instead show intra-shell anticrosses caused by Δ_{SO} which in the case of shell $\nu = 0$ is zero to within the spectroscopic linewidth.

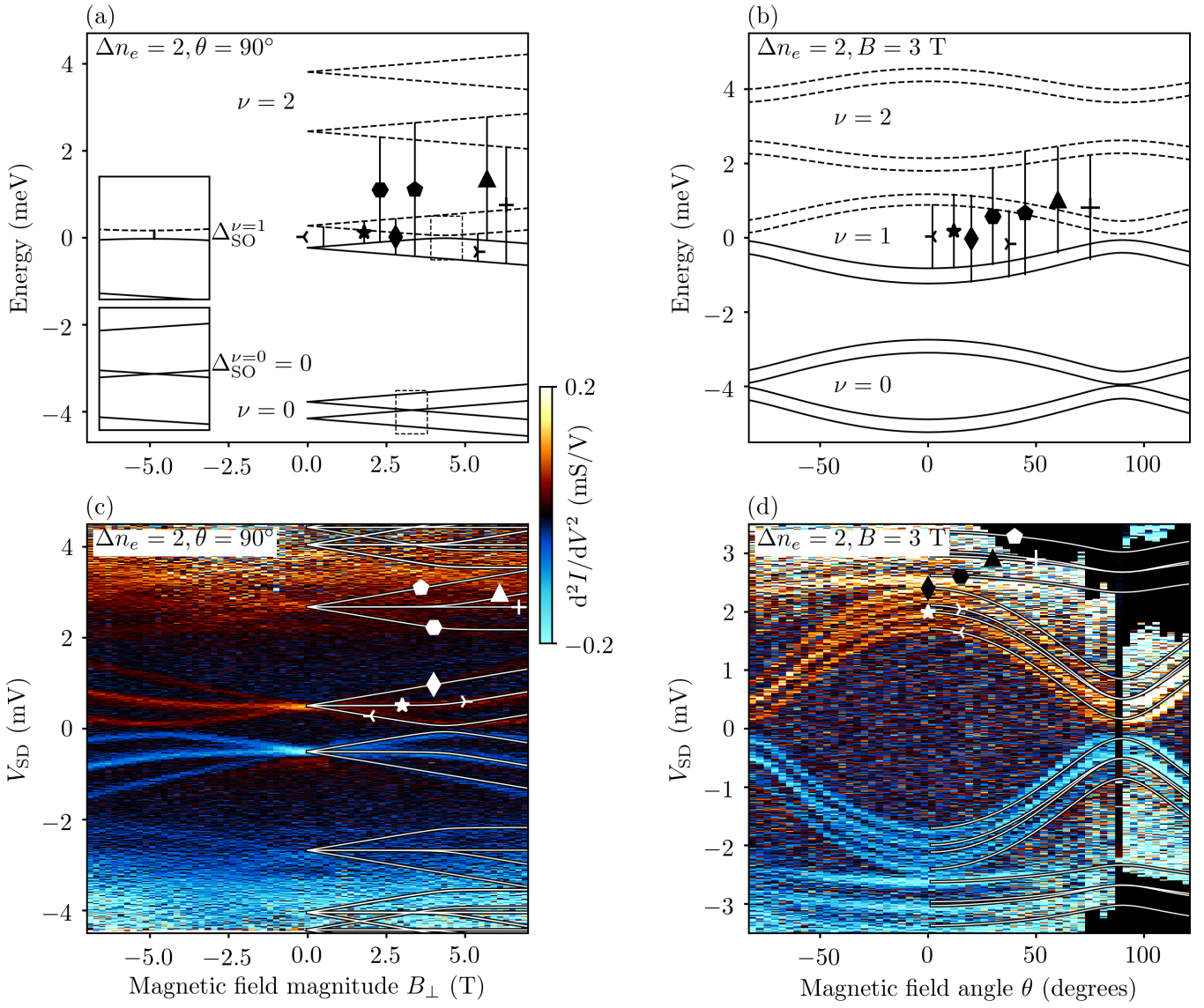

Figure 4.4: Same as Fig. 4.3, but for (a), (c) $\theta = 90°$ and (b), (d) magnetic field rotation. The insets in (a) show spin-orbit induced anticrosses, one of which is a crossing since $\Delta_{\mathrm{SO}}^{\nu=0} = 0$. These (anti)crossings are unrelated to shell couplings since they occur for states which belong to the same shell. In (b) no inset is shown since there are no "simple" single parameter anticrosses.

In Fig. 4.4(d) the fact that the ➢ and ★ excitations have a finite splitting in parallel field and no splitting in perpendicular field is another indication of the finite spin-orbit coupling. At perpendicular field (see Fig. 4.4(a)) the orbital motion does not couple to the magnetic field. The resulting energy levels are split purely by spin, leading to particle-hole symmetry and consequently to degenerate excitations. Conversely, at parallel magnetic field (Fig. 4.3(a)), spin-orbit interaction causes a slight asymmetry between the upper and lower Kramers doublet and a corresponding splitting of the ➢ and ★ excitations.

No inset is shown in Fig. 4.4(b) since no "simple" single-parameter anti-crosses are visible here.

Conclusion

In conclusion, we have studied experimentally and theoretically the coupling between three shells in a carbon nanotube quantum dot. The results show that the evolution of the energy levels can be accurately captured by extending an existing model. Contrary to expectations, we find that some inter-shell parameters and orbital g-factors in the model change when adding the second electron to one of the considered shell. The change in inter-shell parameters can be explained by a change in the electrostatic potential caused by the added electron. The change in g_{orb} is harder to explain, although the changing potential may also affect the wave function density along the tube and hence g_{orb}.

Acknowledgments

We thank Bernd Braunecker for fruitful discussions and acknowledge the financial support from the Carlsberg Foundation, the European Commission FP7 project SE2ND, the Danish Research Councils and the Danish National Research Foundation.

Chapter 5

Non-collinear spin-orbit magnetic fields in a carbon nanotube double quantum dot

This chapter is published as

M. C. Hels, B. Braunecker, K. Grove-Rasmussen, and J. Nygård. Non-collinear spin-orbit magnetic fields in a carbon nanotube double quantum dot. Phys. Rev. Lett., 117:276802, Dec 2016. [22].

5.1 Main text

Abstract

We demonstrate experimentally that non-collinear intrinsic spin-orbit magnetic fields can be realized in a curved carbon nanotube two-segment device. Each segment, analyzed in the quantum dot regime, shows near four-fold degenerate shell structure allowing for identification of the spin-orbit coupling and the angle between the two segments. Furthermore, we determine the four unique spin directions of the quantum states for specific shells and magnetic fields. This class of quantum dot systems is particularly interesting when combined with induced superconducting correlations as it may facilitate unconventional superconductivity and detection of Cooper pair entanglement. Our device comprises the necessary elements.

Main text

Controlling local magnetic fields on the nanoscale is currently of strong interest in quantum information and spintronics. Local fields are important for operating spin quantum bits, spin-filters and realizing topological states of matter. Several approaches to address the spin degree of freedom in this manner have been pursued involving techniques based on on-chip strip lines [92],

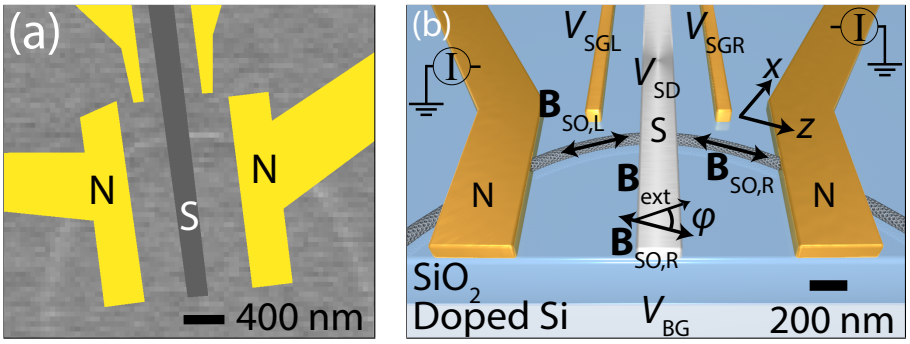

Figure 5.1: **(a)** SEM image of nanotube with Au normal leads (50 nm), a Ti/Al superconducting lead (5/15 nm) and two side gates. Note that the lead geometries are overlaid on the image digitally. **(b)** Schematic of the device. The angle φ reflects the angle between the external magnetic field $\mathbf{B}_{\text{ext}}$ and the tangent of the midpoint of the right nanotube segment. A rigorous definition of φ is given below. Note that $\mathbf{B}_{\text{ext}}$ is constricted to the x-z-plane. The expected valley-dependent directions of the spin-orbit magnetic fields $\pm\mathbf{B}_{\text{SO,(L/R)}}$ are indicated by the two-headed arrows.

nuclear spin ensembles [93], micromagnetic stray [94, 95, 96] and exchange fields [97, 98], g-factor engineering [99] and spin-orbit coupling [100, 101].

A particularly interesting situation arises in double dots coupled to a central superconducting electrode. Here the control of the local spin directions, inducing non-collinear spin projection axes for the two dots, is predicted to give rise to unconventional superconductivity [42], poor man's Majorana physics [102] and novel schemes for transport based spin-entanglement detection of Cooper pairs [10].

These geometries can favorably be realized with carbon nanotubes when utilizing spin-orbit interactions (SOI) [17, 81, 82, 83, 103, 104] to control [76] and filter spins [78]. In contrast to other quantum dot systems (e.g. semiconducting nanowires), the effect of SOI on the four-fold degenerate energy spectrum (due to spin $s = \uparrow, \downarrow$ and valley $\tau = K, K'$) of nanotubes is well-understood [24] and gives rise to spin-orbit magnetic fields oriented along the nanotube axis. In this Letter we demonstrate the realization of non-collinear magnetic fields using the spin-orbit fields in a bent carbon nanotube [75, 105, 106, 77, 76, 19] double quantum dot connected in parallel between the superconductor and two normal leads. The non-collinearity of the fields originates from the geometry-defined angle between the two quantum dot tube segments. Furthermore, the spin alignment can be controlled and rotated by applying an external magnetic field.

In this paper we present data from the hybrid carbon nanotube device [11] shown in Fig. 5.1(a). Nanotubes are grown using chemical vapor deposition [89] (CVD) on a doped Si chip with a 0.5 μm thermal oxide cap. In the growth process nanotubes are bound to the substrate in random orientations

by van der Waals forces. Many of the tubes are in this way fixated in curved configurations. The nanotubes are subsequently located using scanning electron microscopy (SEM) at an acceleration voltage of 1.5 kV and metal leads are defined by e-beam lithography at 20 kV. The two nanotube segments are 450 nm long and the superconducting lead (5 nm Ti sticking layer with 15 nm Al on top) is 240 nm wide.

The measurement configuration is indicated in Fig. 5.1(b). The superconducting lead is voltage biased and the normal leads are grounded through current amplifiers so that the nanotube segments are measured in parallel. Standard lock-in techniques and differentiated DC current were used to obtain $\mathrm{d}I/\mathrm{d}V$. The lock-in conductance was differentiated numerically to obtain $\mathrm{d}^2I/\mathrm{d}V^2$. Measurements were done at a base temperature of 30 mK.

Bias spectroscopy plots for the two nanotube segments are shown in Figs. 5.2(a),(c). In both plots Coulomb resonances occur in sets of four reflecting the spin and valley degeneracy in carbon nanotubes at zero magnetic field (i.e., the shells g-e, M-O are (near) four-fold degenerate) [24]. Coulomb blockade in shell f in the left dot and shell M and O in the right dot is lifted by the SU(2) Kondo effect which is visible as zero-bias conductance resonances at electron fillings 1 and 3. In shell e in the left dot the lead-dot coupling is so strong that all four states participate in an SU(4) Kondo state which gives rise to a zero-bias conductance resonance for all fillings in the shell [24]. About 35 (60) shells are observed in the left (right) dot indicating that the nanotube is of high quality even though we do not employ an ultraclean fabrication procedure [24]. The right dot has a charging energy $U_\mathrm{R} \approx 9\,\mathrm{meV}$ and the left dot has a charging energy $U_\mathrm{L} \approx 6\,\mathrm{meV}$. In Fig. 5.2(b),(d) bias spectroscopy plots at low V_SD reveal a soft superconducting gap $\Delta_\mathrm{SC} \approx 60\ \mu\mathrm{eV}$ [46]. For $|V_\mathrm{SD}| < \Delta_\mathrm{SC}/|e|$ transport takes place via Andreev reflections.

A narrow band gap is identified at $V_\mathrm{BG} \approx 0\,\mathrm{V}$ from room temperature data. We define the lettering of the shells so that lower (upper) case letters count in the direction of negative (positive) V_BG starting with "a" ("A") at the band gap. Thus, the filling in, e.g., shell N in the right side is 53-56 electrons within the uncertainty of the band gap position.

We determine the electronic structure of a specific shell by inelastic cotunneling spectroscopy as sketched in Fig. 5.3(i). When eV_SD matches the energy difference between two levels in the nanotube there is an increase in conductance, i.e., a peak or a dip in $\mathrm{d}^2I/\mathrm{d}V_\mathrm{SD}^2$. By varying the magnetic field strength and direction for different fillings (backgate voltages) in a shell the evolution of the four levels can be fitted to a four-level model [24, 81, 87, 82, 83, 88, 107]. In this way we extract the spin-orbit energy Δ_SO, valley coupling $\Delta_{KK'}$, orbital g-factor g_orb and offset angle φ_SO for the spin-orbit magnetic field which is parallel to the tube axis. The parameters Δ_SO and g_orb depend on chirality which is, however, hard to determine.

SOI has the effect of lowering the energy of states with parallel spin and

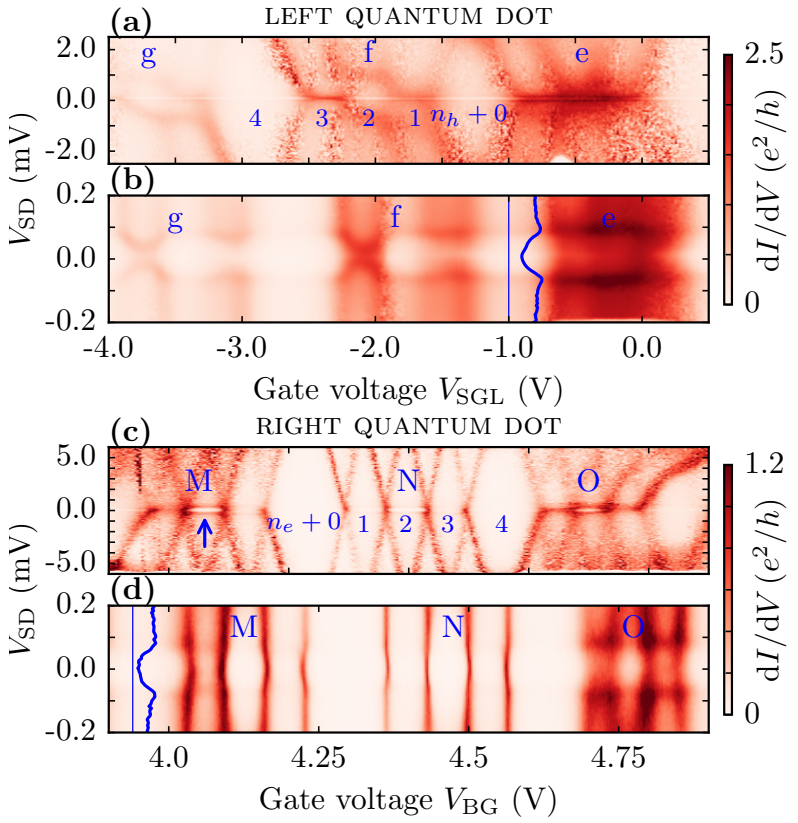

Figure 5.2: **(a),(c)** Bias spectroscopy of the left and right quantum dots showing charging energies of $U_L \approx 6\,\text{meV}$ and $U_R \approx 9\,\text{meV}$, respectively. Both dots show four-fold shell filling characteristic of carbon nanotubes. Kondo resonances caused by strong lead-dot coupling are visible at zero bias for multiple fillings. They are most pronounced in shell e in the left dot. The blue arrow shows the the onset of inelastic cotunneling close to zero bias in shell M. The dot filling is $n_e = 53$-56 electrons for shell N and $n_h = 20$ holes for shell f. **(b),(d)** A superconducting gap is visible in both dots with a magnitude of about 60 μeV. Cuts in (c) and (d) show the superconducting gap.

orbital magnetic moments. For the electron spin this is equivalent to the effect of a local magnetic field with opposite direction for the K and K' states. Thus, in zero magnetic field with only SOI present the four-fold degenerate states split into two doublets. Introducing disorder $\Delta_{KK'}$ couples K and K' states and opens avoided crossings. With both SOI and disorder present neither spin nor valley is a good quantum number.

Fits for shell N are shown in Fig. 5.3 with excellent correspondence between spectroscopic data and model. In particular the electron-hole symmetry within the shell is seen to be broken by comparing (a) and (c) (see Fig. 5.3(h)). For this shell we find $\Delta_{\mathrm{SO}} = 120\text{-}170\ \mu\mathrm{eV}$, $\Delta_{KK'} = 50\text{-}100\ \mu\mathrm{eV}$, $|g_{\mathrm{orb}}| = 2.4\text{-}2.9$ and exchange splitting $J = 50\text{-}200\ \mu\mathrm{eV}$, which are consistent with values previously reported [17, 18, 81, 19, 90, 91]. Some transitions are not visible in the magnetic field angle sweeps because of noise. The offset angle for shell N, $\varphi_{\mathrm{SO}}^{\mathrm{N}}$ is chosen as the zero-point of φ so that $\varphi_{\mathrm{SO}}^{\mathrm{N}} \equiv 0$. This angle is found to coincide with the tangent of the midpoint of the right segment in the SEM image within experimental uncertainty.

Interestingly, shell N is spin-orbit dominated by having $\Delta_{\mathrm{SO}} > \Delta_{KK'}$. A nanotube in this regime is not normally obtained in devices that are not ultraclean since exposing the nanotube to lithographic processing typically introduces disorder. The property of being spin-orbit dominated shows up clearly in the difference between Fig. 5.3(a) and (c) which would be identical [81] for $\Delta_{\mathrm{SO}} = 0$. With SOI the two highest-energy levels cross at the spin-orbit magnetic field $B_{\mathrm{SO}} \equiv \Delta_{\mathrm{SO}}/g_{\mathrm{s}}\mu_{\mathrm{B}}$. Disorder does not cause an anti-crossing here since the two states belong to the same valley. However, the spin-flip scattering by an external magnetic field $\mathbf{B}_{\mathrm{ext}}$ making an angle Θ with $\mathbf{B}_{\mathrm{SO}}$ causes an anti-crossing of Δ_Θ [18] which is observed in Fig. 5.3(c).

Of particular interest is the angle $\varphi_{\mathrm{SO}}^{\nu}$ between the directions of the intrinsic spin-orbit magnetic field in a given shell ν and N. The $\varphi_{\mathrm{SO}}^{\nu}$ are extracted from magnetic field angle sweeps by identifying the angle with which the fit must be offset for it to correspond to the data. The model does not take into account the curving of the tube and thus $\varphi_{\mathrm{SO}}^{\nu}$ represents an effective angle dependent on the position of the wave function of each shell ν. This interpretation implies that $\varphi_{\mathrm{SO}}^{\nu}$ is the same for levels in the same shell, which is consistent with the data.

We now want to establish that the $\varphi_{\mathrm{SO}}^{\nu}$ are, indeed, different in the two nanotube segments. Figure 5.4 shows a comparison between excitation spectroscopy for shell h in the left segment and shell N in the right segment (shell N is also shown in Fig. 5.3). In this figure the minimum of the second (first) transition for shell h (N) can be identified as the angle where the external magnetic field is oriented perpendicular to the spin-orbit magnetic field. The minimum occurs because the magnetic field couples minimally with the orbital magnetic moment in the nanotube at perpendicular orientation. We find that the spin-orbit magnetic field angles $\varphi_{\mathrm{SO}}^{\mathrm{h}} = 109^\circ - 90^\circ = 19^\circ$ and

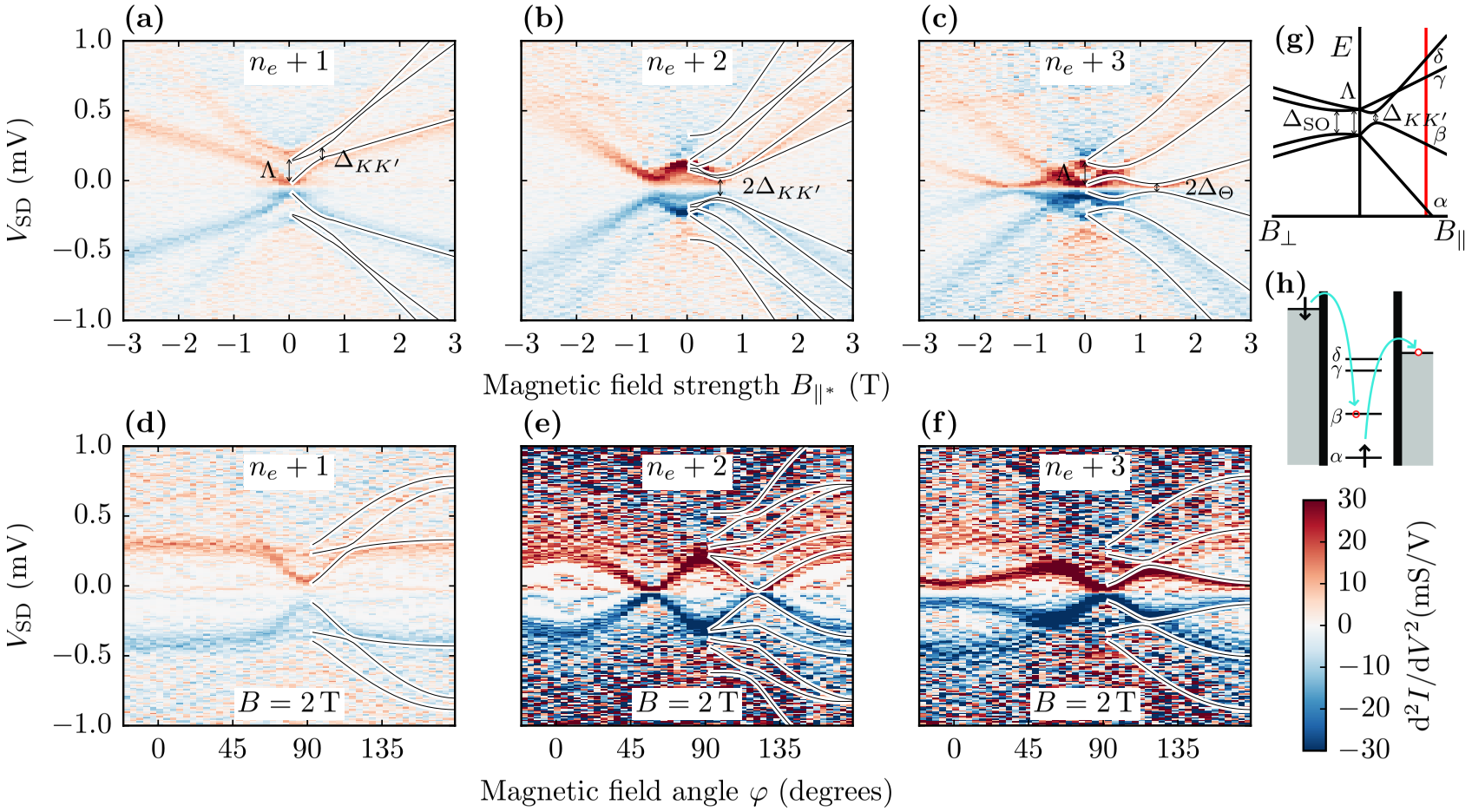

Figure 5.3: Excitation spectroscopy of shell N in the right dot. **(a)-(c)** In the top row the magnetic field magnitude is swept with the field aligned $-11°$ away from parallel orientation (denoted by $\|^*$). The misalignment does not change the spectrum qualitatively compared to parallel orientation. The zero-field splitting is denoted by $\Lambda = \sqrt{\Delta_{KK'}^2 + \Delta_{SO}^2}$. **(d)-(f)** Bottom row are magnetic field angle sweeps at 2 T. The electron filling n_e = 53-56. For all plots fitting parameters are $\Delta_{SO} = 150\ \mu$eV, $\Delta_{KK'} = 70\ \mu$eV, $J = 120\ \mu$eV, $|g_{orb}| = 2.6$. **(g)** Plot of the nanotube spectrum with the parameters for the shell shown. **(h)** Schematic of an inelastic cotunneling process involving level α and β at the red line in (h). This process is allowed when $|V_{SD}|$ is equal to or above the energy difference between levels α and β.

(by definition) $\varphi_{\rm SO}^{\rm N} = 0°$ are at an angle of 19° with respect to each other.

Similar sets of measurements of parallel, perpendicular and angular magnetic field sweeps have been made for nine other shells. The extracted angles $\varphi_{\rm SO}^{\nu}$ are plotted in Fig. 5.4 in which a clear clustering is seen with the $\varphi_{\rm SO}$-angles generally being smaller in the right dot. From the $\varphi_{\rm SO}^{\nu}$-values we estimate the average angle for the left and right segment $\varphi_{\rm SO}^{\rm av,(L,R)}$ and the difference between the averages $\Delta\varphi_{\rm SO}^{\rm av} = \varphi_{\rm SO}^{\rm av,L} - \varphi_{\rm SO}^{\rm av,R} = 21° \pm 3°$. This angle is visualized in the inset of Fig. 5.4 by tangents drawn on the nanotube segments. The large uncertainties in shells i, c and b are due to low $g_{\rm orb}$-values which reduces the curvature in the excitation spectroscopy plots [1].

The present device geometry allows for injection of Cooper pairs from the central superconducting electrode into the two dots. Ideally, as one electron tunnels into each dot, the Cooper pair is split into the two nanotube segments [13, 11], thereby injecting nonlocal spin-entangled electrons in the two dots [49]. This type of device may allow tests of a Bell inequality for Cooper pairs [2]. Notably, it has recently been proposed that with the bent nanotube geometry the effective magnetic field due to SOI and external field, can be used to configure levels with two spin projection axes per segment to act as spin filters for entanglement detection [10, 78, 58]. This scheme therefore requires a clear quantum dot shell structure, SOI, and a finite angle $\varphi_{\rm SO}$ between the spin-orbit fields for the two dots as shown above.

To address the spin projection axes we show in Fig. 5.5(a),(c) the spin expectation value $\langle \mathbf{S} \rangle$ for shells h and N as a function of external magnetic field angle φ based on the four-level model. For $\Delta_{KK'} = 0$, all quantum dot levels are fully spin polarized, with directions of $\langle \mathbf{S} \rangle$ that are different in the two quantum dots because of different $\varphi_{\rm SO}$ and $\Delta_{\rm SO}$. In reality $\Delta_{KK'}$ is always present, and the spin polarization is only partial. Nonetheless, as long as $\Delta_{KK'}$ remains smaller than the minimum energy difference δE between the levels with opposite valley in the same shell (see Supplemental Information), a detection of entanglement remains possible upon a prudent selection of angular ranges and magnetic field strengths, for which the polarizations remain close to full, e.g., as indicated in Fig. 5.5(b),(d) at $\varphi = -36°$. For systems as our sample, $\Delta_{KK'}$ should lie in the sub 100 μeV range to fulfill this requirement, which puts shell N in the good regime but would require further improvement for shell h. While challenging, this is within experimen-

[1] The data set consists of 77 sweeps similar to the six sweeps in Fig. 5.3. Only for the $n_e = 3$ sweep for shell d (i.e., one sweep out of 77) is the value for $\varphi_{\rm SO}$ inconsistent with the other sweeps for the shell. The correspondence between data and model for this particular sweep is not as good as for the remaining sweeps in this shell, even if the angle is chosen to fit only this shell. One explanation is that the longitudinal wave function for this filling is different from the other fillings.

[2] In such an experiment, the violation of a Bell inequality is not used to disprove local hidden variable theories [51], but as a proof of entanglement under the assumption that quantum mechanics is valid.

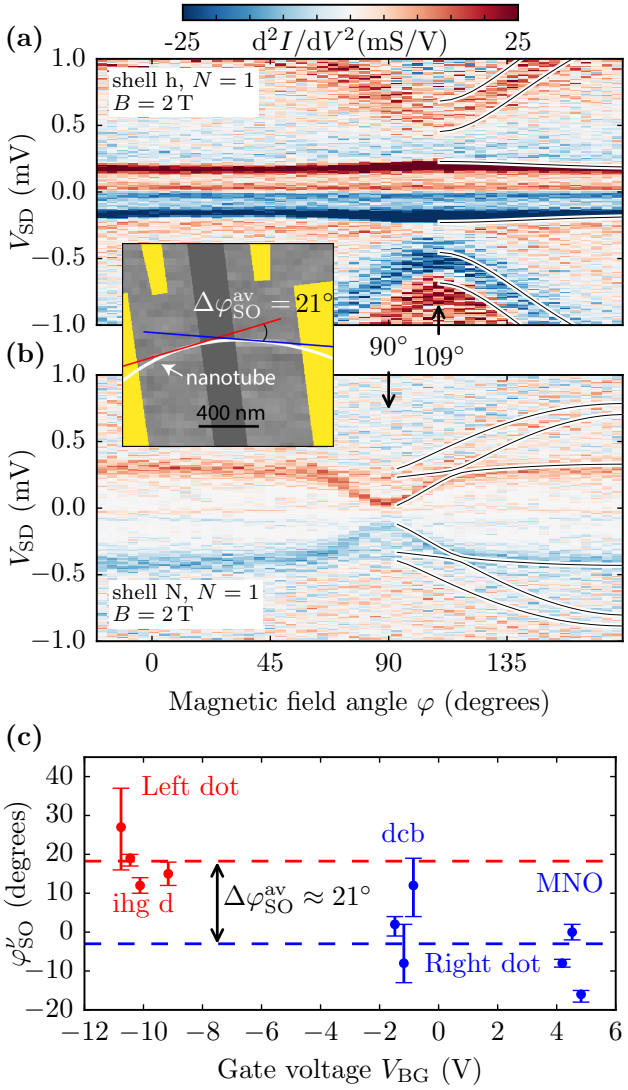

Figure 5.4: Excitation spectroscopy of **(a)** shell h in the left segment and **(b)** shell N in the right segment. Annotations show the angle where $\mathbf{B}_{\text{ext}}$ is oriented perpendicular to the spin-orbit magnetic field. This occurs for different angles in the two segments. **Inset**: SEM image of the device. The average angle difference between the left and right dot of 21° is illustrated by tangents drawn on the nanotube segments. Drawing the tangents at the segment midpoints would instead give $\Delta\varphi_{SO}^{av} \approx 32°$. **(c)** Spin-orbit magnetic field angles plotted for the shells measured. Red (blue) denotes left (right) segment. Dashed lines are averages of angles in a segment. Error bars are obtained as the minimum and maximum value for φ_{SO}^{ν} that make the model fit the data.

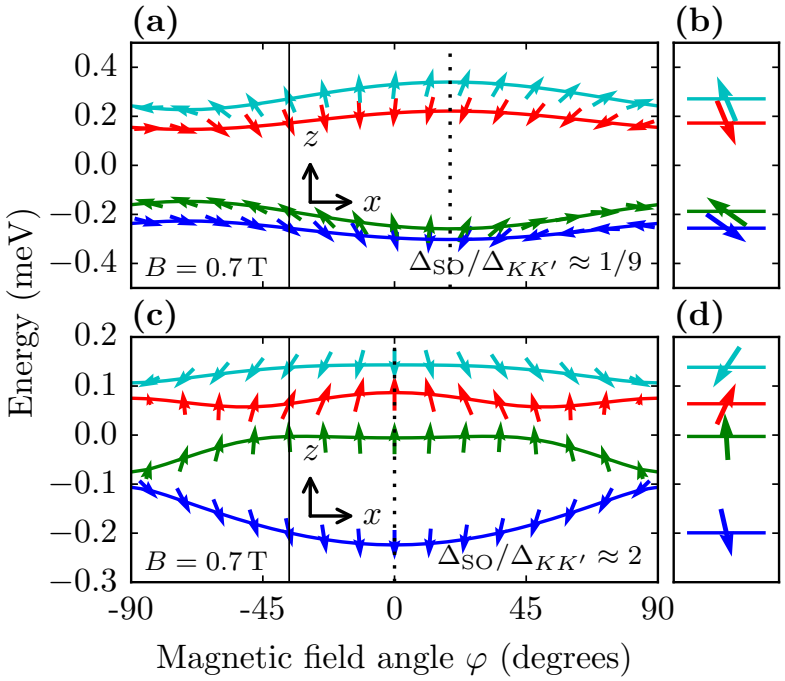

Figure 5.5: **(a),(c)** Spectrum and spin expectation value $\langle \mathbf{S} \rangle$ as a function of external magnetic field angle φ. **(b),(d)** Energy levels and $\langle \mathbf{S} \rangle$ at the position of the solid black lines in (a),(c). The model parameters are for shell h and shell N in (a),(b) and (c),(d), respectively. The spin vectors are shown in the x-z-plane since the effective magnetic field is constricted to this plane. The dotted vertical lines show the angle at which the magnetic field is parallel to the tube segment. All spins are shown in a global basis relative to shell N.

tal reach and shows that our device is close to fulfilling the conditions for an entanglement test. Furthermore, our theoretical understanding for $\Delta_{KK'} \neq 0$ (Supplemental Information) allows analysis even in the non-ideal regime.

In conclusion, we have shown that non-collinear spin-orbit magnetic fields with a significant average angle of over 20° degrees can be realized in a curved nanotube parallel double dot device. The underlying analysis of fits of the energy spectrum versus magnetic field allows for precise predictions of the spin orientation in the two quantum dots. Spin control has implications for several proposals coupling quantum dots to superconductors [102, 42, 108]. In particular, the distinctly non-collinear spin projection axes can be used for spin detection and future testing of spin-entanglement of split Cooper pairs [10].

Acknowledgments

We thank A. Levy Yeyati, and J. Paaske for fruitful discussions and acknowledge the financial support from the Carlsberg Foundation, the European Commission FP7 project SE2ND, the Danish Research Councils and the Danish National Research Foundation.

The research data supporting this publication can be accessed at [109].

5.2 Supplemental Information

The purpose of the Cooper pair splitter is to split entangled pairs that tunnel from the superconductor into the parallel quantum dots. Due to the special bent geometry of the CNT, the external field, and the intrinsic SOI magnetic fields pointing along the axes of the nanotube dots, the four energy levels in each dot have different alignment of the spin. Measuring the conductance product through different pairs of levels with different relative alignment of spin is similar to having different alignments of detectors in a traditional Bell test setup. For instance, for a parallel alignment of the polarizations on both levels the conductance over either level is suppressed as the splitting of spin singlets is blocked, whereas tuning the polarizations to an antiparallel alignment leads to an increase to a maximum conductance. Therefore the conductance itself is proportional to the spin correlation measurements required for the Bell inequality [10]. The appropriate addition of these conductances according to a Bell-type inequality reveals by violation of this inequality whether the Cooper pairs are entangled when tunneling out of the superconductor.

While we could clearly demonstrate that our device has spin polarized quantum dot levels, they are not fully polarized mainly due to scattering between the valleys K and K'. This degradation of the spin polarization has substantial influence on spin entanglement detection schemes and can lead

to erroneous conclusions. In this supplement we provide an estimate on the acceptable magnitude of the inter-valley scattering. Remarkably, our current device is close to fulfilling the necessary requirements for entanglement detection.

For transport measurements in the Cooper pair splitter, we shall focus on the entanglement detection scheme put forward in Ref. [10]. It relies on the violation of the CSHS Bell inequality

$$Q = |\langle S_K S'_K\rangle + \langle S_K S'_{K'}\rangle + \langle S_{K'} S'_K\rangle - \langle S_{K'} S'_{K'}\rangle| \leq 2, \tag{5.1}$$

which includes four nonlocal spin correlators obtained, as described below, by transport measurements through the different quantum dot levels. Equation (5.1) was originally designed to disprove, for instance, hidden variable theories. However, if we accept quantum mechanics, a violation of Eq. (5.1), i.e. a measurement of $Q > 2$, provides a sufficient demonstration of the existence of entanglement in the measured quantum states, which are in the present setup the split spin-entangled Cooper pairs.

This detection of entanglement is robust against most scattering processes and imperfections in either quantum dot, but can be falsified by inter-valley scattering $\Delta_{KK'}$ [10]. While the latter is unimportant for semiconducting nanotubes [10], it plays a limiting role for the small bandgap nanotubes used in the experiments. In the following we will use Q' to denote the result for Eq. (5.1) in the presence of $\Delta_{KK'}$ and use Q for the ideal, unperturbed value. In Fig. 5.6 we show Q' as a function of magnetic field rotation angle φ for the parameters of shells h and N provided in the main text, comparing the calculated values Q' for the experimentally determined $\Delta_{KK'}$ (dashed lines) with the optimal case of $\Delta_{KK'} = 0$ in both dots (solid lines), assuming the injection of spin singlet electron pairs in the Cooper pair splitter. Figure 5.6 shows that the valley mixing is dominating Q' and that the violation of Eq. (5.1) does not allow any conclusion on the entanglement of the injected electron pairs. In particular, the fact that Q' exceeds the maximally possible value $Q = \sqrt{8} \approx 2.83$ for spin correlators demonstrates that the spin reconstruction completely fails. The relevant question is therefore about the acceptable maximum $\Delta_{KK'}$ such that Eq. (5.1) remains trustworthy for entanglement detection.

In the following we answer this question by first identifying the situations in which $\Delta_{KK'}$ scattering can become decisive, which requires an investigation of the microscopic model of carbon nanotubes. This will provide us estimates on the acceptable magnitudes of $\Delta_{KK'}$. These estimates are then corroborated by some quantitative numerical examples. Our main conclusion is that even small bandgap nanotubes remain useful for entanglement detection under considerable amounts of inter-valley scattering, if a careful selection of the angular range is made where the individual levels remain energetically far apart with respect to the $\Delta_{KK'}$.

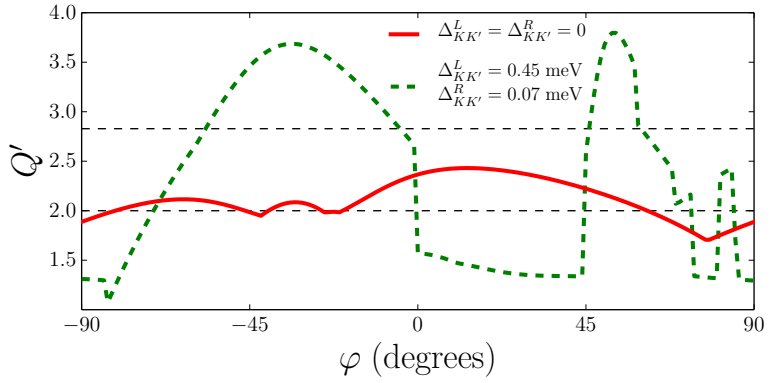

Figure 5.6: Values of Q', evaluated by Eq. (5.1) in the presence of $\Delta_{KK'}$, as a function of the magnetic field rotation angle φ, based on the effective model with the experimentally determined parameters for shells h (left quantum dot L) and N (right quantum dot R), computed for the splitting of spin-singlet entangled Cooper pairs at $B = 0.7$ T and the angle $\Delta\varphi_{\rm SO} = 21°$ between the quantum dot axes. The solid red line shows the ideal case $Q' = Q$ with $\Delta^L_{KK'} = \Delta^R_{KK'} = 0$, and shows over a wide range $2 < Q < \sqrt{8} \approx 2.83$ (between the dashed horizontal lines), demonstrating the potential of this Cooper pair splitter for entanglement detection. The dashed green line represents the same calculation of Q' in the presence of $\Delta^L_{KK'} = 0.45$ meV for shell h and $\Delta^R_{KK'} = 0.07$ meV for shell N, which are strong enough scattering amplitudes to destroy the resemblance with the red curve and lead even to $Q' > \sqrt{8}$ which would be impossible for spin correlators.

For the experiment presented this means that the right side (shell N) has sufficiently low valley mixing, while the left side (shell h) should be in the same regime, i.e. in the sub 100 μeV range. This is an experimentally challenging but feasible requirement. Furthermore, even for larger $K - K'$ coupling, the strong variations of Q seen in Fig. 5.6 may be tested and would provide insight into the applicability of the model and the assumption related to tunneling.

Effect of valley mixing on spin projections

If we neglect spin-orbit interaction (SOI), curvature and inter-valley scattering, the 4 levels of a quantum dot orbital, for 2 spin projections $s = +, - = \uparrow, \downarrow$ and 2 valley indices $\tau = +, - = K, K'$, have degenerate energies $E_{\tau,s}$. If we choose the spin S_z direction along the nanotube axis, SOI and curvature cause a partial lifting of the degeneracy, such that $E_{\tau,s} \neq E_{\tau,-s}$, but $E_{\tau,s} = E_{-\tau,-s}$ is maintained due to the time-reversal symmetry of the SOI. Nonetheless, the splitting can be interpreted as arising from a valley

dependent Zeeman field $\tau B_{\rm SO}\hat{\mathbf{z}}$, where $\hat{\mathbf{z}}$ is the unit vector along the nanotube axis. The further application of an external magnetic field $\mathbf{B}$ then creates an effective, valley dependent Zeeman field $\mathbf{B}_\tau^{\rm eff} = \mathbf{B} + \tau B_{\rm SO}\hat{\mathbf{z}}$. The orbital effect of the magnetic field causes a further valley dependent shift of the energy levels, expressible by an orbital g-factor $\tau g_{\rm orb}$ (with a positive or negative $g_{\rm orb}$ depending on whether the quantum dot is electron like or hole like) multiplying the z component of the magnetic field. Consequently, the effective Hamiltonian describing the quantum dot in a magnetic field takes the form

$$H_0 = E_0 + \frac{g_s}{2}\mu_B \mathbf{S}\cdot(\mathbf{B} + \tau_z B_{\rm SO}\hat{\mathbf{z}}) - \tau_z g_{\rm orb}\hat{\mathbf{z}}\cdot\mathbf{B}, \tag{5.2}$$

for E_0 an energy offset, $\mathbf{S} = (S_x, S_y, S_z)$ the vector of spin-Pauli matrices, and we will use $\tau_{x,y,z}$ for the valley Pauli matrices. Both Zeeman and orbital effects together cause a full lifting of the degeneracy, and hence allow the detection of each state individually. Due to the Zeeman term, each eigenstate is fully spin polarized, providing a projection onto $\pm S_\tau$ where $S_\tau = \hat{\mathbf{a}}_\tau\cdot\mathbf{S}$ for $\hat{\mathbf{a}}_\tau = \mathbf{B}_\tau^{\rm eff}/|\mathbf{B}_\tau^{\rm eff}|$ the unit vector parallel to $\mathbf{B}_\tau^{\rm eff}$. As shown in Ref. [10], the reconstruction of spin correlators through conductance measurements over these spin projective states can be used to probe the spin entanglement of Cooper pairs in a Cooper pair splitter setup through a Bell inequality as Eq. (5.1).

The requirement for a useful test of the Bell inequality are measurements along non-collinear spin projection axes $\hat{\mathbf{a}}_K$ and $\hat{\mathbf{a}}_{K'}$. A valley mixing scattering process with amplitude $\Delta_{KK'}$ leads to a hybridization between the different spin projected eigenstates. Spin is then no longer a good quantum number, and the interpretation of the Bell inequality becomes for large $\Delta_{KK'}$ meaningless. For a quantitative estimate, we need to investigate the effect of $\Delta_{KK'}$.

For this purpose, we must consider the Hamiltonian before attaining the effective model of Eq. (5.2). Following the notations of Refs. [87, 82], the Hamiltonian of a long carbon nanotube is given by

$$H_{\rm CNT} = \hbar v_F\Big(k_G\sigma_1 + k'\tau_z\sigma_2\Big) + \Big(\alpha\sigma_1 + \beta\tau_z\Big)S_z, \tag{5.3}$$

where v_F is the Fermi velocity, $\sigma_{1,2}$ the Pauli matrices referring to the A, B sublattice indices of the hexagonal carbon lattice, and α, β are the SOI coupling constants (denoted by $\Delta_{\rm SO}^1, \Delta_{\rm SO}^0$ in Ref. [24]), depending both on chirality and radius. The quantity $k' = k + \Delta k_{cv}^z$ denotes the sum of the longitudinal momentum k and a small curvature induced shift Δk_{cv}^z. Finally, $k_G = k_G^0 + \Delta k_{cv}^t$ provides the transverse quantized momentum, giving rise to the gap $E_G = 2\hbar v_F k_G$ between the subbands, with Δk_{cv}^t a curvature induced offset and $k_G^0 = (n - \tau m/3)/R$ for n the subband index, R the nanotube radius, and $m = (N_1 - N_2) \bmod 3$, for the chirality indices (N_1, N_2). The confinement potential of a quantum dot causes a further quantization of k'

and leads to the quantum dot levels that can be captured by the effective Hamiltonian H_0, with level depending $B_{\rm SO}$, E_0, and $g_{\rm orb}$.

For the lowest subband $n = 0$, it is important to notice that both k_G^0 and Δk_{cv}^t [87, 82] are proportional to τ and hence have opposite signs in opposite valleys (yet the final eigenvalues depend on the squares of these amplitudes and lead to similar energies in each valley). A valley mixing scattering potential of the form $H_{KK'} = \tau_x \Delta_{KK'}/2$ leads therefore to a mixing of components in the Hamiltonian that are characterized by the energy amplitudes $+E_G$ and $-E_G$. In the limit $|\Delta_{KK'}| \ll |E_G|$, the hybridization between the valleys can be expanded as a function of $\Delta_{KK'}/E_G$. With typical values $\Delta_{KK'} \sim 0.1$ meV, it is clear that for semiconducting nanotubes with $E_G \sim 100$ meV the effect of the hybridization is negligible [10], and Hamiltonian (5.2) as well as its consequences, for instance, on probing the Bell inequality remain unchanged.

However, for small gap nanotubes with $k_G^0 = 0$, the dominating role of E_G is replaced by a competition between $\Delta_{KK'}$ with the remaining curvature induced bandgap, the SOI coupling strength, the quantum dot confinement energy, and the orbital and Zeeman energies by the magnetic field, which all together lead to the effective magnetic splittings $|g_S \mu_B \mathbf{B}_\tau^{\rm eff}|$ and $|2 g_{\rm orb} \mu_B \hat{\mathbf{z}} \cdot \mathbf{B}|$. As long as $\Delta_{KK'}$ remains smaller than these scales, the loss of spin polarization by the valley mixing remains a small effect. It should be noticed that the curvature induced small gap $\hbar v_F \Delta k_{cv}^t$ depends on the nanotube diameter D as $\Delta k_{cv}^t \propto 1/D^2$, allowing us to achieve some tunability of $\mathbf{B}_\tau^{\rm eff}$ by choosing nanotubes with smaller or larger diameter.

The preceding observations can be quantified by adding the first order correction in $H_{KK'}$ to the wave functions,

$$|\psi_{\tau,s}\rangle = |\phi_{\tau,s}\rangle + \sum_{s'} \frac{\langle \phi_{-\tau,s'}| \, \Delta_{KK'} \tau_x \, |\phi_{\tau,s}\rangle}{E_{\tau,s} - E_{-\tau,s'}} \, |\phi_{-\tau,s'}\rangle \, , \tag{5.4}$$

where $|\phi_{\tau,s}\rangle$ and $E_{\tau,s}$ denote the eigenvectors and eigenvalues of H_0. If χ is the angle between $\hat{\mathbf{a}}_K$ and $\hat{\mathbf{a}}_{K'}$, we have $\langle \phi_{-\tau,s'}| \, \Delta_{KK'} \tau_x \, |\phi_{\tau,s}\rangle \propto \cos(\chi/2)$ for $s = s'$ and $\propto \sin(\chi/2)$ for $s \neq s'$. For general angles $\cos(\chi/2), \sin(\chi/2) \sim 1$, showing that the amplitude of the valley mixing part of the wave function is indeed set by $\delta_\tau = \Delta_{KK'}/\min_{s,s'}\{|E_{\tau,s} - E_{-\tau,s'}|\}$.

The ideal determination of spin expectation values is based on the projectors $P_{\tau,s} = |\phi_{\tau,s}\rangle \langle \phi_{\tau,s}|$, such that $P_{\tau,\uparrow} - P_{\tau,\downarrow} = S_\tau = \hat{\mathbf{a}}_\tau \cdot \mathbf{S}$. For a realistic measurement, the projection is obtained from restricting transport through a selected quantum dot level, for instance, by integrating the conductance over the resonance of the level. This results in a measured quantity $G_{\tau,s} \propto \langle \phi_{\tau,s}| \, \hat{\rho} \hat{I} \, |\phi_{\tau,s}\rangle$, where $\hat{\rho}$ is the density matrix of injected particles or Cooper pairs, and $\hat{I}$ the current operator. The spin reconstruction is then based on [10]

$$\frac{G_{\tau,\uparrow} - G_{\tau,\downarrow}}{G_{\tau,\uparrow} + G_{\tau,\downarrow}} = \langle S_\tau \rangle + \langle X_\tau \rangle, \tag{5.5}$$

where the division by the sum of the $G_{\tau,s}$ provides the normalization, $\langle S_\tau \rangle$ is the ideal spin measurement, and $\langle X_\tau \rangle \sim \delta_\tau$ is the error from valley mixing.

Spin correlation measurements in a Cooper pair splitting operation are obtained in a similar way. We use the notations above for the left quantum dot and use a tilde for the quantities of the right quantum dot. If $G_{\tau,s;\tilde{\tau},\tilde{s}}$ contains the nonlocal Cooper pair splitting amplitude, projected on states $|\psi_{\tau,s}\rangle$ on the left and $\left|\tilde{\psi}_{\tilde{\tau},\tilde{s}}\right\rangle$ on the right quantum dot [10], we have

$$\frac{\sum_{s,\tilde{s}} s\tilde{s} G_{\tau,s;\tilde{\tau},\tilde{s}}}{\sum_{s,\tilde{s}} G_{\tau,s;\tilde{\tau},\tilde{s}}} = \langle S_\tau \tilde{S}_{\tilde{\tau}} \rangle + \langle X_{\tau;\tilde{\tau}} \rangle, \tag{5.6}$$

with the error $\langle X_{\tau;\tilde{\tau}} \rangle \sim \max_{\tau,\tilde{\tau}}\{\delta_\tau, \tilde{\delta}_{\tilde{\tau}}\}$. The value Q in Eq. (5.1) then becomes $Q' = Q + \delta Q$ with the ideal result Q and the error

$$\delta Q = C \max_{\tau,\tilde{\tau}}\{\delta_\tau, \tilde{\delta}_{\tilde{\tau}}\}, \tag{5.7}$$

where C, with $|C| \gtrsim 1$, accounts for all further details and the sums and differences in Q.

With such a δQ the threshold for entanglement detection increases. Indeed, for an ideal measurement of Q, spin entanglement of injected electron pairs is detected if $Q \leq 2$ is violated. With a measured $Q' = Q + \delta Q$, this inequality becomes

$$Q' \leq 2 + |\delta Q|, \tag{5.8}$$

where we need to choose absolute values for δQ to rule out misinterpretations of $Q' > 2 - |\delta Q|$ but still $Q' < 2$ as proofs of entanglement. The latter equation gives an estimate on the necessary violation of the Bell inequality (5.1) for a valid detection of entanglement.

It should be stressed that for large $\Delta_{KK'}$ the perturbative result (5.7) is no longer limiting, and δQ can become large and, in particular, can lead to a Q' exceeding the possible maximum $Q = \sqrt{8}$ for spin correlators. The latter case is a strong indicator of a loss of spin polarization due to $\Delta_{KK'}$.

Quantitative numerical test

For a quantitative check of the estimate in Eq. (5.8) we investigate the influence of $\Delta_{KK'}$ on two models of the type as discussed above. As the first example, we consider a nanotube with chirality (24,12) in a magnetic field of $B = 1$ T, in a bent Cooper pair splitter setup as considered in Ref. [10]. The calculation of the quantum dot levels follows then from Eq. (5.3) in the presence of confining gates defining dots with a length of 450 nm, following Refs. [10, 83, 88, 107].

Figure 5.7 shows the values of Q' as a function of φ and $\Delta_{KK'}$, up to the maximum of $\Delta_{KK'} = 0.12$ meV. The thick dash-dotted line marks where

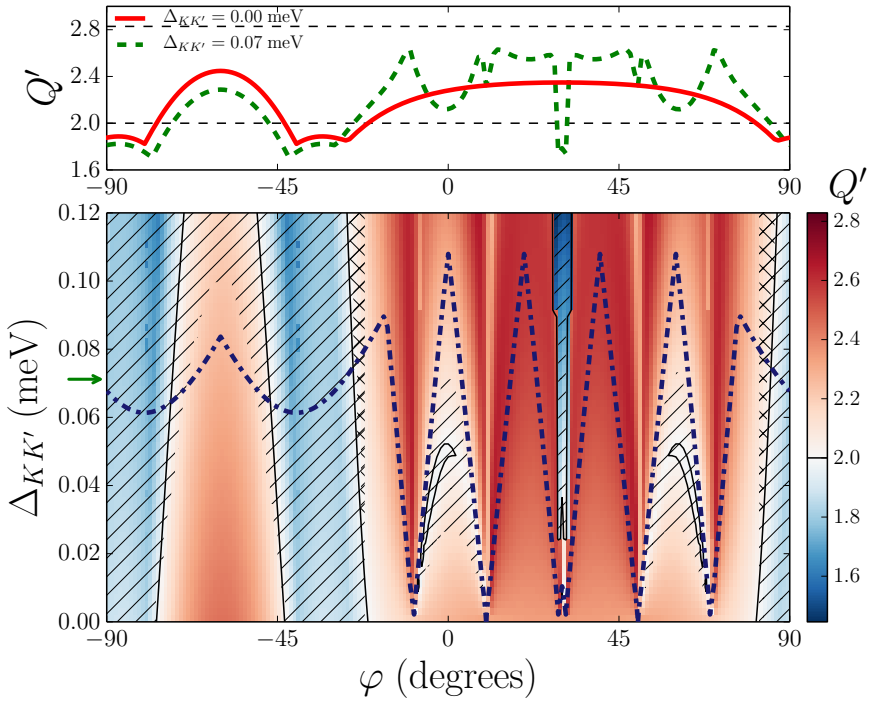

Figure 5.7: The bottom graph shows a density plot for Q' as a function of $\Delta_{KK'}$ (same for both quantum dots) and magnetic field angle φ for a (24,12) nanotube in a 1 T magnetic field, with quantum dot lengths of 450 nm. Assumed is a bending angle $\Delta\varphi_{\mathrm{SO}} = 30°$ between both quantum dot axes and a large bending radius, as in the experimental setup, such that the local spin axes defining $\mathbf{S}$ are adiabatically transformed when transporting a spin from the left to the right end of the nanotube, such that the spin correlators in Eq. (5.1) must be evaluated in the *local* coordinate systems of both quantum dots. The contour lines mark the boundary $Q' = 2$. In the unhatched areas $Q' > 2 + |\delta Q|$ such that entanglement detection based on Q' would be consistent with the ideal Q. In the diagonally hatched areas $Q' < 2 + |\delta Q|$ and no conclusion can be made. In the cross-hatched areas the ideal $Q \leq 2$ excludes entanglement detection, but $Q' > 2$ due to the valley mixing, which would lead to a false entanglement detection. The dash-dotted blue line marks $\min\{\delta_\tau, \tilde{\delta}_{\tilde{\tau}}\} = 1$, and the spin correlation reconstruction via Eq. (5.6) is valid only far below this dash-dotted line. In the top plot we display the ideal curve with $\Delta_{KK'} = 0$ (solid red line) and the curve with $\Delta_{KK'} = 0.07$ meV for both quantum dots (dashed green line), corresponding to horizontal cuts through the bottom plot at the minimum and at the position of the green arrow on the vertical axis. The range of $2 < Q < \sqrt{8}$ is framed by the dashed horizontal lines.

$\max_{\tau,\tau'}\{\delta_\tau, \delta'_{\tau'}\} = 1$, and we can expect that the entanglement detection remains valid sufficiently below this line. In the diagonally dashed regions $Q < 2 + |\delta Q|$ and entanglement detection is impossible, whereas in the undashed regions $Q > 2 + |\delta Q|$ provides a safe entanglement detection. The cross-hatching, however, marks regions, in which $Q' > 2$ but $Q < 2$, meaning that $|\delta Q|$ is large enough to provide an apparent but de facto inconclusive violation of the Bell inequality. The black contour lines mark the threshold value $Q' = 2$. This figure indicates that while for specific level configurations even weak valley mixing amplitudes of $\Delta_{KK'} \gtrsim 0.01$ meV have a sufficient influence to destroy the spin projections, the principal detectability of entanglement extends over a remarkably wide range of $\Delta_{KK'}$ values. This is illustrated in particular by the top part of Fig. 5.7, which shows the angular dependence of Q' for the ideal case with $\Delta_{KK'} = 0$ (solid red line) and with $\Delta_{KK'} = 0.07$ meV (dashed green line). Although Q' with large $\Delta_{KK'}$ shows strong jumps whenever two dot levels are coming close to each other, the overall trend and shape of the curve as a function of φ follows the ideal case Q.

As a second example we consider the effective model of Eq. (5.2) for a quantum dot, as used in Ref. [24], parametrizing the spin-orbit interaction strength by the energy $\Delta_{\mathrm{SO}} = g_s \mu_B B_{\mathrm{SO}}/2$ and $g_{\mathrm{orb}} \to \pm g_{\mathrm{orb}}$ depending if the quantum dot levels are electron or hole like. Figure 5.8 shows the results as in Fig. 5.7 within this model for the experimentally determined parameters for shells h and N of the two quantum dots, yet with varying (and identical) $\Delta_{KK'}$ for both dots. In contrast to the previous example, both quantum dots are substantially different. The influence of $\Delta_{KK'}$ is much more pronounced, leading to much wider regions of inconclusive or wrong entanglement detection, also well illustrated by the inset where the curve at $\Delta_{KK'} = 0.07$ meV (dashed line) has now only little in common with the result at $\Delta_{KK'} = 0$ (solid line).

A particular sensitivity to valley mixing is noted in Fig. 5.8 at angles $\varphi > 0$. While $Q' > 2$ for $\Delta_{KK'} = 0$ (solid red curve in upper panel), these Q' values drop below 2 almost instantaneously as soon as $\Delta_{KK'}$ becomes nonzero (observe in the lower panel the thin, bright, horizontal area (visible when zooming) close to $\Delta_{KK'} = 0$ at $\varphi > 0$, which is immediately replaced by the hatched blue regions when moving up on the vertical axis). This behavior reflects a strong sensitivity of the spin polarizations upon valley mixing, and the abrupt change in Q' is the result of the nonlinear normalizations in Eq. (5.6). Such a behavior is absent in Fig. 5.7 which thus represents a sample with more robust spin polarizations. We remark furthermore that Fig. 5.8 shows that a qualitatively unchanged behavior of Q' over a range of small to large values of $\Delta_{KK'}$ does not allow to conclude on the stability of the spin projections.

Yet improvement can be made even for this system, for instance, by en-

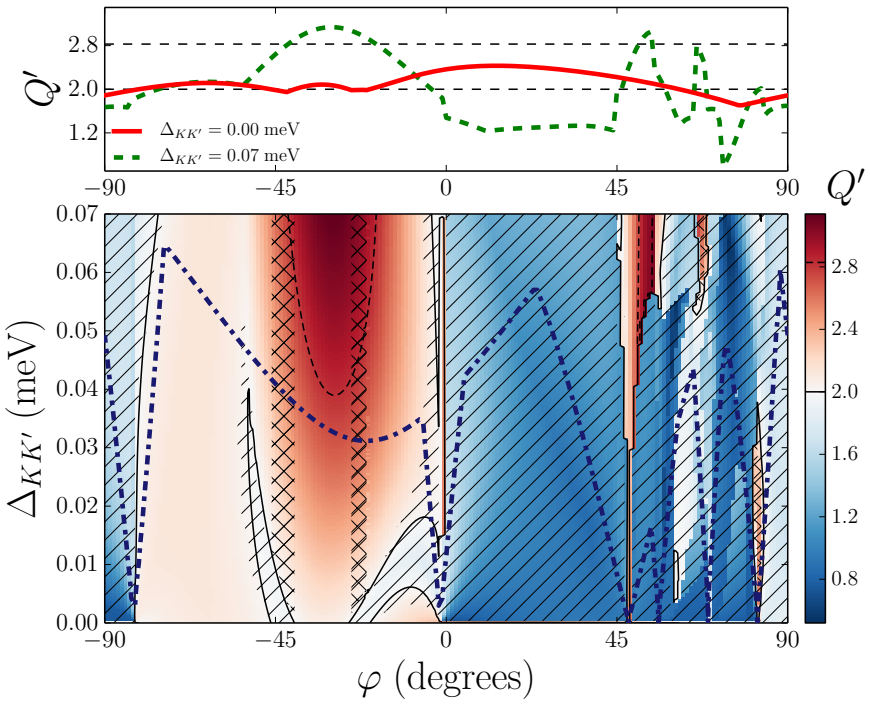

Figure 5.8: Same plots as for Fig. 5.7 based on the effective model, Eq. (5.2), for both quantum dots with the experimental parameters for shells h (hole type, $\Delta_{\mathrm{SO}} = g_s \mu_B B_{\mathrm{SO}}/2 = 0.05$ meV, $g_{\mathrm{orb}} = 5.2$, $g_s = 2$) and N (electron type, $\Delta_{\mathrm{SO}} = 0.15$ meV, $g_{\mathrm{orb}} = 2.6$, $g_s = 2$), subject to $B = 0.7$ T and the bending angle $\Delta\varphi_{\mathrm{SO}} = 21°$. The dashed contour lines show where Q' exceeds the nominal maximum $Q = 2\sqrt{2}$, giving a definite identification of the regions where the spin correlation reconstruction is entirely invalidated due to $\Delta_{KK'}$.

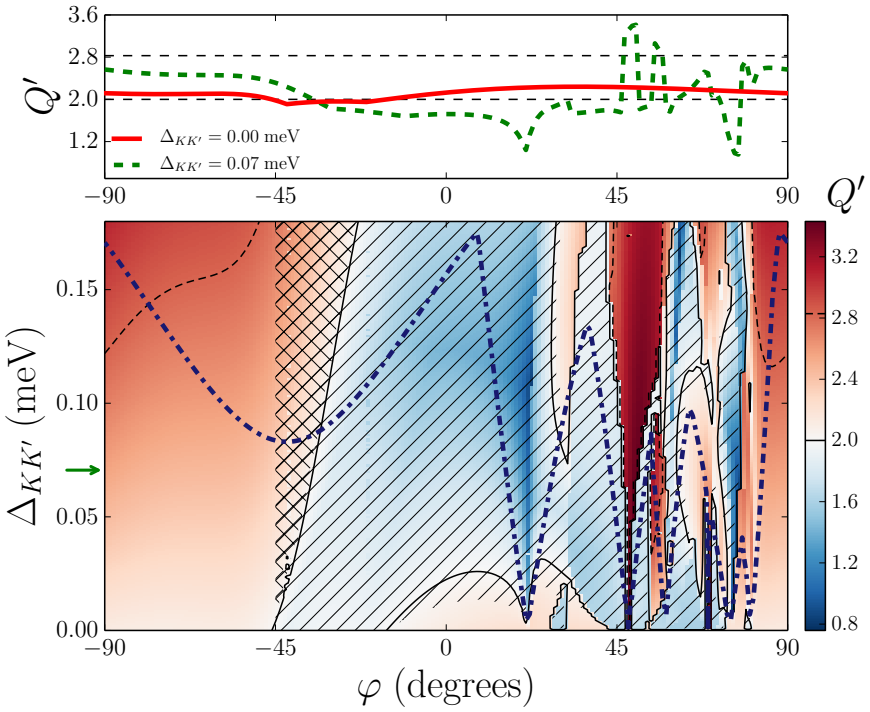

Figure 5.9: Repetition of the results of Fig. 5.8 for an increased magnetic field of $B = 2$ T and an enhanced range of $\Delta_{KK'}$. The top plot shows still the curves at $\Delta_{KK'} = 0$ and $\Delta_{KK'} = 0.07$ meV (corresponding to a horizontal cut at the green arrow on the $\Delta_{KK'}$ axis in the bottom plot).

hancing the stability of the spin polarizations by increasing the magnetic field (assuming that the critical field for the superconductor could be increased accordingly). Figure 5.9 shows the same situation as Fig. 5.8 for the larger field $B = 2$ T. While still far from ideal, the improvement of the situation for entanglement detection is quite notable.

These results show that with the flexibility of the free choice of φ there are ranges of the direction of the magnetic field, in which Q' follows quite closely the ideal values of Q even for values of $\Delta_{KK'}$ that can become even as large as the 0.07 meV of shell N. From the data these angular ranges are characterized by a smooth behavior of Q' without the discontinuous jumps arising from approaching and crossing energy levels, for which the strict requirement $\Delta_{KK'} \ll \min_{\tau,s,s'}\{|E_{\tau,s} - E_{-\tau,s'}|\}$ can be weakened to $\Delta_{KK'}$ approaching this upper limit.

Superconducting gap in excitation spectroscopy data

In Fig. 5.10 excitation spectroscopy of filling $n_e + 2$ of the h shell in the left segment is shown. In addition to the excitation lines at larger bias the closing of the superconducting gap of $\Delta_{\mathrm{SC}} \approx 60$ μeV is also visible at zero bias and $B_{\parallel^*} \lesssim 0.8$ T. The superconducting gap changes the excitation spectrum by shifting up the excitations in energy by Δ_{SC}. This is, however, too small an energy scale to be noticeable in plots such as Fig. 3 (a)-(c) in the main text due to low-energy excitations in those plots. Similarly, the inclusion of the superconducting gap in the nanotube model does not change the extracted parameters, since the fit is dominated by data above B_{C}. Cuts along V_{SD} in Fig. 2 (b),(d) in the main text show that the gap is "soft"[46].

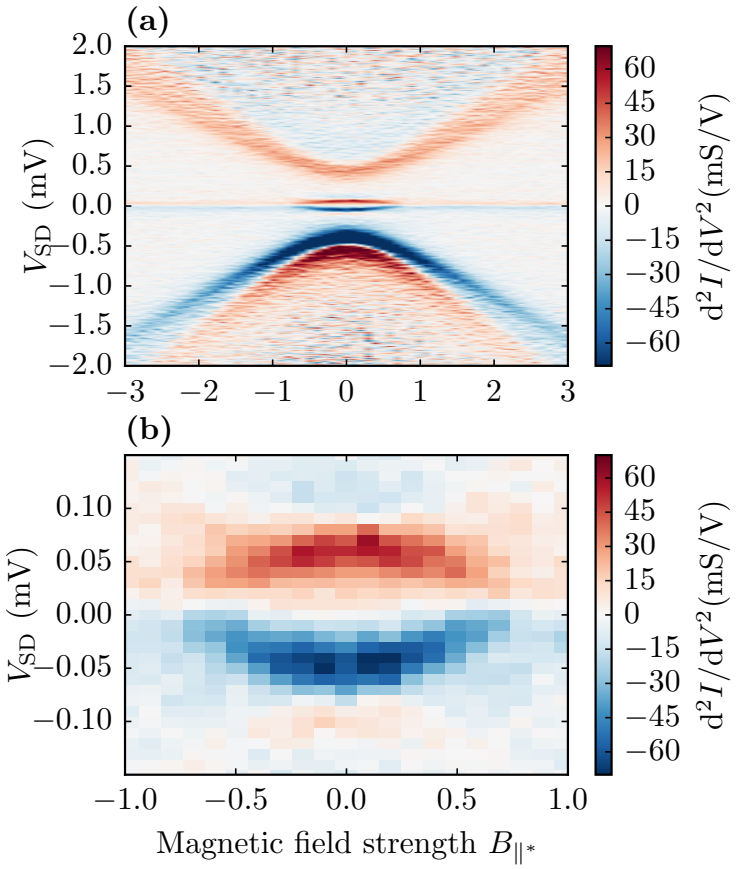

Figure 5.10: **(a)** Excitation spectroscopy of the $n_e + 2$ filling in shell h. The first excitation is seen to be at significantly higher energy than the superconducting gap at ≈ 60 μeV. **(b)** Zoom of region at low magnetic field and low bias showing the closing of the superconducting gap in more detail.

Chapter 6

Nonlocal signals in a carbon nanotube Cooper pair splitter

The results in the Chapter 5 showed that even in the presence of KK'-scattering it is still possible to detect entanglement by modifying the original scheme by Braunecker et al. [10]. Thus encouraged we move forward in this chapter with an entanglement detection experiment on the CNT CPS device from the previous chapter. In practical terms this procedure involves

1. Identifying a set of nonlocal conductance signals ΔG between at least one shell in each dot. The signals must be positive even after subtracting the classical negative resistive crosstalk signal.

2. Calculating the Q-value from equation eq. (2.54) and asserting that it violates (5.8) where disorder has been taken into account.

Please refer to figures 2.12 and 5.1 for schematics of the device.

Relative to last chapter we shift our focus to shells h, g, f, e, d, c and b in the left dot and shells w, v, u, t, s in the right dot. The backgate voltage is now fixed at $V_{\mathrm{BG}} = -10.5\,\mathrm{V}$ compared to $V_{\mathrm{BG}} \approx 5\,\mathrm{V}$ in the last chapter. These voltages are on either side of the band gap which means that we are now dealing with holes in both dots. Also note that we will use dot 1 (dot 2) interchangeably with "left" ("right") dot according to the context.

Figure 6.1 shows bias spectroscopy data of the region of interest (subfigures a and c) as well as low-bias zooms revealing the superconducting gap and subgap states (subfigures b and d). The shape of the subgap states in dot i depends on the relative magnitudes of Δ, charging energy U_i and dot-superconductor coupling Γ_{Si} [110]. Charging energy and level spacing are larger than all other parameters in both dots at 4 meV to 8 meV. The fact that the subgap excitations approach $V_{\mathrm{SD}} = 0$ in Figure 6.1(b) indicates that Γ_{S1} is comparable to or larger than $\Delta \approx 60\,\mu\mathrm{eV}$. Conversely, in dot 2 in Figure 6.1(d) the subgap excitations are everywhere pushed out to the gap at Δ reflecting a high energy for the singlet [110] and consequently a low

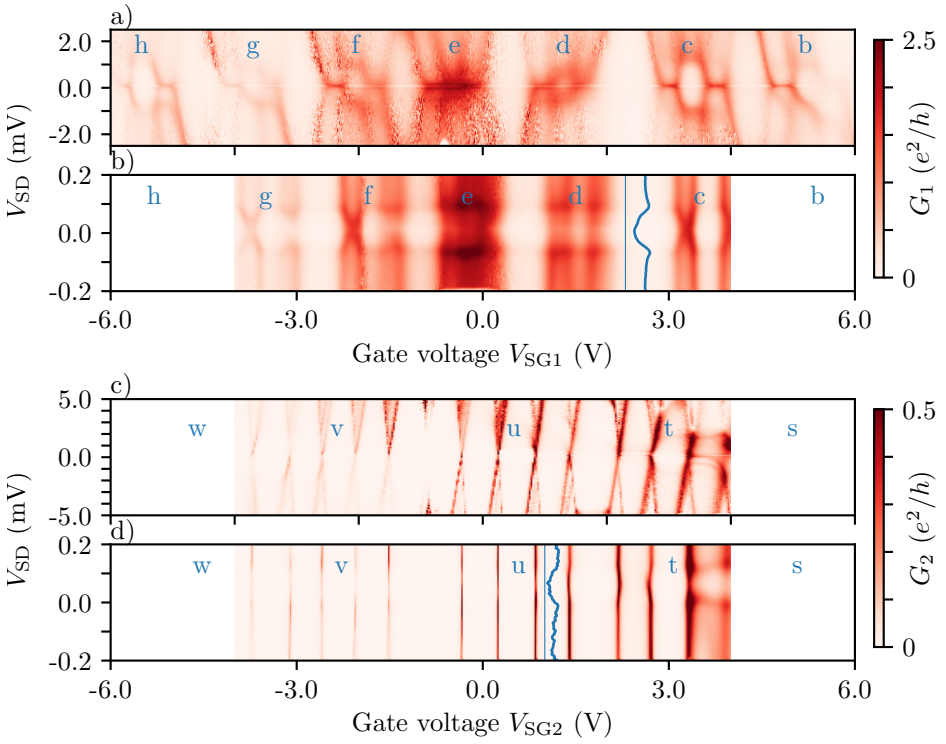

Figure 6.1: a), c) High bias data showing the shell structure in dot 1 and 2. Shells h, g, f, d, c and b show zero-bias SU(2) Kondo resonances whereas shell e has an SU(4) Kondo resonance. The coupling is weaker in dot 2 than in dot 1 and consequently dot 2 is Coulomb blockaded between all resonances. b), d) Zoom around the superconducting gap in dot 1 and 2. Line cuts in blue show the superconducting gap more clearly. The structure of the subgap states in dot 1 indicates that $\Gamma_{S1} \gtrsim \Delta$. In dot 2 the subgap excitations are pushed out to Δ which indicates a weak $\Gamma_{S2} \ll \Delta$. Note the vertical offset in voltage of 70 µeV in dot 2 visible in the t shell and in the blue line cut. Truncated versions of a) and b) are also shown in Chapter 5.

value for Γ_{S2}, such that $\Gamma_{S2} \ll \Delta$. Since the excitations are narrow and the maximum conductance is close to $1e^2/h$ we take Γ_{N2} to be comparable to Γ_{S2} by the standard Breit-Wigner shape of Coulomb resonances (see section 2.2.2). Conversely, for device 1 the asymmetry in conductance at positive and negative bias in, e.g., shells g and b indicates that one coupling is much smaller than the other. In this case $\Gamma_{N1}/\Gamma_{S1} \ll 1$ except for shell d where the coupling strengths are opposite $\Gamma_{N1}/\Gamma_{S1} \gg 1$. The thermal energy is negligible at the experiment temperature of about 25 mK: $k_B T \approx 2.5\,\mu\text{eV}$. The AC excitation $|eV_{SD}| = 6\,\mu\text{eV}$ is smaller than all other parameters except $k_B T$.

In summary we are in the parameter regime

$$U_i, \Delta E_i \gg \Gamma_{S1} \gtrsim \Delta \gg \Gamma_{S2}, \Gamma_{N1}, \Gamma_{N2}, k_B T \quad \text{and} \quad |eV_{SD}| > k_B T \tag{6.1}$$

except for shell d which has $\Gamma_{N1}/\Gamma_{S1} \gg 1$.

If we compare these parameter values with the those found to maximize the I_{CPS}/I_{EC} in the analysis of Recher et al. ([49] and section 2.3.2) we see that our device is not ideally suited for Cooper pair splitting. Being in the wrong parameter regime does not exclude transport by Cooper pair splitting, but we should expect a lower I_{CPS}/I_{EC} ratio as well as lower efficiency ϵ and visibility η.

Now, to measure a nonlocal signal we must sweep the chemical potential of the dots independently. In order to do this we define linear combinations of side gates to cancel the cross capacitance. These "mix" gates are defined by

$$\begin{pmatrix} V_{SG1} \\ V_{SG2} \end{pmatrix} = \begin{pmatrix} 1.000 & -0.100 \\ -0.102 & 1.000 \end{pmatrix} \begin{pmatrix} V_{MG1} \\ V_{MG2} \end{pmatrix}. \tag{6.2}$$

Figure 6.2 shows the stability diagram of a subset of the region in Figure 6.1. Specifically, Figure 6.2 comprises all states in dot 1 in Figure 6.1(a), but only the states in dot 2 which are below $V_{SG2} = 0$. The off-diagonal coefficients in the definition of the mix gates (6.2) are sufficiently small that we can use mix and side gates interchangeably when comparing the two figures. Note that both plots in Figure 6.2 consist of two separate sweeps. This is visible as a slight vertical discontinuity in Figure 6.2(a) at $V_{MG2} = -3.2\,\mathrm{V}$ and blank areas in the top left and bottom right corners in both plots. These sweeps were taken using the mix gates by fixing the value of V_{MG1} and sweeping the full ranges of V_{MG2} (that is, V_{MG2} is swept from $\approx -6\,\mathrm{V}$ to $\approx -3.2\,\mathrm{V}$ in the left sweep and from ≈ -3.2 to $\approx -1\,\mathrm{V}$ in the right).

We wish to identify the nonlocal signals ΔG_i in Figure 6.2, which are expected to have maximum amplitude at the crossing between resonances in the two dots [49]. Evidently, no nonlocal signals are immediately visible in Figure 6.2. To enhance the visibility we subtract for each vertical column (horizontal row) in the left (right) plot the background using the new algorithm described in section C.2. By doing this we obtain the nonlocal signal

$$\Delta G_i = G_i - G_{0,i} \tag{6.3}$$

where G_0 is the baseline signal which is assumed to contain no CPS processes. We emphasize that the procedure of C.2 takes a 1D data trace as input. Thus, the constituent 1D traces in the plots are treated separately and no correlation between 1D traces is used, whether the 1D traces are adjacent in the data or not. Also, since the plots in Figure 6.2 consist of two separate sweeps each, the procedure is applied to the sweeps separately to avoid any artifacts that may arise from the discontinuity at $V_{MG2} \approx -3.2\,\mathrm{V}$.

The background subtraction procedure only gives a meaningful result for G_1 due to the way the sweep is performed (sweeping V_{MG2} and stepping

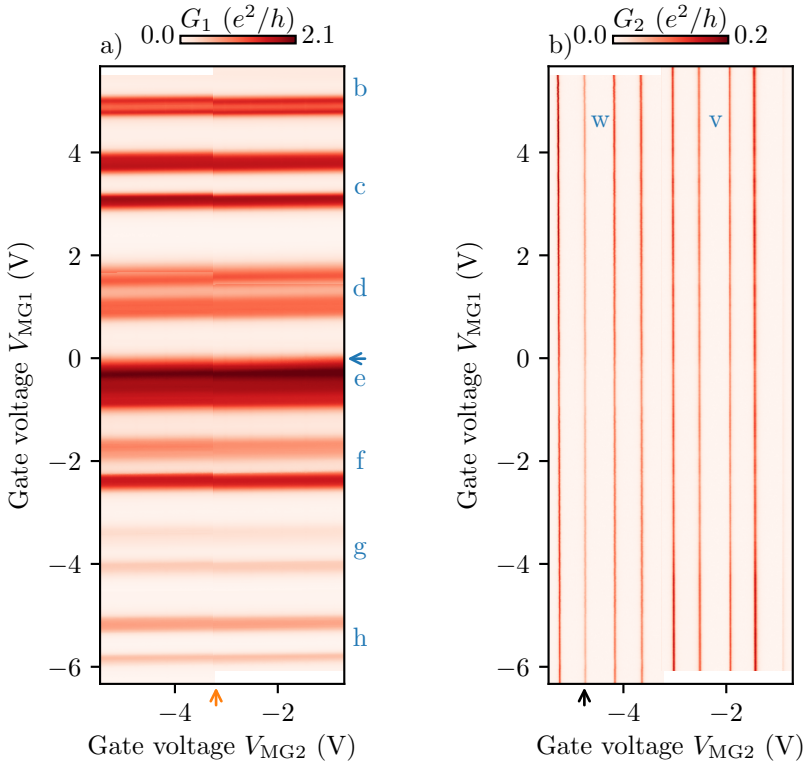

Figure 6.2: Stability diagram of a) dot 1 and b) dot 2 measured using mix gates which correct for cross capacitance. Letters denote naming of shells. The magnitude of the nonlocal signal is too small to be immediately visible. Note that both subplots consist of two sweeps each, which is the reason for the blank space in the corners and the vertical discontinuity at $V_{MG2} \approx -3.2\,\mathrm{V}$ (orange arrow).

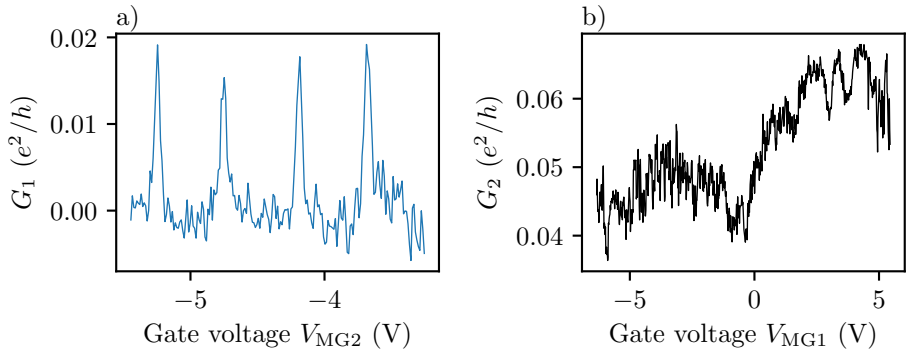

Figure 6.3: Line cuts at the positions of the arrows in Figure 6.2 which illustrate the difficulties in baseline subtraction. a) Line cut in dot 1, b) line cut in dot 2. The conductance in dot 1 is well-behaved and the baseline is well-defined. Drift and noise cause the baseline in the dot 2 line cut to be poorly defined. Note that a) only extends half the V_{MG2} range of Figure 6.2.

V_{MG1}). To illustrate the problem Figure 6.3 shows line cuts at the arrows in Figure 6.2. Conductance in dot 1 along the blue arrow is shown in Figure 6.3(a). Four peaks are clearly visible along with the baseline despite noise. The conductance in dot 2 in Figure 6.3(b) shows a more noisy, drifting behavior. This is caused in part by the fact that the time between adjacent G_2 data points is equivalent to the time it takes to do the whole trace in Figure 6.3(a). Thus, drift over time has a marked negative effect on G_2 leading to an ill-defined baseline.

With the above reservations regarding background subtraction in mind the dot 1 nonlocal signal ΔG_1 is shown in Figure 6.4 along with the corresponding visibility $\eta_1 = \Delta G_1/G_1$. The horizontal noisy bands in Figure 6.4 coincide with the horizontal resonances in Figure 6.2 where the higher current causes an increased shot noise. We observe that the positive nonlocal signals appear both on resonances, slopes of resonances, and in valleys. Negative nonlocal signals only appear on resonances. The nonlocal signals do not depend on resonance detuning in the way predicted by eq. (20) in [49] which predicts maximum amplitude for the nonlocal signal at zero detuning. This may be explained by the fact that our device is not in the ideal CPS regime as discussed above. Also, we predict the softness of the gap in the our device (see line cuts in Figure 5.2) to diminish the Cooper pair splitting process relative to other transport processes.

We obtain a local visibility η_1 no higher than 6 % which is comparable to some results in the literature: Hofstetter et al.: 0-12% [13], Fülöp: 3.7% [111], Fülöp et al.: 2.8%-28.7% [15], Schindele et al.: 0-12% [112], Herrmann et al.: 35-55% 0-100% [11], Schindele et al.: 75%-98% [12]. Das et al.: 70%-100% [14].

We can calculate the classical negative crosstalk using $\delta G_1 \approx -\delta G_2 R_W G_1$ [13]. Here, δG_1 is the change in dot 1 conductance as a resonance enters the

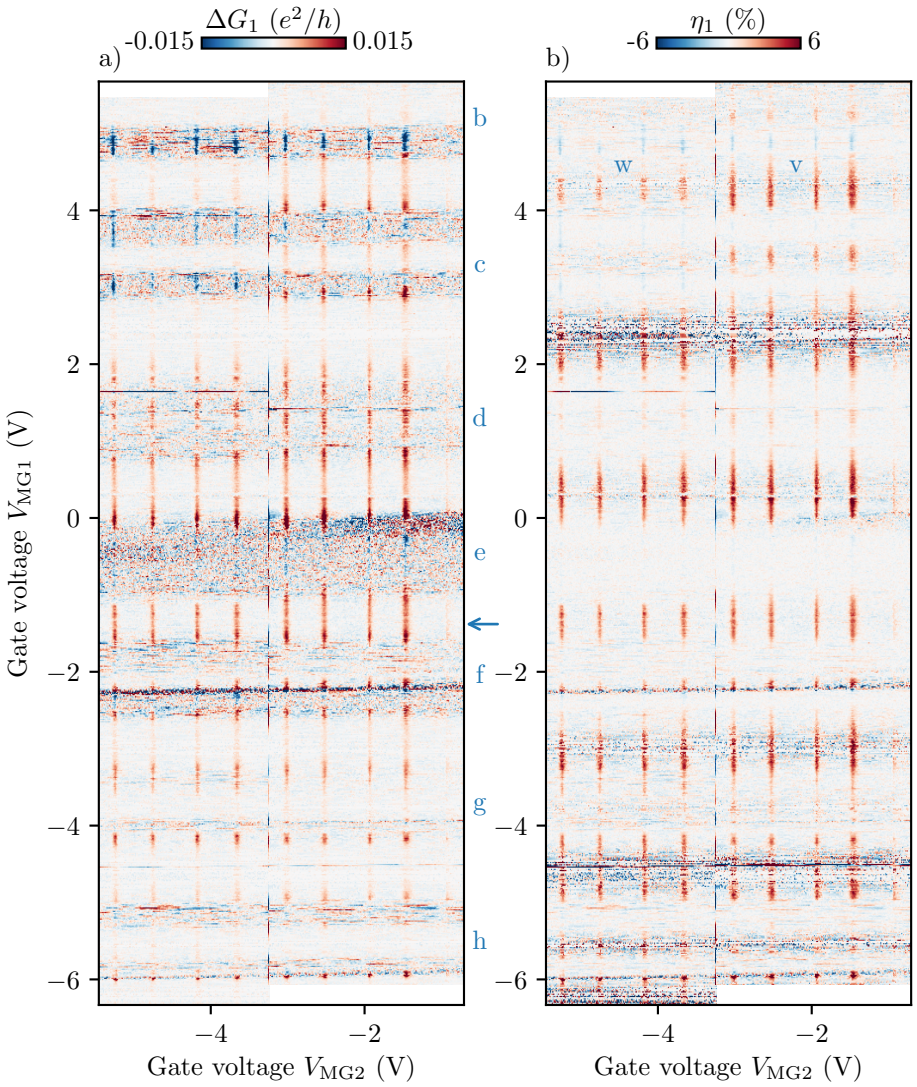

Figure 6.4: a) Nonlocal signal ΔG_1 in dot 1. b) Visibility η_1 in dot 1. The horizontal noisy bands coincide with horizontal resonances in Figure 6.2(a). No obvious variation in ΔG_1 can be deduced within shells, although variation between shells can be seen at, e.g., $V_{MG1} = 3\,\mathrm{V}$.

bias window in dot 2 with a consequent increase in conductance δG_2. The expression is valid as long as the wire series resistance R_{W} is much smaller than $1/G_1$ which is valid in our device which has $R_W \approx 130\,\Omega$ and $1/G_1 \sim h/e^2 \approx 25\,\mathrm{k}\Omega$. From Figure 6.2 we get $\delta G_2 \lesssim 0.2e^2/h$ and $G_1 \lesssim 2.1e^2/h$ so that δG_1 becomes $\lesssim 0.002e^2/h$. This is small enough that we can safely neglect it in analyzing the experimentally obtained ΔG_1 in Figure 6.4.

Of particular interest for the entanglement detection experiment [10] is whether ΔG_1 shows any variation depending on the specific combination of resonances within a shell. The only clear difference is observed at $V_{\mathrm{MG1}} = 3\,\mathrm{V}$ where the four left-most (right-most) resonances show negative (positive) values for ΔG_1. These eight resonances belong to two distinct shells (w and v), however, and no variation is visible within the shells. Unfortunately, we do not have data on shell w, but we can speculate that its lead couplings are different from shell v, which leads to a different ΔG_1. Rather than this coupling-induced change in ΔG_1 we are interested in changes in ΔG_1 caused by the quantum mechanical character of the carbon nanotube states.

Despite sincere efforts it has not been possible for this author to identify consistent patterns in the magnitude or sign in ΔG_1. Possible hypotheses for ΔG_1-dependence such as, e.g., sign of detuning and strength of coupling (including SU(2) vs SU(4) Kondo effect) do not hold across all resonances. Analysis is also impeded by the fact that the effective bias is only known with a substantial margin of error. This will be discussed at the end of the chapter.

To establish that the nonlocal signals we observe are, indeed, a superconducting effects we sweep V_{MG2} in Figure 6.5 at the position of the blue arrow in Figure 6.4 and increase the magnetic field to quench the superconductor. The nonlocal signal vanishes between $B \approx 0.2$ and 0.3 T, well before the in-plane critical field of $\approx 0.7\,\mathrm{T}$ where the superconducting gap goes to zero. The values of ΔG_1 of the four resonances do not decrease monotonically, however. The ΔG_1-value in the top resonance appears to increase, not decrease, until $B \approx 0.2$ T for instance. This could be an expression of the spin-filter effect we are looking for in the entanglement detection experiment. Without knowing the parameter regime of the shells in question it is hard to say anything quantitative about this observation, though. In the following we will attempt a speculative explanation:

The chemical potential in dot 1 is fixed at $V_{\mathrm{MG1}} = -1\,\mathrm{V}$ between shell f (no holes) and shell e (4 holes). The four relevant resonances in dot 2 belong to shell v which we assume to have $\Delta_{KK'} > \Delta_{\mathrm{SO}}$ as this is usually the case. Suppose $B_{\mathrm{SO}} \ll 0.1\,\mathrm{T}$ in both dots. In this case the spins in both dots will be fully polarized along $\mathbf{B}$ for $B \gtrsim 0.1\,\mathrm{T}$ with one spin-up-spin-down pair increasing in energy and one pair decreasing in energy (see Figure 21(c) in Laird et al. [24]). Suppose further, that only a single level with a fixed spin in dot 1 participates in the CPS process. Then the amplitude for the CPS

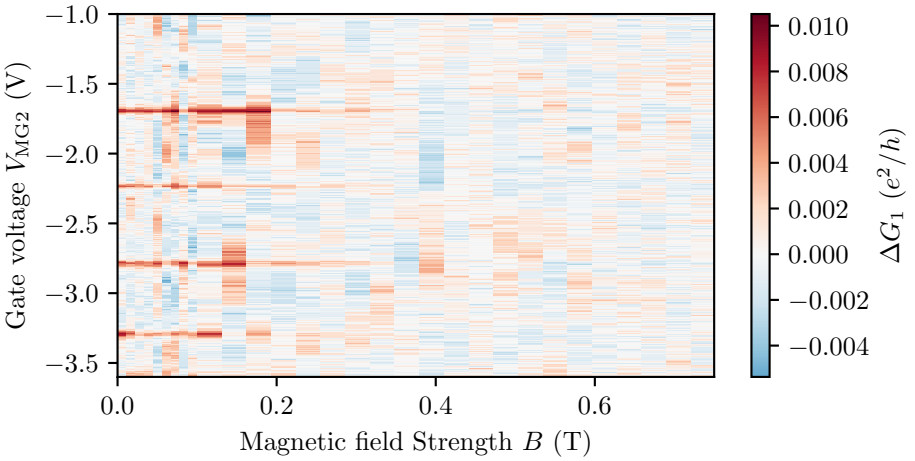

Figure 6.5: Evolution of the nonlocal signal ΔG_1 as a function of magnetic field strength. The magnetic field is oriented parallel to the tube axis to within 10°. The critical field of the aluminium film for this orientation of the field is ≈ 0.7 T. The plot consists of two merged sweeps which explains why the resolution for $B < 0.1$ T is higher.

process will depend on the overlap between the level in dot 1 and a given level in dot 2 where the spin alternates between up and down. For instance, if dot 1 holds a spin-up electron, then the CPS process has larger amplitude for a spin-down in dot 2 because of the singlet nature of the Cooper pair. The polarization of the spins explains why the top and third ΔG-values and the second and bottom ΔG-values are similar. A disorder-dominated shell $\Delta_{KK'} > \Delta_{\mathrm{SO}}$ ensures that levels with opposite spins do not cross with increasing B which serves to explain why the pattern just described is the same for all B-values. We emphasize that this is a speculative, albeit realistic, explanation.

Given the small magnitude of the superconducting gap $\Delta \approx 60\,\mu$eV in our device it is important to be able to control V_{SD} precisely since the Cooper pair splitting current is sensitive to the ratio $|eV_{\mathrm{SD}}|/\Delta$ [57]. The current amplifiers employed in the measurements (Ithaco DL1211, see section 3.2) unfortunately do not support automatically regulating the offset voltage at the input connector at the microvolt level. Also, this voltage offset was suspected to drift on the order of tens of microvolts. To gauge this drift the offset was measured periodically by performing bias spectroscopy in later, equivalent measurements on a nanowire CPS device and identifying the V_{SD} zero-point. A series of such measurements is shown in Figure 6.6. The offset shows 24 hour periodic oscillations with maxima at 4PM and minima at 4AM which is consistent with the warmest and coldest times of day in Copenhagen in July. Although the data in this chapter was taken in December-January and the laboratory is air conditioned we should still expect the bias to oscillate on the time scale of 24 hours given the measurement in Figure 6.6.

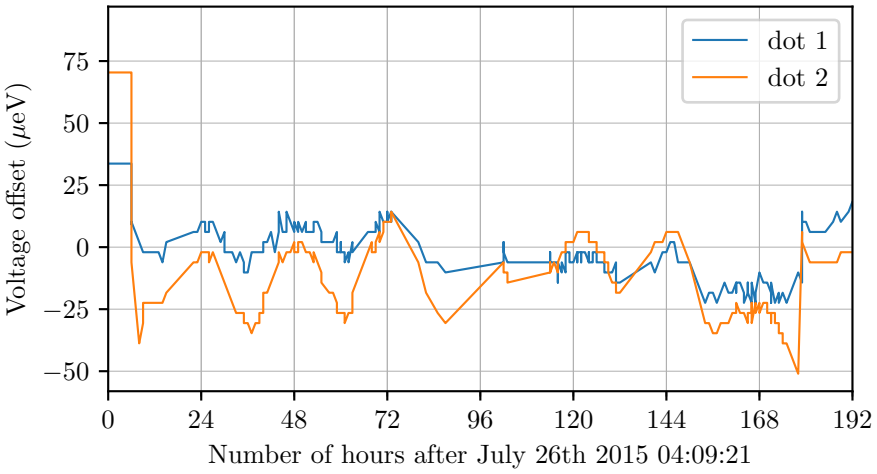

Figure 6.6: Evolution over time of current amplifier voltage offsets in dot 1 (blue) and dot 2 (orange) obtained from bias spectroscopy data. The offsets are seen to oscillate with a 24-hour period. The minima and maxima of the oscillations are consistent with those of temperature. Straight lines are due to the fact that points are not equidistant on the x-axis. The current amplifiers were calibrated manually near the start of the measurement where the offsets drop from $> 25\,\mu\text{eV}$ to smaller values. Note that this measurement is not conducted on the CNT CPS device discussed in this chapter. The measurement setup is equivalent so the offset results should be transferable.

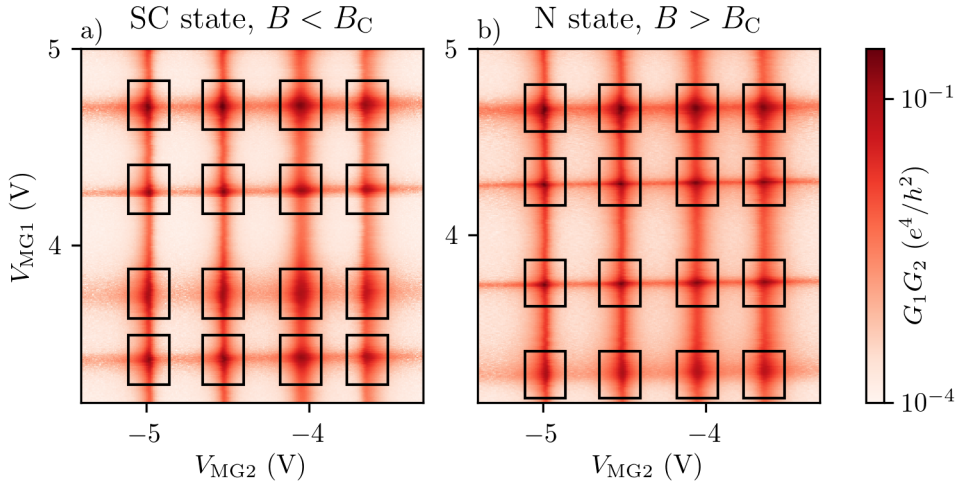

Figure 6.7: Stability diagram for calculating Q for a) superconducting state and b) normal state. The magnetic field B is used to drive the superconductor normal. The black rectangles show the region where the conductance product G_1G_2 is numerically integrated to obtain $G_{\nu a_\tau,\nu' b_{\tau'}}$ in eq. (2.55).

Thus, the CPS measurements are done, effectively, at a finite, unknown bias with oscillations on the order of Δ. This seriously impedes analysis of the measurements. To address this issue subsequent measurements employed SP 983 current amplifiers [113] which have adjustable input voltage [1].

Finally, in a separate cooldown of the CNT CPS device we sought to establish a baseline for Q by measuring a combination of resonances which ought *not* to demonstrate entanglement. The measurement is shown in Figure 6.7. Note that the plot shows the conductance product, not conductance for the separate dots. The black rectangles show the region where the conductance product G_1G_2 is numerically integrated to obtain $G_{\nu a_\tau,\nu' b_{\tau'}}$ in eq. (2.55). In this particular region of chemical potential we have no information about the spin and valley character of the states which is necessary to calculate Q. Therefore, we calculate Q for all $(4!)^2 = 576$ possible combinations of spin and valley index to get an upper bound on Q. We use eq. (2.54) to get for the superconducting and normal state, respectively

$$Q_{\mathrm{SC}} \leq 0.16, \qquad Q_{\mathrm{N}} \leq 0.1. \tag{6.4}$$

These values are comforting to use as baseline values because they indicate that no amount of data wrangling can produce a high Q-value if the physical effect is not present. As such, a small Q-value of even 0.5 would be strong indication of a non-trivial effect. We find that the values in (6.4) are robust against small changes in the boundary of the black boxes since the conductance product is strongly suppressed away from resonance by either one or

[1] Both the LSK389A and IF3602 models were used and both consistently achieved stable input voltage control at the $\pm 10\,\mu$V level or better.

the other dot being in Coulomb blockade.

Note that it is not possible to do this calculation for the data in Figure 6.2 because all resonances in dot 1 are SU(2) or SU(4) Kondo resonances which are outside the scope of the Braunecker proposal.

In closing we sum up the results of the carbon nanotube Cooper pair splitter device investigated in this chapter and Chapter 5. The device satisfies many of the requirements for the entanglement detection experiment. Specifically, it shows a superconducting gap, a critical magnetic field comparable to the appreciable spin-orbit magnetic field in the nanotube, shell structure, low disorder (in dot 2), a non-zero angle between the nanotube segments, and evidence of Cooper pair splitting transport processes.

When the entanglement detection experiment and analysis are carried out we find that the value of the Q parameter does not indicate entanglement which is to be expected given the couplings between nanotube and leads. The fact that $Q < 0.16$ for several hundred combinations of spin and valley state assignments is evidence that Q is a robust parameter and that a finding of $Q > 2$ would be trustworthy evidence for transport of entangled Cooper pairs.

Despite sincere efforts this project has not succeeded in fabricating additional samples with nanotube-lead couplings better suited for the entanglement detection experiment. Compared to the requirement of non-collinear spin-orbit fields combined with low disorder, better-suited couplings ought to be straightforward to achieve judging by the range of couplings observed in the literature [114, 91, 115, 81]. Thus, the present device serves as a proof-of-concept that a CNT CPS device capable of demonstrating entanglement is well within reach for a lab with a working CNT device process.

Chapter 7

Tuning of Couplings in an InAs nanowire device

In chapters 5 and 6 we saw that carbon nanotube devices with exotic properties can be fabricated used conventional techniques without the use of "ultra-clean" schemes [1]. The performance of the device in question was, however, limited by the fact that the couplings Γ_i between quantum dot and electrodes were inappropriate for the planned experiments. Compared to the exotic nanotube properties the Γ_i couplings depend on simple electrostatics and should, in principle, be straightforward to control. In this chapter we address the shortcomings of the device in chapters 5 and 6 by showing results from an InAs nanowire (NW) CPS device with 15 bottom gates. The Γ_i's in the device are shown to depend exponentially on the voltage applied to the gates which is the behavior predicted by basic quantum theory [116].

Figure 7.1 shows the geometry of the device internally known as "N3B". Arrays of 15 bottom gates with a pitch of 50 nm are covered with 24 nm layers of HfO_2. InAs NWs are deposited randomly on the chip and electrodes are defined on the nanowires which are located on top of bottom gate arrays. The device was fabricated by Anders Jellinggaard and the measurements presented in the following were done by the author. For more details on fabrication we refer to [110, 117].

The device was measured using the setup detailed in Section 3.2 with additional lock-in amplifiers for measuring the voltage drops over two dots in the device. Conductances in this chapter are thus calculated four-terminally. The device was meant for Cooper pair splitting experiments so efforts were spent initially to tune it into the ideal regime identified by Recher et al. in reference [49]. Here, we focus on the tuning of the dot-lead coupling to complement chapters 5 and 6. In the following we will use the terminology "plunger" for gates which (primarily) control electrochemical potential in a dot and "cutter" for gates which (primarily) control lead-dot coupling. Note that a plunger (cutter) gate may also affect dot-lead coupling (electrochemical potential) due to cross-capacitance.

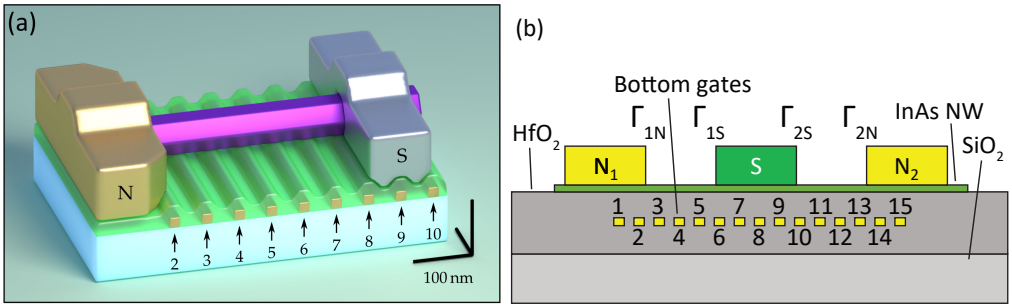

Figure 7.1: (a) Artist's representation of the left half of the InAs NW device. The purple NW is contacted by gold (N) and aluminium (S) electrodes. All three rest on a layer of HfO_2 (green) which covers 15 bottom gates (only 10 shown here). (b) Side view schematic of InAs NW device. Dot-electrode couplings Γ_i are specified on the figure. Note that the schematic is *not* to scale. Both are adapted from [110, 117].

With all bottom gates at 0 V the device is usually "open" with a constant conductance of order e^2/h when any single gate is varied. The tuning procedure then typically proceeds as

1. Decrease the voltage simultaneously on all gates until pinch-off is achieved. In some devices this pinch-off voltage is rather high (that is, it is large and *negative*). Such high voltages often cause the device to exhibit "switches" (see glossary) which impede consistent measurements.

2. Tune the plunger gate relative to the cutter gates to define a quantum dot with reproducible gate traces.

3. The cutter gate voltages are now varied one at a time. At each value of the cutter gate the plunger gate is swept and Γ's are extracted by fitting Coulomb peaks to eq. (2.38). Note that Γ_1 and Γ_2 (we use 1 (2) for L (R) in this chapter) enter symmetrically in eq. (2.38) which means that it is not possible *a priori* to know which lead a given Γ-value belongs to.

Figure 7.2 shows Coulomb peaks in dot 2. The height and width of the peaks are seen to change with increasing V_{g11} which is consistent with our expectation that V_{g11} should tune Γ_{2S}. A conductance trace and the corresponding fit are shown in the zoomed conductance trace.

Repeating the fit in Figure 7.2 for multiple values of V_{g11} and for gates 2, 6 and 14 yields the results in Figure 7.3. In this figure Γ_ν and $\Gamma_{\nu'}$ are distinguished by the output order of the fitting algorithm. Post-fitting analysis ascribes ν and ν' to lead N or S. Different colors correspond to different peaks, although the peaks are in general different between plots (for instance, the Coulomb peaks in dot 1 do not exist in dot 2). Note that the data in

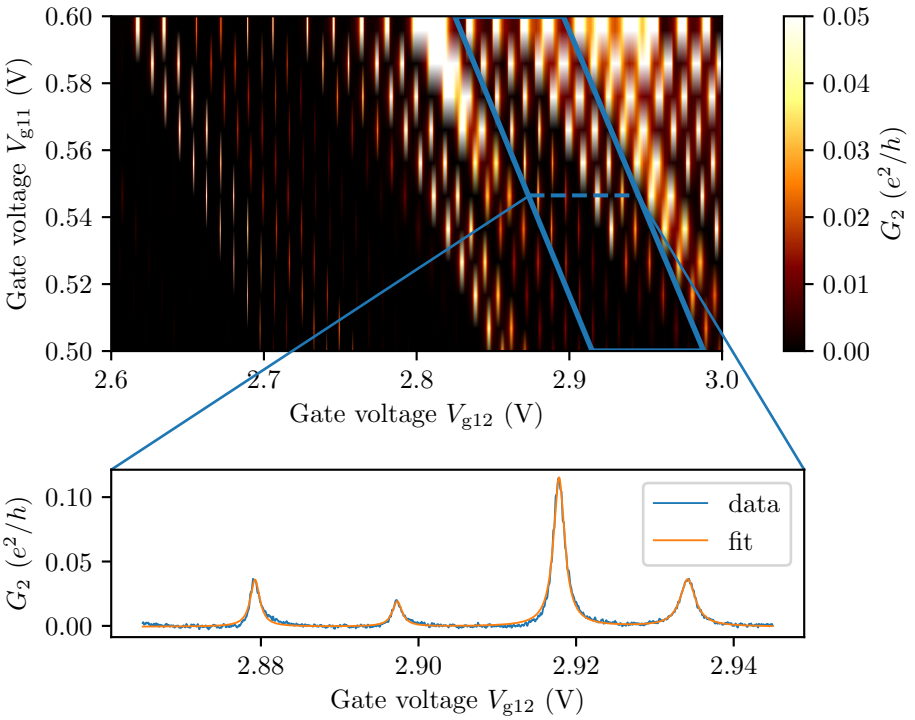

Figure 7.2: Example of coupling extraction. Conductance in dot 2 as a function of cutter gate V_{g11} and plunger gate V_{g11}. Coulomb peaks are seen in the horizontal direction. The peaks change appearance when changing V_{g11} since gate 11 tunes Γ_{2S}. The peaks in the blue parallelogram are analyzed further below. Conductance data as well as the corresponding fit to four instances of eq. 2.38 are shown in the zoom-in. This trace yields two couplings per peak, or eight couplings in total. The data is taken with the Al electrode in the superconducting state. The coupling to the SC electrode is found to be small enough that eq. 2.38 provides a good description of the peaks, even though the peaks are technically resonances of subgap states.

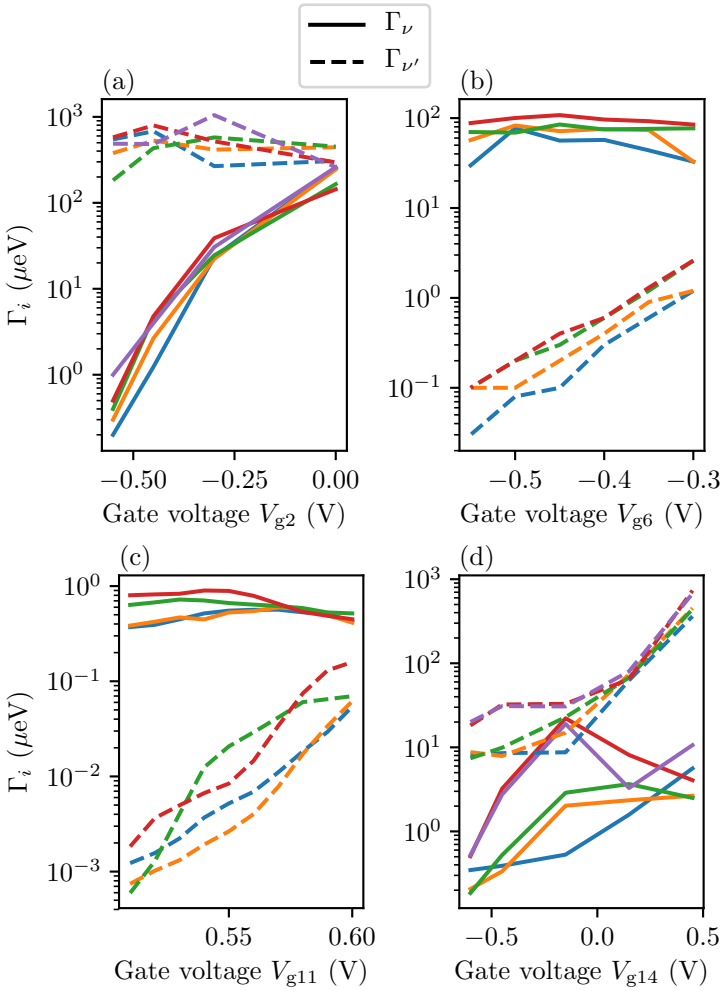

Figure 7.3: Couplings Γ as a function of gate voltage. In each plot a number of peaks have been fitted and the corresponding couplings (two per peak) are shown as lines. Peaks with same color within a plot belong to the same peak. Fitting peaks to eq. (2.38) outputs two unspecified couplings. It is straightforward to identify which lead a coupling belongs to from its evolution with gate voltage, but here we conservatively distinguish them with subscripts ν and ν'. In (d) one set of couplings is tuned to increase beyond the other. Although this looks messy it is consistent with the tuning in the other plots. See main text for analysis. Note that $\Gamma_{\nu'}$ is tuned across two orders of magnitude with a modest change in V_{g11} in (c).

Figure 7.2(c) is taken in the SC state. Comparing the SC and N state for other data shows that the difference is negligible for these Γ_{2S} values.

In Figure 7.3(a)-(c) we see clearly that one set of Γ's (either solid or dashed lines) depends exponentially on the gate voltage and that the other is roughly constant. At a glance Figure 7.3(d) appears to break this trend. The slope of the leftmost three data points indicates, however, that the gammas actually cross around $-0.1\,\mathrm{V}$. Switching dashes and solid lines for the two rightmost data points means that we again have one set of lines which depends exponentially on V_{g14} and one set which is roughly constant. The trend is not as clear for the blue lines, though. We note that this tuning is not efficient for every single peak in the device as demonstrated by the different ranges on the x-axes in Figure 7.3.

The interpretation of Figure 7.3 is now straightforward: Varying the voltage on a gate tunes the closest dot-lead coupling exponentially, while leaving the other dot-lead coupling essentially untouched. For instance, we identify the dashed lines in Figure 7.3(b) with Γ_{1S} and the solid lines with Γ_{1N}. This level of control is highly desirable in a Cooper pair splitting device since it is predicted to provide a way to tune the ratio between cotunneling and Cooper pair splitting currents.

The tunability in the device was used to investigate the hybridization between the dot electron and quasiparticles in the superconductor. This work was done by Anders Jellinggaard et al. and is published in ref. [110]. For this study the right electrode was left floating and a single dot was tuned up in the left segment such that Γ_{1N} is the smallest energy scale in the system. In this configuration the system can exhibit various types of singlet subgap states, determined by the ratio U/Δ. A large U/Δ favors a single screened electron on the dot while a small U/Δ favors a superposition of zero and double occupation. By varying the dot-superconductor coupling the singlet subgap states are mixed and lowered in energy.

Figure 7.4 shows bias spectroscopy data for increasing values of V_{g3}. While gate 3 primarily tunes Γ_{1N} exponentially it also has an effect on Γ_{1S} that is generally unsystematic. We focus on the resonance labeled IV where V_{g3} does tune Γ_{1S} systematically so that higher n in Figure 7.4 gives smaller Γ_{1S}. At a_0 (that is, strong Γ_{1S}) the loop is open since the singlet states are sufficiently hybridized and low in energy that the doublet states never become the ground state. As n is increased (that is, Γ_{1S} is decreased) the loop gradually closes again as the hybridized singlets increase in energy and the doublet becomes the ground state. Between a_3 and a_4 a quantum phase transition occurs where the doublet and lowest singlet have the same energy.

Cooper pair splitting in the device was also investigated, but the results were not conclusive.

The results presented in this chapter shows that bottom gates can be em-

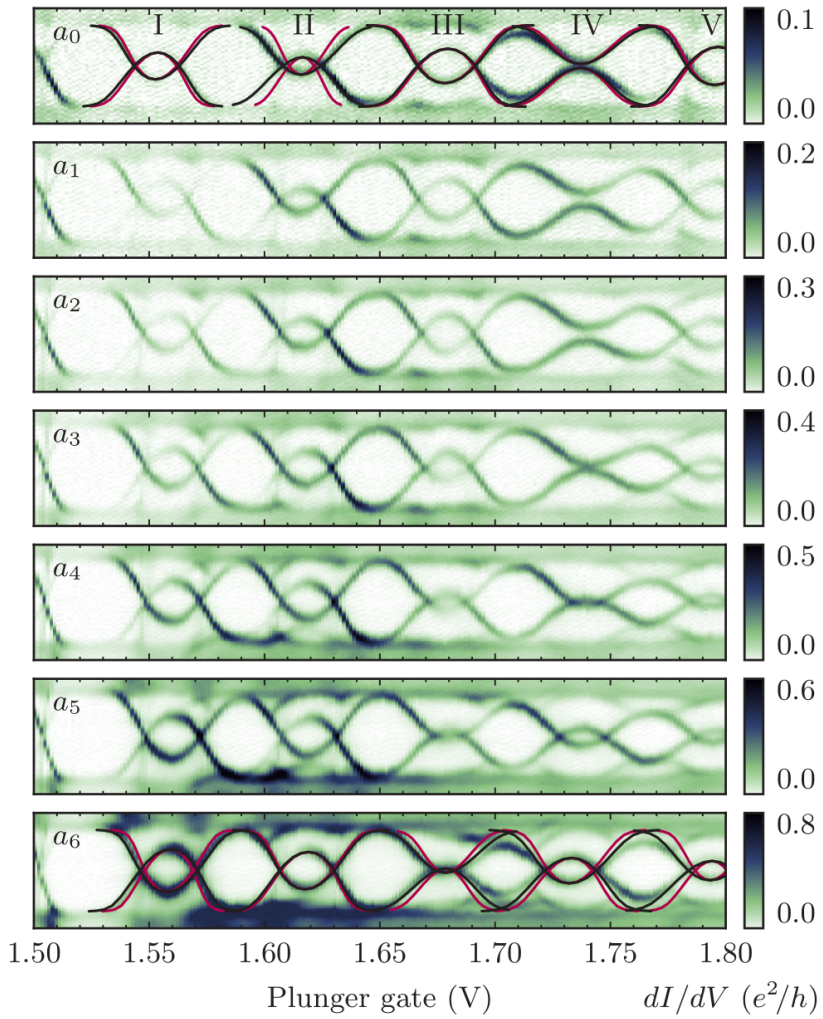

Figure 7.4: Bias spectroscopy data for a range of V_{g3}-values. The effect of V_{g3} on Γ_{1S} is generally unsystematic, except in resonance IV. Here, Γ_{1S} decreases with increasing n, thus tuning the resonance through a quantum phase transition. Adapted from [110].

ployed to efficiently control the dot-electrode coupling in a NW quantum dot device. The ability to change parameters independently is highly desirable since it enables strong tests of theoretical predictions. This is demonstrated with data on subgap transport in the dot.

Implementing bottom gates for on CNT devices is somewhat more challenging because of the high temperatures required for CNT growth. This can be solved by growing the tubes on a separate substrate and subsequently transferring them to a chip with the pre-defined device electrodes using stamping [118, 119, 120] or other methods [71]. Bottom gates that can withstand high temperatures have also been explored in the literature [121]. However, transfer of a curved, kinked or crossed nanotube would be necessary in order to obtain a device for the entanglement detection experiment.

Chapter 8

Conclusion and Outlook

This thesis describes fabrication, measurement and analysis of transport in carbon nanotube devices.

Carbon nanotubes are attractive to use in quantum devices because of their exotic, well-understood electronic properties. The spectrum in a carbon nanotube quantum dot are typically described in terms of shells which are sets of four states close in energy. This thesis builds on the understanding of the carbon nanotube spectrum by showing that the coupling between such shells can be straightforwardly included in the existing model by allowing the electrostatic potential to vary along the tube, rather than staying constant. The validity of the extended model is established by presenting inelastic cotunneling spectroscopy data which is in excellent correspondence with the model.

Furthermore, we present data from a curved carbon nanotube Cooper pair splitter device demonstrating that the intrinsic spin-orbit magnetic fields in the two segments of the device are non-collinear. Such a device allows precise predictions of spin directions in the nanotube, hence allowing future studies on, e.g., entanglement detection, Majorana bound states, and unconventional pairing in superconductors [10, 102, 42]. The presented data also shows that the nanotube device has low disorder which is a requirement for many nanotube applications. However, such low disorder is not typically obtained with the fabrication scheme used here. We provide fabrication details for the potential replication of the device. The impact of disorder on the validity of the entanglement detection experiment is also developed. We find that the experiment can be conducted in a finite disorder device if a modified Q parameter is used.

Continuing the study of the device above we present data on its Cooper pair splitting capabilities. We find that the bend of the nanotube along with its low disorder and high spin-orbit coupling satisfies the requirements for the entanglement detection experiment [10] that are typically considered difficult. However, the quantum dots in the device are too strongly coupled to the superconductor and too weakly coupled to the normal electrodes to

be well-suited for the above experiment. Still, the measurement of nonlocal signals that vanish in magnetic field is an indication that the device does produce a finite Cooper pair splitting current. Finally, the Q parameter is calculated and tested against the threshold value of 2. The obtained Q-values are all below 0.16 indicating that the Q parameter is robust against false positive $Q > 2$ results. This is reassuring for future experiments.

Finally, we report data from a bottom gated nanowire Cooper pair splitter device. We find that the electrode-dot couplings can be tuned independently and exponentially by the bottom gates as predicted by basic theory. Combining bottom gates with the low disorder and high spin-orbit coupling described above would yield a device ideal for the entanglement detection experiment [10]. Executing such a combination again ties back to the employment of novel fabrication techniques.

Where to go from here? There is no question that carbon nanotubes is an excellent platform for studying new physics. However, to perform such studies the increasing complexity and requirements of theoretical proposals must be matched by a corresponding increase in ingenious techniques for implementing said proposals. Although recent advances have yielded high-quality devices [1, 71] they have not done so consistently when implemented in other labs. Indeed, the enthusiasm for carbon nanotubes as a replacement for silicon has existed at least 20 years [122, 123] and yet, despite the slow-down of Moore's law [4], carbon nanotube transistors have only recently been shown to perform better than their silicon counterparts [124]. Conversely, a deep understanding of nanowire growth [125] has enabled, e.g., epitaxy of semiconductor-superconductor interfaces [126] which have made nanowires front-runners in the race for robust qubits [127, 128]. In the author's opinion a similar breakthrough is necessary for carbon nanotubes if their exotic properties are to be fully exploited.

Ice lithography [66, 67, 68, 69], in-situ selection of carbon nanotubes [71, 72] and chirality-selection [129, 130] are approaches to this problem. Ice lithography addresses the resist residue issue while in-situ selection provides the ability to test a number of nanotubes at cold temperatures until a high-quality specimen is found. Chirality selection is desirable since chirality determines whether the CNT is semiconducting or metallic. While it is possible to determine the chirality of a given nanotube [129] chirality-controlled growth [130, 131] as well as the general growth mechanism are still topics of current research [132, 133, 134]. If such techniques are able to provide consistent results they will set a new standard for carbon nanotube devices and enable a host of new studies.

As for the Cooper pair splitter, a couple of interesting questions are of current interest. One question concerns the piece of nanotube or nanowire directly under the superconducting electrode. Under certain conditions this

piece forms a "third site" [15, 135] which may cause interference with the dot electrons. To avoid such interference recent approaches have cut the nanowire under the superconducting electrode with focused ion beam (FIB) milling and/or used wide bottom gates to deplete the nanowire segment that remains [111]. Additional experiments using these techniques could shed light on the mechanisms that limit Cooper pair splitting efficiency and help explain why some devices do not show Cooper pair splitting at all.

The question of whether the splitting Cooper pair is entangled is still open. Other proposals for entanglement detection exist besides using spin-orbit magnetic fields in carbon nanotubes. These include using ferromagnetic leads [136, 137, 138], noise cross-correlation [139, 140, 141], or Tomonaga-Luttinger liquids [142].

In a broader perspective the Cooper pair splitting geometry can also host studies unrelated to Cooper pair splitting. As mentioned above these include (poor man's) Majorana bound states [102], coupling spin qubits [143], and controlling the character of the paired electrons [42]. A Cooper pair splitter device may also be used as a counterpart to STM measurements of magnetic impurities on the surface of superconductors [144]. Such impurities are of strong current interest since they host Majorana modes at their ends whose topological protection increases with the length of the chain [145, 146, 147]. In STM experiments magnetic adatoms such as Mn, Fe, Co and Ni play the role of the impurities with spin moments of 5/2, 2, 3/2 and 1. Conversely, quantum dots with an odd occupation of electrons have spin moments of 1/2 which are well understood. CPS devices also potentially provide a higher degree of control of couplings, charging energies etc. These features allow detailed studies of the smallest non-trivial chain with two impurities, often called an Andreev or Shiba molecule [62, 148]. Extending the chain would allow strong tests of theoretical predictions for Majorana modes while being in principle straightforward to implement experimentally.

Appendix A

Fabrication

A.1 Standard fabrication processes

This section contains information about default parameters and procedures for fabrication. Note that they do not necessarily represent optimized or best-practice values, but rather the values that were actually used, unless otherwise noted. **Fabrication process A.1.1**

Resist spinning

1. Clean chip in first acetone, then IPA. Sonicate when the chip is in acetone. If nanotubes are on the chip, do not sonicate.
2. Bake chip on hotplate for 4 minutes at 185°C.
3. Spin resist at 4000 revolutions per minute for 45 seconds.
4. Bake chip on hotplate for 3 minutes.
5. Repeat steps 3-4 for additional layers of resist.

Fabrication process A.1.2
CVD process for growing nanotubes.

Time			Gas flow (nL/min N_2)		
(minutes)	T_{set} (°C)	T_{oven} (°C)	Ar	H_2	CH_4
0	910	21	2	–	–
5	910	z	0.8	–	–
x	910	910	–	0.1	–
x+10	910	910	–	0.1	0.65
x+10+y	0	910	0.8	–	–

Here, x is the time when the oven reaches 910°C and y is the desired growth time. The temperature z varies from growth to growth.

Fabrication process A.1.3
Exposure settings for rough features, that is, features larger than about 500 nm.

- Area step size: 20 nm
- Dose: 390 µC/cm^2
- Write field size: 200 µm
- Aperture: 120 µm
- Voltage: 20 kV.

Fabrication process A.1.4
Exposure settings for fine features, that is, features smaller than about 500 nm.

- Area step size: 4 nm
- Dose: 390 µC/cm^2
- Write field size: 100 µm
- Aperture: 30 µm
- Voltage: 20 kV.

Fabrication process A.1.5
Development of PMMA resists.

1. Immerse chip in MIBK:IPA 1:3 for 55 seconds at room temperature.
2. Immerse chip in IPA for 55 seconds at room temperature.
3. Blow dry with N_2 gun.

A.2 Fabrication recipe for devA

Data from devA are presented in chapter 5. devA was known as `cnt_gen5_FI` during fabrication.

1. Cut out 1.1 cm × 2.0 cm chip with a 500 nm SiO_2 top layer.
2. Sonicate chip in acetone. Flush with IPA and dry with nitrogen.
3. Bake chip on hot plate at 185 °C for 4 minutes.
4. Spin resists EL-6 and A4 at 4500 rpm for 1 minute. Bake chip at 185 °C for 4 minutes between spinning EL-6 and A4 and after spinning A4.
5. Expose alignment mark pattern in the resist using an Elionix ELS-7000[1] and settings: Field size: 300 µm, dots: 20000, dose time: 0.22 µs, dose: 922 µC/cm^2, current: 10 nA, aperture 120 µm.
6. Develop chip in MIBK:IPA 1:3 for 90 seconds at room temperature, then 55 seconds in IPA at room temperature.
7. Ash 30 seconds before evaporating Ti/Pt (5/60 nm) in AJA evaporation chamber.
8. Lift-off in NMP at 80 °C in water bath for 25 minutes. Sonicate in NMP for 2 minutes and flush with transfer pipette.
9. Apply carbon nanotube catalyst to chip. See section A.3 for details.
10. Grow CNTs at 910 °C for 18 minutes. See fabrication process A.1.2 for details.
11. Take images of carbon nanotubes in SEM at an acceleration voltage of 1.5 kV. Use the following image properties: Size: 100 µm × 100 µm, resolution: 2000 points × 2000 points, point average: 1.
12. Design devices based on SEM images. DesignCad 23 was used for this purpose, but the author has later found LayoutEditor to be a superior program. A notable improvement over DesignCad is that it can make arbitrary transformations to imported images to align them to the design. It also provides faster rendering of the design+image combination.

[1] The ELS-7000 operates at an acceleration voltage of 100 kV while the minimum energy required to knock out a carbon atom of the nanotube is estimated at 86 keV [149]. Thus, the Raith eLine (variable acceleration voltage, but typically 20 kV) was used exclusively after nanotube growth to avoid damaging the nanotubes.

13. Flush chip in acetone and then IPA. Dry with nitrogen. Sonication should be avoided when CNTs are on the chip.

14. Spin resist EL-6 and A4 as in point 4.

15. Expose pattern for normal contacts in the resist using Raith eLine. Settings for inner contacts are given in A.1.4. Settings for outer contacts are given in A.1.3.

16. Develop chip in MIBK:IPA 1:3 for 55 seconds at room temperature, then 55 seconds in IPA at room temperature.

17. Evaporate Au on the chip using Edwards Auto 306 thermal evaporator.

18. Spin resist EL-6 and A4 as in point 4.

19. Expose pattern for superconducting contacts in the resist using Raith eLine. Settings for inner contacts are given in A.1.4. Settings for outer contacts are given in A.1.3.

20. Develop chip in MIBK:IPA 1:3 for 55 seconds at room temperature, then 55 seconds in IPA at room temperature.

21. Evaporate Ti/Al on the chip in AJA evaporation chamber.

If the metals used for the device are not suitable for bonding an additional lithography step is required to define bonding pads. This was the case for the fabrication of devA where an additional lithography step of Ti/Au 10/90 nm was done. Generally, the Au lithography step (point 15) should be last because Au doesn't adhere well to the chip surface[2]. The reason that it's not the last step in the recipe above is that the intention was to deposit titanium as a sticking layer below the gold. This did not work out for various reasons.

A.3 Deposition of carbon nanotube catalyst

It took a few tries to figure out an efficient way of depositing the CNT catalyst on the wafer. The below recipe was found to work consistently for the catalyst consisting of iron nitrate ($Fe(NO_3)_3$) molybdenum acetate and alumina support particles[3]. Note that this recipe is designed for dot exposures in a Raith eLine. It consistently yielded catalyst dots with radii of 2 µm with little to no catalyst contamination on the rest of the chip. It might not work with area exposures below a certain size unless the exposure parameters are changed.

[2] This is even more of a problem when using leads made of Pd which adheres poorly to the chip surface.

[3] The catalyst itself was introduced by Kong et al. [89].

1. Spin A6 PMMA at 4500rpm for 1 minute.
2. Bake at 185 °C for 1 minute.
3. Spin another layer of A6 PMMA at 4500rpm for 1 minute to yield a double-layer of A6.
4. Bake at 185 °C for 1 minute.
5. Expose catalyst pattern using dot exposure with parameters: Dose: 350 µC/cm^2, area step: 10 nm, dot dose: 0.1 pA, write field: 200 µm, acceleration voltage: 20 kV, aperture: 30 µm. It is important in this step that you scan as little as possible on the chip when finding alignment marks and aligning. If possible you should know the distance from an alignment mark to the corner of your chip and jump directly to it rather than searching for it. Accidentally exposing resist promotes sticking of catalyst to the chip in that spot. Catalyst that sticks accidentally to the chip is typically more prone to being scattered on the chip in subsequent steps.
6. Develop for 55 seconds in MIBK:IPA 1:3, then 55 seconds in IPA.
7. Stir catalyst solution for 2 minutes or more.
8. For a 1 cm × 2 cm chip apply 4 drops of catalyst using a transfer pipette.
9. Let the chip dry under a petri dish for about 11 minutes. The duration is probably not important as long as the chip is completely dry. The purpose of the petri dish is to avoid stray drops of liquid hitting the chip.
10. Bake the chip for 7 minutes at 185 °C.
11. Lift-off in 100 mL NMP for two hours at 76 °C.
12. At this point the chip can be sonicated if it is absolutely necessary. Sonication is efficient in removing catalyst resting on resist, but it also shakes loose and scatters catalyst resting on the chip. Typically, sonication is not necessary if the chip has been sitting in NMP long enough at 76 °C.
13. Spray the chip thoroughly with acetone to remove unwanted catalyst residues before moving the chip to IPA and drying it.

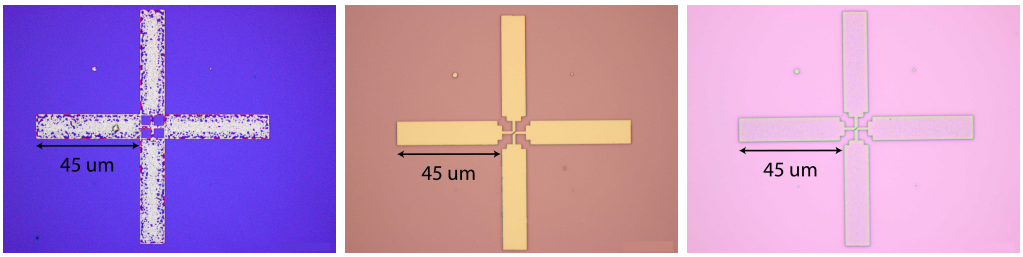

Figure A.1: Left: Titanium/platinum alignment mark after exposure to CNT growth. Middle: Tantalum mark before exposure to heat. Right: The same Tantalum mark after exposure to CNT growth.

A.4 Other fabrication issues

A.4.1 Alignment marks for CNT devices

When working with carbon nanotubes it is preferred to expose them to as few lithography steps as possible when they are on the chip to avoid introducing disorder and resist contamination. Thus, alignment marks should preferentially be done before the CVD growth. However, not all metals can withstand exposure to the high temperatures of the CVD growth process (see, e.g., A.1.2). A common solution [1, 17, 150] is to use a tungsten/platinum metal stack which have high melting points of 1768°C and 3422°C, respectively. For this project tungsten was initially substituted by titanium due the the former being unavailable.

In the left panel of Figure A.1 a alignment mark with the metal stack Ti/Pt (5/90nm) is shown after being exposed to a CVD growth similar to A.1.2. This degradation of the metal is known as titanium-platinum agglomeration [151] and in this alignment mark it impedes, e.g., the mark's use for automatic alignment. It may cause smaller marks to be unusable altogether, even for manual alignment.

Tantalum with a melting point of 3020°C does not show this problem. Comparing Figure A.1 middle (before growth) and right panel (after growth) we see that the alignment mark maintains its shape nicely. We attribute the change in color to the formation of Ta_2O_5. Since tantalum has a high superconducting transition temperature its resilience to the CVD growth process would indicate that it's an interesting candidate for electrodes for "clean" nanotube devices. However, we have found that after CVD growth the tantalum film is typically insulating at room temperature which indicates that it would not turn superconducting at low temperature.

A.4.2 Choosing resist for CNT devices

In this thesis PMMA resist is usually chosen for e-beam lithography. Some investigations find that ZEP520A is superior for obtaining low-resistance

contact to carbon nanotubes. The hypothesis is that the low surface adhesion, low molecular-weight, low clearing-dose and high sensitivity of the ZEP copolymer decrease the amount of resist residue left behind after development [64, 65]. These residues are thought to have great effect on the contact between metal and CNT.

Hoping to improve the device yields we attempted the ZEP520A as well, changing most other steps in the fabrication process as well, according to the references above. Notably, as the clearing dose of ZEP520A is much lower than PMMA, the current and consequently the aperture of the SEM must be changed.

Despite closely adhering to the procedure given in [64, 65] and visiting the University of Basel where this process is used, no difference in low-resistance device yield was observed in our lab. This negative result indicates that there are more than one crucial step in CNT device fabrication.

Another step commonly thought to be crucial is metal evaporation which is also a determining factor for the CNT-metal interface. The Paris group run by Takis Kontos obtain good CNT devices with a nitrogen-cooled Plassys evaporator with a low base pressure of $< 5 \times 10^{-10}$ mbar. The device is left to sit overnight in the evaporator overnight to allow potential outgassing of resist, thereby decreasing resist residues. Although the Paris group uses PMMA they also use a lower current (aperture) of ≈ 20 pA (10 µm) at 20 kV. The settings given in section A.1.4 lead to a substantially higher current of ≈ 300 pA. At face value a current of 20 pA would be more appropriate for ZEP520A than for PMMA where it leads to long exposure times due to PMMA's higher sensitivity. Given the higher yield in the Paris group, it raises the question, however, whether a high current can damage the nanotube similarly to a high voltage [149].

A.4.3 Miscellaneous fabrication tips

The author has found that the exact position of the nanotubes in SEM images sometimes differed from their position after fabricating electrodes. One obvious explanation is misalignment which causes the device shift, rotate or magnify relative to the tube. There are some indications, however, that spraying the chip, either with a plastic pipette or using a N_2 gun causes a larger displacement of the tubes. This should be avoided, if possible.

Due to yield issues a sample was designed to test the sensitivity of the CNT-metal interface to e-beam dose. Surprisingly, the author found high conductances larger than e^2/h independent of the dose which varied between 0.8 and 1.9 times a base dose of 390 µC/cm^2. This result is contrary to those found by Samm et al. [64] who find that the resistance of the CNT devices strongly depends on the dose. Note, however, that the result in [64] is for the ZEP520A resist. Some of the tubes on the test sample had conductances larger than $4e^2/h$ indicating double-walled CNTs, which may

contact differently to metal than single-walled CNTs.

Initially in this project the author had issues with write field errors in the Raith eLine. Write field errors occur when the electromagnetic deflection of the electron beam and the laser movement of the stage are not precisely adjusted. The symptom is gaps in metal structures, which of course breaks devices. An easy fix is to increase the write field magnification values by, says 1% after doing adjustment. This will enlarge all structures by 1%, ensuring overlap between write fields. This fix should obviously not be used for structures that are size-sensitive.

Gaps in structures which do not cross a write field may be caused by the following setting in the eLine: `Patterning Details -> Area Mode -> Direction mode -> Scan direction`. Setting this to `preset U` rather than `automatic longest` solved the gap problem for the author.

On the topic of write field adjustment the author stresses the importance of using narrow alignment marks. A width of, e.g., 1 µm may be too much to get proper definition of the center when doing manual adjustment. The author uses alignment marks in the shape of a plus that decrease in width from 1 µm at the tips to 100 nm at the center.

Appendix B

Miscellaneous data

B.1 CNT devices with vanadium electrodes

For the Cooper pair splitter geometry a large superconducting gap Δ is desirable since it suppresses unwanted cotunneling processes (see section 2.3.2) if $U > \Delta$. This is the typical regime for quantum dots with dimensions $\lesssim 500\,\text{nm}$ and leads of aluminium or superconductors with similar gap magnitude. Bulk vanadium has a superconducting gap of $\Delta = 1.6$ meV [44] while a thin film of vanadium has been observed with a gap of $\Delta = 0.55$ meV [152]. Both of these values are significantly larger than that in aluminium.

In the present work 2-terminal nanotube devices were fabricated with vanadium leads at a separation of 300 nm. Figure B.1 shows bias spectroscopy from one such device exhibiting a superconducting gap of $\Delta = 0.65$ meV, consistent with [152]. The vanadium-specific part of fabrication is as follows:

1. Spin resists EL6 and A4 according to fabrication process A.1.1.
2. Expose leads using settings in A.1.4.
3. Develop chip using A.1.5.
4. Evaporate 5 nm titanium followed by 90 nm vanadium in AJA. The evaporation was done at 10 kV with currents of (Ti) 18.7 mA and (V) 30.6 mA and rates of (Ti) 0.75 Å/s and (V) 1.2 Å/s. The base pressure of the evaporation chamber was 1.2×10^{-8} Torr before loading the chip. The pressure during evaporation was not recorded, but is typically found to be lower than 5×10^{-7} Torr.
5. Lift-off in NMP in water bath at 80°C for 2 hours. Flush chip with 7.5 mL plastic pipette to remove any remaining metal film.

Bias spectroscopy from one such device is shown in Figure B.1. In the plot we see Coulomb blockade with subgap resonances in the regions with

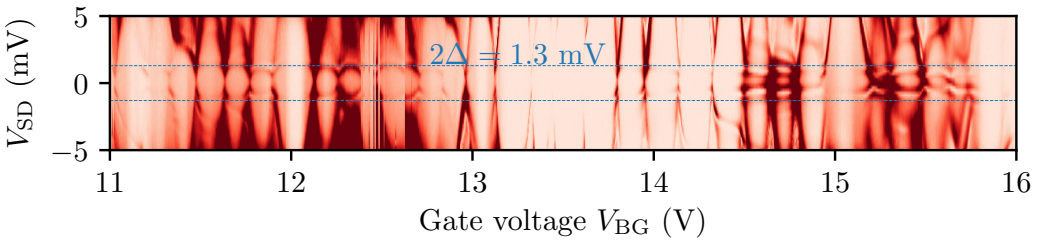

Figure B.1: Bias spectroscopy of a 2-terminal carbon nanotube device with superconducting titanium/vanadium leads at 300 mK. The superconducting character of the leads is reflected in the presence of subgap states for $|V_{SD}| < 1.3$ mV.

strong dot-lead coupling for biases below the superconducting gap of about $\Delta = 0.65$ meV. The subgap states extend to a bias of 2Δ because both leads are superconducting. Having two superconducting leads rather than one superconducting and one normal also complicates the appearance of the subgap states since both leads have non-trivial density of states. To obtain the subgap spectrum of one superconductor one would have to deconvolve the density of states of the other superconductor from the data.

Despite this promising result similar subsequent devices did not exhibit any superconducting gaps. One of these subsequent samples were fabricated using thermal evaporation in an Edwards Auto 306 thermal evaporator instead of the e-beam evaporation in step 4. above. The thermally deposited vanadium was *hard* to lift-off, requiring more than 10 hours in both hot (85°C) and room-temperature NMP and blasting with a nitrogen gun in the NMP solution. Possibly due to the harsh lift-off treatment the devices on the chip did not show a high enough conductance to warrant a cool-down. The difficult lift-off process may have been caused by the high melting point of vanadium of 1910°C. Metals with high melting points require high currents in an evaporation chamber before reaching evaporation. This warms up the chamber and may cause the resist to bake and harden.

To investigate the dependence of fabrication parameters of the vanadium film a series of thin films of Ti/V 5/60 nm were fabricated following the above recipe, but without nanotubes. The test films were fabricated at widths of 300 nm, 500 nm, 1 µm and 5 µm. Current-biased measurements at low temperature showed that only the 5 µm film exhibited a superconducting transition. This transition occurred between 300 mK and 2.5 K while for a BCS-type superconductor with the above gap of 0.65 meV a superconducting temperature $T_C \approx \Delta/(1.75k_B) \approx 4.3$ K is expected. Two hypotheses were put forward as to the low transition temperature and absence of superconducting transitions:

1. Contamination of the vanadium by atmospheric oxide. Depending on the oxidation depth of the material a thin vanadium film may not have

enough bulk left to maintain the superconducting phase.

2. Contamination of the vanadium by resist from the lithography process. The high energies required to evaporate vanadium may cause outgassing of resist from the sample. The resist polymers are consequently incorporated into the metal film reducing its purity.

To test hypothesis 1. a new, similar sample was fabricated with a metal stack of Ti/V/Al 5/60/10 nm such that the native aluminium oxide would prevent oxide migration into the vanadium. However, no improvement was observed in the transition temperatures for this sample. Because of these issues the vanadium film was abandoned in favor of tantalum which at that point in the project had a higher transition temperature, both nominally and practically.

Appendix C

Methods

C.1 Lock-in measurements

In transport studies in condensed matter physics we often want to measure the differential conductance $\mathrm{d}I/\mathrm{d}V$ in some mesoscopic circuit. This section explains how such measurements can be made with a lock-in amplifier.

The current I_{sig} through the circuit is caused by an AC+DC voltage

$$V = V_0 + V_L \cos\omega t = V_0 + V_{\mathrm{ref}} \tag{C.1}$$

applied across the device. Assuming I_{sig} is a function of V only, we can Taylor expand it around V_0[1]

$$\begin{aligned} I_{\mathrm{sig}}(V) &= I_{\mathrm{sig}}(V_0) + \left.\frac{\mathrm{d}I_{\mathrm{sig}}}{\mathrm{d}V}\right|_{V=V_0} V_L\cos(\omega t) + \frac{1}{2}\left.\frac{\mathrm{d}^2 I_{\mathrm{sig}}}{\mathrm{d}V^2}\right|_{V=V_0} V_L^2\cos^2(\omega t) + \ldots \\ &= \sum_n^\infty \frac{1}{n!}\left.\frac{\mathrm{d}^n I_{\mathrm{sig}}}{\mathrm{d}V^n}\right|_{V=V_0} V_L^n \cos^n(\omega t) \end{aligned} \tag{C.2}$$

We are following the terminology in the Stanford Research Systems 830 (SR830) lock-in manual [153] so that *signal* denotes the input to the lock-in and *reference* denotes the output from the lock-in. In the following we will disregard phase difference between the signal and reference as well as X and Y components since these can be easily calculated from the results given here.

Inside the lock-in the signal (C.2) is multiplied with the reference signal by a phase sensitive detector:

$$I_{\mathrm{sig}}(V) V_L \cos\omega t = \sum_n^\infty \frac{1}{n!}\left.\frac{\mathrm{d}^n I_{\mathrm{sig}}}{\mathrm{d}V^n}\right|_{V=V_0} V_L^{n+1}\cos^{n+1}(\omega t). \tag{C.3}$$

[1] Typically, the current I_{sig} is converted to a voltage in a current amplifier and measured in the lock-in amplifier as a voltage. Below, we will use I_{sig} in the equations for clarity. Results for a measured voltage can be obtained by replacing $I_{\mathrm{sig}} \to gV_{\mathrm{sig}}$ throughout, where g is the gain of the current amplifier and V_{sig} is the voltage signal measured in the lock-in.

Split the sum in odd and even n to separate even and odd powers of $\cos\omega t$

$$\begin{aligned} I_{\text{sig}}(V)V_L\cos\omega t &= I_{\text{sig}}(V_0)V_L\cos\omega t \\ &+ \sum_{n=1,2\ldots}^{\infty}\left\{\frac{1}{(2n-1)!}\left.\frac{\mathrm{d}^{2n-1}I_{\text{sig}}}{\mathrm{d}V^{2n-1}}\right|_{V=V_0} V_L^{2n}\cos^{2n}(\omega t)\right. \\ &\left. + \frac{1}{(2n)!}\left.\frac{\mathrm{d}^{2n}I_{\text{sig}}}{\mathrm{d}V^{2n}}\right|_{V=V_0} V_L^{2n+1}\cos^{2n+1}(\omega t)\right\} \\ &= I_{\text{sig}}(V_0)V_L\cos\omega t \\ &+ \sum_{n=1,2\ldots}^{\infty}\frac{1}{(2n-1)!}\left.\frac{\mathrm{d}^{2n-1}I_{\text{sig}}}{\mathrm{d}V^{2n-1}}\right|_{V=V_0} V_L^{2n}\cos^{2n}(\omega t) \\ &+ \sum_{n'=2,3,\ldots}^{\infty}\frac{1}{(2(n'-1))!}\left.\frac{\mathrm{d}^{2(n'-1)}I_{\text{sig}}}{\mathrm{d}V^{2(n'-1)}}\right|_{V=V_0} V_L^{2n'-1}\cos^{2n'-1}(\omega t) \end{aligned} \tag{C.4}$$

After the phase sensitive detector the signal is put through a low-pass filter that removes all AC components. As (C.4) stands, it is not clear whether there are DC components hidden in the powers of $\cos\omega t$. By using the following trigonometric identities ([154] eq. (12.71) and (12.73) we can see clearly which terms are AC and which are not:

$$\begin{aligned} \cos^{2n-1}A = \frac{1}{2^{2n-2}}\Bigg\{ &\cos(2n-1)A + \binom{2n-1}{1}\cos(2n-3)A \\ &+\cdots+\binom{2n-1}{n-1}\cos A\Bigg\} \end{aligned} \tag{C.5}$$

$$\begin{aligned} \cos^{2n}A = \frac{1}{2^{2n}}\binom{2n}{n} + \frac{1}{2^{2n-1}}\Bigg\{ &\cos 2nA + \binom{2n}{1}\cos(2n-2)A \\ &+\cdots+\binom{2n}{n-1}\cos 2A\Bigg\}. \end{aligned} \tag{C.6}$$

We see that all odd powers of $\cos\omega t$ are AC and that even powers of $\cos\omega t$ only contains one DC term: $2^{-2n}\binom{2n}{n}$. Consequently, the output of the low-pass filter is

$$\begin{aligned} \mathrm{LPF}(I_{\text{sig}}(V)V_L\cos\omega t) &= \sum_{n=1,2\ldots}^{\infty}\frac{1}{(2n-1)!}\frac{1}{2^{2n}}\binom{2n}{n}\left.\frac{\mathrm{d}^{2n-1}I_{\text{sig}}}{\mathrm{d}V^{2n-1}}\right|_{V=V_0} V_L^{2n} \\ &= \sum_{n=1,2\ldots}^{\infty}\frac{2^{1-2n}}{n!(n-1)!}\left.\frac{\mathrm{d}^{2n-1}I_{\text{sig}}}{\mathrm{d}V^{2n-1}}\right|_{V=V_0} V_L^{2n} \end{aligned} \tag{C.7}$$

The zero-order term in eq. (C.4) is also removed since it contains $\cos\omega t$.

Before the lock-in outputs this expression on its display as the R value it divides by V_L to take account for the factor introduced when the reference signal was multiplied

$$R = \frac{1}{V_L}\mathrm{LPF}(I_{\mathrm{sig}}(V)\cos\omega t) = \sum_{n=1,2\ldots}^{\infty} \frac{2^{1-2n}}{n!(n-1)!} \left.\frac{\mathrm{d}^{2n-1}I_{\mathrm{sig}}}{\mathrm{d}V^{2n-1}}\right|_{V=V_0} V_L^{2n-1}. \quad \text{(C.8)}$$

Let's calculate a few terms of R:

$$R(n=1) = \frac{1}{2} \left.\frac{\mathrm{d}I_{\mathrm{sig}}}{\mathrm{d}V}\right|_{V=V_0} V_L \quad \text{(C.9)}$$

$$R(n=2) = \frac{1}{16} \left.\frac{\mathrm{d}^3 I_{\mathrm{sig}}}{\mathrm{d}V^3}\right|_{V=V_0} V_L^3 \quad \text{(C.10)}$$

$$R(n=3) = \frac{1}{384} \left.\frac{\mathrm{d}^5 I_{\mathrm{sig}}}{\mathrm{d}V^5}\right|_{V=V_0} V_L^5 \quad \text{(C.11)}$$

Post-processing in the lock-in may or may not scale the output so that the numerical pre-factor for the $n = 1$ term is cancelled.

Thus, by choosing the reference signal to have the same frequency ω as the input signal we can measure the differential conductance $\mathrm{d}I/\mathrm{d}V$ by (C.9). The measurement includes higher order derivatives of I_{sig}, but they are attenuated by a fast-growing pre-factor.

Suppose we instead chose the reference signal to be twice the input signal frequency 2ω. Measuring at multiples of the input frequency is called measuring the *harmonics* of the signal. Repeating the procedure above we arrive at an expression for the second harmonic output

$$R_{2\omega} = -I_{\mathrm{sig}}(V_0) + \sum_{n=1,2,\ldots}^{\infty} \frac{2^{-2n}}{(n+1)!(n-1)!} \left.\frac{\mathrm{d}^{2n} I_{\mathrm{sig}}}{\mathrm{d}V^{2n}}\right|_{V=V_0} V_L^{2n}. \quad \text{(C.12)}$$

This expression involves only even derivatives of I_{sig}, including the DC term $-I_{\mathrm{sig}}(V_0)V_L$. In order to get rid of this unwanted DC term some lock-ins have a high-pass filter at the input[2].

Calculating a few terms of the sum in (C.12) gives

$$R_{2\omega}(n=1) = \frac{1}{8} \left.\frac{\mathrm{d}^2 I_{\mathrm{sig}}}{\mathrm{d}V^2}\right|_{V=V_0} V_L^2 \quad \text{(C.13)}$$

$$R_{2\omega}(n=2) = \frac{1}{96} \left.\frac{\mathrm{d}^4 I_{\mathrm{sig}}}{\mathrm{d}V^4}\right|_{V=V_0} V_L^4 \quad \text{(C.14)}$$

$$R_{2\omega}(n=3) = \frac{1}{3072} \left.\frac{\mathrm{d}^6 I_{\mathrm{sig}}}{\mathrm{d}V^6}\right|_{V=V_0} V_L^6 \quad \text{(C.15)}$$

[2] This setting is called "AC vs DC coupling" on the SR830 lock-in.

The second harmonic output gives direct access to the second derivative of the current which may contain important information about the underlying physical system.

Importantly, obtaining the derivatives directly from the lock-in output avoids numerical differentiation of current data which often introduces additional noise.

Standard lock-in measurements are used throughout the thesis to obtain $\mathrm{d}I/\mathrm{V}$ data. Second harmonic lock-in measurements were used to obtain the $\mathrm{d}^2I/\mathrm{V}^2$ data in [23] while numerical differentiation was used to obtain the $\mathrm{d}^2I/\mathrm{V}^2$ data in chapters 5 and 4.

C.2 Baseline subtraction for nonlocal signals

In order to extract the additional nonlocal signal ΔG on top of a conductance signal the baseline must be subtracted. Consider the data in Figure C.1a) and c). Sweeping over peaks in the right dot (c)) gives rise to nonlocal signals in the left dot (a)). However, the right mix gate slightly perturbs the baseline conductance in the left dot due to imperfect coefficients in the definition of the mix gates in eq. (6.2). Common strategies for baseline subtraction address this problem with varying degrees of success:

1. Subtracting the average of the conductance, Figure C.1, blue. This method does not take drift into account. Also, the average depends on the height of the peaks which leads to incorrect detection of a negative nonlocal signal between the peaks.

2. Subtracting a fitted polynomial, Figure C.1a), orange. This method takes care of the drift as long as the drift is not too large. The method still suffers from dependence on peak heights, however.

We propose a new algorithm which yields representative values of ΔG as long as peak widths are narrower than the separation between peaks and the drift can be captured with a polynomial of finite order:

1. Fit data with a polynomial of degree `deg`.

2. Subtract the polynomial from the data.

3. Set the fraction $1 -$ `keep_frac` of points that are furthest from the median to the value of the median. After subtracting the polynomial from the data the median lies on the true baseline and the points furthest from the median are peaks. Essentially, this step "drags down" points on the peaks to lie on the baseline.

4. repeat the above steps `n_iter` times.

The result of applying this algorithm is shown in Figure C.1a) and b). In this project good results have been obtained using `deg` $= 2$, `keep_frac` $= 0.9$ and `n_iter` $= 5$. In some cases the baseline acts erratically and the order of the polynomial must be increased. Also, if the peaks are wider than their separation the median may no longer lie on the baseline. However, as the peaks widen beyond this point the notion of a baseline is increasingly ill-defined. Note that the new algorithm also correctly handles datasets with both positive and negative nonlocal signals.

Another option for baseline subtraction is to use Gaussian smoothing. The performance of this approach has not been investigated by the author.

A Python implementation of the algorithm is presented in the following. The implementation is fast since the heavy lifting is done with the vectorized operations in the Numpy library. Note the use of `numpy.polynomial.polynomial` rather than `numpy.polyfit` which is deprecated.

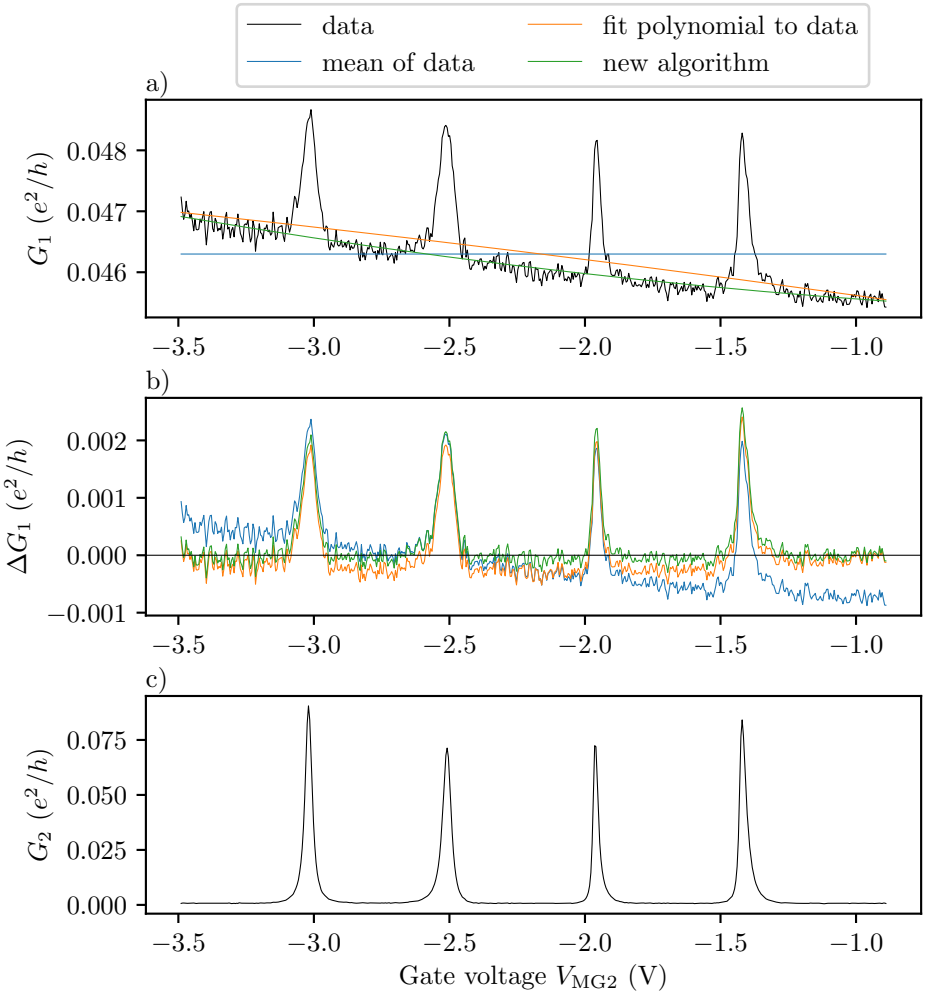

Figure C.1: Comparison of baseline subtracting algorithms. a) To find the baseline of the conductance data (black) one can, e.g., take the mean (blue), fit a polynomial (orange) or use the new algorithm proposed here (green). The performance of the algorithms depends on whether they are robust against, e.g., changes in peak heights or drift. b) Subtracting the obtained baseline gives the nonlocal signal ΔG. Taking the mean (blue) does not take drift into account, while fitting a polynomial (orange) gives false detection of negative nonlocal signals between peaks. The new algorithm is the best performer and represents the nonlocal signal accurately. c) Peaks in the opposite (right) dot which give rise to the nonlocal signals. The large range on the y-axis causes the G_R data to appear noiseless. The data presented here comes from averaged sweeps of Figure 6.2 at $V_{MG1} = -3\,V$.

```
import numpy as np
import numpy.polynomial.polynomial as po

def fit_baseline(ys, n_iter=5, keep_frac=0.9, deg=2, axis=0):
    """
    Iteratively fit a polynomial of degree `deg` to data in `ys
        `.
    In every iteration a fraction 1-`keep_frac` of the points
    in `ys` is set to the median of the current `ys`.
    For data with sufficiently narrow peaks (positive or
    negative) the fit converges to the baseline of the
    original data (until too many points are set to the median).

    Parameters
    ----------
    ys: ndarray, 1D or 2D
        Array to fit.
    n_iter: int
        Number of iterations to perform.
    keep_frac: float
        Fraction of points to not set to median in every
           iteration.
    deg: int
        Degree of polynomial to fit.
    axis: int
        Axis along which to fit. Must be 0 if `ys` is 1D.

    Returns
    -------
    fit_out: ndarray of size ys.shape
        Array with final fit.
    """
    if axis == 1:
        ys = ys.T
    n_valid = ys.shape[0]
    xs = np.linspace(0, 1, n_valid)
    fit_out = np.zeros(shape=ys.shape, dtype=float)
    for _ in range(n_iter):
        coef = po.polyfit(xs, ys, deg=deg)
        fit = po.polyval(xs, coef)
        fit_out = fit_out + fit.T
        ys = ys - fit.T
        med = np.median(ys, axis=0)
        y_delta = np.abs(ys-med)
        keep_n = int(n_valid*keep_frac)
        threshold = np.sort(y_delta, axis=0)[keep_n]
        n_valid = keep_n
        np.putmask(ys, y_delta >= threshold, med)
    if axis == 1:
        fit_out = fit_out.T
    return fit_out
```

C.3 The cntSpectrum Python package

The amount of carbon nanotube modeling in this thesis motivated the author to develop a robust implementation of the four-level model [24] in Python. The result is the cntSpectrum package available at `https://github.com/mchels/cntSpectrum/`. The primary use case of the package is to generate the spectrum and excitation spectrum of a single four-level carbon nanotube shell given the intrinsic parameters Δ_{SO}, $\Delta_{KK'}$ and μ_{orb} and values for the magnetic field. For instance, the code from the file `simple_example.py`

```
from cntspectrum import cntSpectrum
import numpy as np
import matplotlib.pyplot as plt
model_kw = {
    'deltaSO': 0.15,
    'deltaKK': 0.07,
    'mu_orb': 0.15,
    'J': 0.12,
}
model = cntSpectrum(**model_kw)
B_fields = 2
B_angles = np.linspace(0, np.pi, 46)
spectrums = model.get_spectrums(B_fields, B_angles, two_electron
    =False)
fig, ax = plt.subplots()
ax.plot(B_angles, spectrums.squeeze())
ax.set_xlabel('Magnetic field angle (radians)')
ax.set_ylabel('Energy (meV)')
plt.show()
```

produces the plot shown in Figure C.2. The methods `get_spectrums` and `get_ex_spectrums` are available from the class `cntSpectrum` which is initialized with the intrinsic parameters given above. The magnetic field values are only passed to the methods, not at initialization. For the pairs μ_{orb}, g_{orb} and Δ_{SO}, B_{SO} only one parameter must be given. The other is available for convenience as an attribute in the class as shown in the code snippet below

```
model = cntSpectrum(deltaSO=0.15, deltaKK=0.07, mu_orb=0.15, J
    =0)
print(model.BSO)
# prints 1.2975778546712804
print(model.g_orb)
# prints 2.595155709342561
```

As a secondary use-case the package can calculate expectation values for the spin vector for a given basis. The class `cntSpin` is initialized with a basis and has the methods `get_spin_vector` and `get_spin_vectors_from_eigenstates`. The latter method takes the eigenvector output from the `get_spectrums` method and calculates the spin vectors.

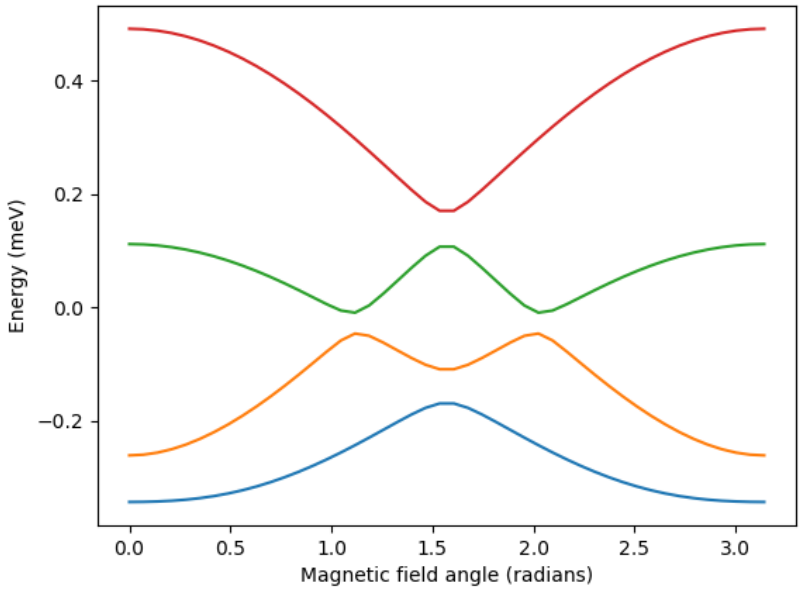

Figure C.2: Calculated carbon nanotube spectrum with parameters $\Delta_{\mathrm{SO}} = 150\,\mu\mathrm{eV}$, $\Delta_{KK'} = 70\,\mu\mathrm{eV}$ and $\mu_{\mathrm{orb}} = 150\,\mu\mathrm{eV}$, $J = 120\,\mu\mathrm{eV}$, $B = 2\,\mathrm{T}$ and a magnetic field angle between 0 and π. Plot generated by the code given in this section and the spectrum is calculated using the cntSpectrum Python package.

Finally, the function `get_ex_spectrums` in `base.py` calculates the excitation spectrum for a general spectrum and number of occupied states. This function can be used for non CNT-data as well.

The package contains tests where the output of various methods is compared against experimentally verified values. The implementation is done in Numpy where possible, which ensures fast processing. We refer to documentation in the code for more information.

C.4 The FolderBrowser Python package

A challenge in transport measurements is visualizing large amounts of data. For this purpose the FolderBrowser package was developed in Python by the author. The package defines a graphical user interface (GUI) which is shown in Figure C.3.

The FolderBrowser package allows plotting of data acquired with the matlab-qd framework with the following features

1. All standard Matplotlib controls (zoom, pan etc.) are available.

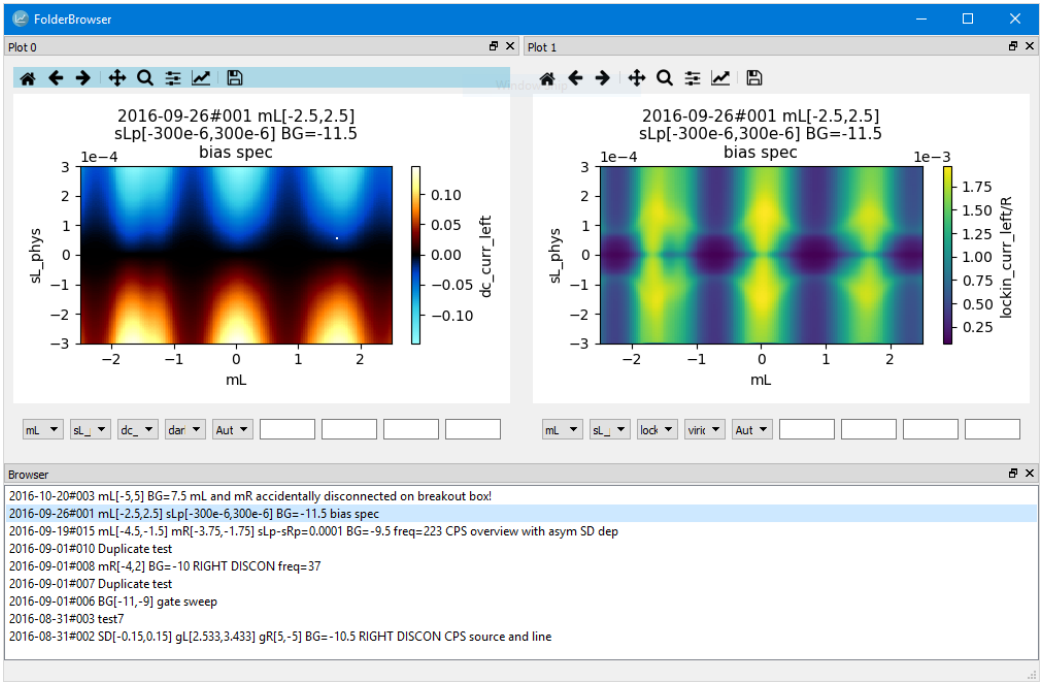

Figure C.3: An example of the FolderBrowser GUI. Note that the size, number and position of sub-windows are adjustable.

2. Additionally, colormap, plot type, limits and aspect ratio can be controlled.

3. Any data column in the dataset can be plotted against any other column.

4. The figure can be copied to the clipboard as a png file.

5. Code for generating the figure can be copied to the clipboard.

6. The figures can be modified interactively from a Jupyter notebook.

7. The FolderBrowser window can host as many plots as required and the layout can be configured on-the-go.

8. The backend can be easily configured to allow data in other formats than the one used by matlab-qd.

For more details, see the GitHub repository at `https://github.com/mchels/FolderBrowser`.

Bibliography

[1] J. Cao, Q. Wang, and H. Dai. Electron transport in very clean, as-grown suspended carbon nanotubes. *Nature Mat.*, 4(10):745–749, 2005.

[2] G. E. Moore. Cramming more components onto integrated circuits. *Electronics*, 38:114–117, 1965.

[3] G. E. Moore. Progress In Digital Integrated Electronics. *IEDM Tech. Digest*, pages 11–13, 1975.

[4] M. M. Waldrop. The chips are down for Moore's law. *Nature (London)*, 530:144–147, 2016.

[5] D. P. DiVincenzo. The Physical Implementation of Quantum Computation. *Progress of Physics*, 48:771–783, 2000.

[6] D. Loss and D. P. DiVincenzo. Quantum computation with quantum dots. *Phys. Rev. A*, 57:120–126, Jan 1998.

[7] L. N. Cooper. Bound Electron Pairs in a Degenerate Fermi Gas. *Phys. Rev.*, 104:1189–1190, Nov 1956.

[8] J. Bardeen, L. N. Cooper, and J. R. Schrieffer. Microscopic Theory of Superconductivity. *Phys. Rev.*, 106:162–164, Apr 1957.

[9] J. Bardeen, L. N. Cooper, and J. R. Schrieffer. Theory of Superconductivity. *Phys. Rev.*, 108:1175–1204, Dec 1957.

[10] B. Braunecker, P. Burset, and A. Levy Yeyati. Entanglement detection from conductance measurements in carbon nanotube cooper pair splitters. *Phys. Rev. Lett.*, 111(13):136806, 2013.

[11] L. G. Herrmann, F. Portier, P. Roche, A. Levy Yeyati, T. Kontos, and C. Strunk. Carbon Nanotubes as Cooper-Pair Beam Splitters. *Phys. Rev. Lett.*, 104(2):026801, 2010.

[12] J. Schindele, A. Baumgartner, and C. Schönenberger. Near-Unity Cooper Pair Splitting Efficiency. *Phys. Rev. Lett.*, 109:157002, Oct 2012.

[13] L. Hofstetter, S. Csonka, J. Nygård, and C. Schönenberger. Cooper pair splitter realized in a two-quantum-dot Y-junction. *Nature (London)*, 461:960–963, 2009.

[14] A. Das, Y. Ronen, M. Heiblum, D. Mahalu, A. V. Kretinin, and H. Shtrikman. High-efficiency Cooper pair splitting demonstrated by two-particle conductance resonance and positive noise cross-correlation. *Nature communications*, 3(5):1165, 2012.

[15] G. Fülöp, S. d'Hollosy, A. Baumgartner, P. Makk, V. A. Guzenko, M. H. Madsen, J. Nygård, C. Schönenberger, and S. Csonka. Local electrical tuning of the nonlocal signals in a Cooper pair splitter. *Phys. Rev. B*, 90:235412, Dec 2014.

[16] W. Liang, M. Bockrath, and H. Park. Shell filling and exchange coupling in metallic single-walled carbon nanotubes. *Phys. Rev. Lett.*, 88:126801, Mar 2002.

[17] F. Kuemmeth, S. Ilani, D. C. Ralph, and P. L. McEuen. Coupling of spin and orbital motion of electrons in carbon nanotubes. *Nature (London)*, 452(7186):448–52, 2008.

[18] H. O. H. Churchill, F. Kuemmeth, J. W. Harlow, A. J. Bestwick, E. I. Rashba, K. Flensberg, C. H. Stwertka, T. Taychatanapat, S. K. Watson, and C. M. Marcus. Relaxation and dephasing in a two-electron $^{13}\mathbf{C}$ nanotube double quantum dot. *Phys. Rev. Lett.*, 102:166802, 2009.

[19] R. A. Lai, H. O. H. Churchill, and C. M. Marcus. g-tensor control in bent carbon nanotube quantum dots. *Phys. Rev. B*, 89:121303, 2014.

[20] R. S. Deacon, A. Oiwa, J. Sailer, S. Baba, Y. Kanai, K. Shibata, K. Hirakawa, and S. Tarucha. Cooper pair splitting in parallel quantum dot Josephson junctions. *Nature Communications*, 6:7446, July 2015.

[21] M. Hels. Toward entanglement detection. Master's thesis, University of Copenhagen, 2015.

[22] M. C. Hels, B. Braunecker, K. Grove-Rasmussen, and J. Nygård. Non-collinear Spin-Orbit Magnetic Fields in a Carbon Nanotube Double Quantum Dot. *Phys. Rev. Lett.*, 117:276802, Dec 2016.

[23] M. Kühnel, M. Overgaard, M. C. Hels, T. Vosch, B. W. Laursen, and K. Nørgaard. Sub-kelvin conductance measurements of large-area solid-state molecular junctions utilizing a high-quality reduced graphene oxide electrode. To be submitted.

[24] E. A. Laird, F. Kuemmeth, G. A. Steele, K. Grove-Rasmussen, J. Nygård, K. Flensberg, and L. P. Kouwenhoven. Quantum transport in carbon nanotubes. *Rev. Mod. Phys.*, 87(3):703–764, 2015.

[25] J.-C. Charlier, X. Blase, and S. Roche. Electronic and transport properties of nanotubes. *Rev. Mod. Phys.*, 79:677–732, May 2007.

[26] H. O. H. Churchill. *Quantum Dots in Gated Nanowires and Nanotubes*. PhD thesis, Harvard University, 2012.

[27] X. Zhou. *Carbon Nanotube Transistors, sensors, and beyond*. PhD thesis, Cornell University, 2008.

[28] J. Svensson and E. E. B. Campbell. Schottky barriers in carbon nanotube-metal contacts. *Journal of Applied Physics*, 110(11):111101–111101–16, December 2011.

[29] A. A. Reynoso and K. Flensberg. Dephasing and hyperfine interaction in carbon nanotube double quantum dots: The clean limit. *Physical Review B*, 84(20):1–20, 2011.

[30] R. Hanson, L. P. Kouwenhoven, J. R. Petta, S. Tarucha, and L. M. K. Vandersypen. Spins in few-electron quantum dots. *Rev. Mod. Phys.*, 79:1217–1265, Oct 2007.

[31] H. Bruus and K. Flensberg. *Many-body Quantum Theory in Condensed Matter Physics*. Oxford University Press, 2004.

[32] T. Ihn. *Semiconductor Nanostructures*. Oxford University Press, 2010.

[33] C. W. J. Beenakker. Theory of Coulomb-blockade oscillations in the conductance of a quantum dot. *Phys. Rev. B*, 44:1646–1656, Jul 1991.

[34] S. De Franceschi, S. Sasaki, J. M. Elzerman, W. G. van der Wiel, S. Tarucha, and L. P. Kouwenhoven. Electron Cotunneling in a Semiconductor Quantum Dot. *Phys. Rev. Lett.*, 86(5):878–881, Jan 2001.

[35] J. Kondo. Resistance Minimum in Dilute Magnetic Alloys. *Progress of Theoretical Physics*, 32(1):37–49, 1964.

[36] L. I. Glazman and M. E. Raikh. Resonant Kondo transparency of a barrier with quasilocal impurity states. *JETP Lett.*, 47:452, 1988.

[37] T. K. Ng and P. A. Lee. On-Site Coulomb Respulsion and Resonant Tunneling. *Phys. Rev. Lett.*, 61:1768, 1988.

[38] M. Pustilnik and L. I. Glazman. Conduction through a Quantum Dot near a Singlet-Triplet Transition. *Phys. Rev. Lett.*, 85:2993–2996, Oct 2000.

[39] W. Izumida, O. Sakai, and S. Tarucha. Tunneling through a Quantum Dot in Local Spin Singlet-Triplet Crossover Region with Kondo Effect. *Phys. Rev. Lett.*, 87:216803, Nov 2001.

[40] M. Tinkham. *Introduction to superconductivity.* Dover Publications, inc., 2004.

[41] L. P. Gor'kov. Exotic superconductors. *Physica Scripta*, 32(1):6, 1985.

[42] B. Sothmann, S. Weiss, M. Governale, and J. König. Unconventional superconductivity in double quantum dots. *Phys. Rev. B*, 90(22):220501, 2014.

[43] A. P. Mackenzie and M. Y. The superconductivity of Sr2RuO4 and the physics of spin-triplet pairing. *Rev. Mod. Phys.*, 75(2):657–712, 2003.

[44] C. Kittel. *Introduction to Solid State Physics.* John Wiley & Sons, Inc., 8th edition, 2005.

[45] R. Mattuck. *A Guide to Feynman Diagrams in the Many-body Problem.* Dover Books on Physics Series. Dover Publications, 1976.

[46] W. Chang, S. M. Albrecht, T. S. Jespersen, F. Kuemmeth, P. Krogstrup, J. Nygård, and C. M. Marcus. Hard gap in epitaxial semiconductor-superconductor nanowires. *Nature Nano.*, 10:232, 2015.

[47] D. H. Douglass. Magnetic Field Dependence of the Superconducting Energy Gap. *Phys. Rev. Lett.*, 6(7):346–348, 1961.

[48] J. O. Schindele. *Observation of Cooper Pair Splitting and Andreev Bound States in Carbon Nanotubes.* PhD thesis, University of Basel, 2014.

[49] P. Recher, E. V. Sukhorukov, and D. Loss. Andreev tunneling, Coulomb blockade, and resonant transport of nonlocal spin-entangled electrons. *Phys. Rev. B*, 63(16):165314, 2001.

[50] A. Einstein, B. Podolsky, and N. Rosen. Can Quantum-Mechanical Description of Physical Reality Be Considered Complete? *Phys. Rev.*, 47:777–780, May 1935.

[51] J. S. Bell. On the Einstein-Podolsky-Rosen Paradox. *Physics*, 1:195–200, 1964.

[52] A. Aspect, P. Grangier, and G. Roger. Experimental Realization of Einstein-Podolsky-Rosen-Bohm *Gedankenexperiment* : A New Violation of Bell's Inequalities. *Phys. Rev. Lett.*, 49:91–94, Jul 1982.

[53] R. Schleser, E. Ruh, T. Ihn, K. Ensslin, D. C. Driscoll, and A. C. Gossard. Time-resolved detection of individual electrons in a quantum dot. *Applied Physics Letters*, 85(11):2005–2007, 2004.

[54] M. A. Nielsen and I. L. Chuang. *Quantum Computation and Quantum Information*. Cambridge University Press, 2000.

[55] D. Beckmann, H. B. Weber, and H. v. Löhneysen. Evidence for Crossed Andreev Reflection in Superconductor-Ferromagnet Hybrid Structures. *Phys. Rev. Lett.*, 93:197003, Nov 2004.

[56] S. Russo, M. Kroug, T. M. Klapwijk, and A. F. Morpurgo. Experimental Observation of Bias-Dependent Nonlocal Andreev Reflection. *Phys. Rev. Lett.*, 95:027002, Jul 2005.

[57] L. Hofstetter, S. Csonka, A. Baumgartner, G. Fülöp, S. d'Hollosy, J. Nygård, and C. Schönenberger. Finite-Bias Cooper Pair Splitting. *Phys. Rev. Lett.*, 107:136801, Sep 2011.

[58] P. Burset, W. J. Herrera, and A. Levy Yeyati. Microscopic theory of Cooper pair beam splitters based on carbon nanotubes. *Phys. Rev. B*, 84:115448, 2011.

[59] J.-D. Pillet. *Tunneling spectroscopy of the Andreev Bound States in a Carbon Nanotube*. PhD thesis, SPEC - CEA Saclay, 2011.

[60] S. Kim, H.-J. Kim, H. R. Lee, J.-H. Song, S. N. Yi, and D. H. Ha. Oxygen plasma effects on the electrical conductance of single-walled carbon nanotube bundles. *Journal of Physics D: Applied Physics*, 43(30):305402, 2010.

[61] W. Kim, H. C. Choi, M. Shim, Y. Li, D. Wang, and H. Dai. Synthesis of ultralong and high percentage of semiconducting single-walled carbon nanotubes. *Nano Letters*, 2(7):703–708, 2002.

[62] N. Y. Yao, C. P. Moca, I. Weymann, J. D. Sau, M. D. Lukin, E. A. Demler, and G. Zaránd. Phase diagram and excitations of a shiba molecule. *Phys. Rev. B*, 90:241108, Dec 2014.

[63] D. R. Lide. *CRC Handbook of Chemistry and Physics, 89th Edition (Internet Version)*. CRC Press/Taylor and Francis, 2009.

[64] J. Samm, J. Gramich, A. Baumgartner, M. Weiss, and C. Schönenberger. Optimized fabrication and characterization of carbon nanotube spin valves. *Journal of Applied Physics*, 115(17):174309, 2014.

[65] J. B. Gramich. *Andreev and Spin Transport in Carbon Nanotube Quantum Dot Hybrid Devices*. PhD thesis, University of Basel, 2016.

[66] S.-W. Lee, M. M., H. T., M. M., and H. C. Suppression of resist contamination during photolithography on carbon nanomaterials by a sacrificial layer. *Carbon*, 66:295 – 301, 2014.

[67] G. M. King, G. Schürmann, D. Branton, and J. A. Golovchenko. Nanometer patterning with ice. *Nano Letters*, 5(6):1157–1160, 2005.

[68] A. Han, D. Vlassarev, J. Wang, J. A. Golovchenko, and D. Branton. Ice lithography for nanodevices. *Nano Letters*, 10(12):5056–5059, 2010.

[69] A. Han, A. Kuan, J. Golovchenko, and D. Branton. Nanopatterning on nonplanar and fragile substrates with ice resists. *Nano Letters*, 12(2):1018–1021, 2012.

[70] A. Roch, M. Greifzu, E. R. Talens, L. Stepien, T. Roch, J. Hege, N. V. Nong, T. Schmiel, I. Dani, C. Leyens, O. Jost, and A. Leson. Ambient effects on the electrical conductivity of carbon nanotubes. *Carbon*, 95(Supplement C):347 – 353, 2015.

[71] J. Waissman, M. Honig, S. Pecker, A. Benyamini, A. Hamo, and S. Ilani. Realization of pristine and locally tunable one-dimensional electron systems in carbon nanotubes. *Nature Nanotechnology*, 8:569–574, August 2013.

[72] Takis Kontos. personal communication.

[73] D. Wei, H.-O. Li, G. Cao, G. Luo, Z.-X. Zheng, T. Tu, M. Xiao, G.-C. Guo, H.-W. Jiang, and T. Ping. Tuning inter-dot tunnel coupling of an etched graphene double quantum dot by adjacent metal gates. *Scientific reports*, 3:3175, 11 2013.

[74] S. Baer and K. Ensslin. *Transport Spectroscopy of Confined Fractional Quantum Hall Systems*. Springer Series in Solid-State Sciences. Springer International Publishing, 2015.

[75] K. Flensberg and C. M. Marcus. Bends in nanotubes allow electric spin control and coupling. *Phys. Rev. B*, 81:195418, 2010.

[76] F. Pei, E. A. Laird, G. A. Steele, and L. P. Kouwenhoven. Valley-spin blockade and spin resonance in carbon nanotubes. *Nature Nano.*, 7(10):630–4, 2012.

[77] E. A. Laird, F. Pei, and L. P. Kouwenhoven. A valley-spin qubit in a carbon nanotube. *Nature Nano.*, 8:565–568, 2013.

[78] F. Mazza, B. Braunecker, P. Recher, and A. Levy Yeyati. Spin filtering and entanglement detection due to spin-orbit interaction in carbon nanotube cross-junctions. *Phys. Rev. B*, 88(19):195403, 2013.

[79] G. A. Steele, A. K. Hüttel, B. Witkamp, M. Poot, H. B. Meerwaldt, L. P. Kouwenhoven, and H. S. J. van der Zant. Strong coupling between single-electron tunneling and nanomechanical motion. *Science*, 325(5944):1103–1107, 2009.

[80] A. Benyamini, A. Hamo, S. V. Kusminskiy, F. von Oppen, and S. Ilani. Real-space tailoring of the electron-phonon coupling in ultraclean nanotube mechanical resonators. *Nature Phys.*, 10:151–156, February 2014.

[81] T. S. Jespersen, K. Grove-Rasmussen, J. Paaske, K. Muraki, T. Fujisawa, J. Nygård, and K. Flensberg. Gate-dependent spin-orbit coupling in multielectron carbon nanotubes. *Nature Phys.*, 7:348–353, 2011.

[82] J. Klinovaja, M. J. Schmidt, B. Braunecker, and D. Loss. Carbon nanotubes in electric and magnetic fields. *Phys. Rev. B*, 84:085452, 2011.

[83] D. V. Bulaev, B. Trauzettel, and D. Loss. Spin-orbit interaction and anomalous spin relaxation in carbon nanotube quantum dots. *Phys. Rev. B*, 77:235301, 2008.

[84] D. H. Cobden and J. Nygård. Shell filling in closed single-wall carbon nanotube quantum dots. *Phys. Rev. Lett.*, 89:046803, Jul 2002.

[85] S. Sapmaz, P. Jarillo-Herrero, J. Kong, C. Dekker, L. P. Kouwenhoven, and H. S. J. van der Zant. Electronic excitation spectrum of metallic carbon nanotubes. *Phys. Rev. B*, 71:153402, Apr 2005.

[86] K. Grove-Rasmussen, S. Grap, J. Paaske, K. Flensberg, S. Andergassen, V. Meden, H. I. Jørgensen, K. Muraki, and T. Fujisawa. Magnetic-field dependence of tunnel couplings in carbon nanotube quantum dots. *Phys. Rev. Lett.*, 108:176802, Apr 2012.

[87] J. Klinovaja, M. J. Schmidt, B. Braunecker, and D. Loss. Helical Modes in Carbon Nanotubes Generated by Strong Electric Fields. *Phys. Rev. Lett.*, 106:156809, 2011.

[88] S. Weiss, E. I. Rashba, F. Kuemmeth, H. O. H. Churchill, and K. Flensberg. Spin-orbit effects in carbon-nanotube double quantum dots. *Phys. Rev. B*, 82:165427, 2010.

[89] J. Kong, H. T. Soh, A. M. Cassell, C. F. Quate, and H. Dai. Synthesis of individual single-walled carbon nanotubes on patterned silicon wafers. *Nature (London)*, 395:878–881, 1998.

[90] J. P. Cleuziou, N. V. N'Guyen, S. Florens, and W. Wernsdorfer. Interplay of the Kondo Effect and Strong Spin-Orbit Coupling in Multihole Ultraclean Carbon Nanotubes. *Phys. Rev. Lett.*, 111:136803, 2013.

[91] D. R. Schmid, S. Smirnov, M. Margańska, A. Dirnaichner, P. L. Stiller, M. Grifoni, A. K. Hüttel, and C. Strunk. Broken SU(4) symmetry in a kondo-correlated carbon nanotube. *Phys. Rev. B*, 91:155435, 2015.

[92] F. H. L. Koppens, C. Buizert, K. J. Tielrooij, I. T. Vink, K. C. Nowack, T. Meunier, L. P. Kouwenhoven, and L. M. K. Vandersypen. Driven coherent oscillations of a single electron spin in a quantum dot. *Nature (London)*, 442:766, 2006.

[93] J. R. Petta, A. C. Johnson, J. M. Taylor, E. A. Laird, A. Yacoby, M. D. Lukin, C. M. Marcus, M. P. Hanson, and A. C. Gossard. Coherent Manipulation of Coupled Electron Spins in Semiconductor Quantum Dots. *Science*, 309:2180–2184, 2005.

[94] M. Pioro-Ladrière, T. Obata, Y. Tokura, Y.-S. Shin, T. Kubo, K. Yoshida, T. Taniyama, and S. Tarucha. Electrically driven single-electron spin resonance in a slanting Zeeman field. *Nature Phys.*, 4:776–779, 2008.

[95] M. Kjaergaard, K. Wölms, and K. Flensberg. Erratum: Majorana fermions in superconducting nanowires without spin-orbit coupling [Phys. Rev. B 85, 020503(R) (2012)]. *Phys. Rev. Lett.*, 90(5):059901, 2014.

[96] A. D. Crisan, S. Datta, J. J. Viennot, M. R. Delbecq, A. Cottet, and T. Kontos. Harnessing spin precession with dissipation. *Nature Comm.*, 7:10451, 2016.

[97] A. N. Pasupathy, R. C. Bialczak, J. Martinek, J. E. Grose, L. A. K. Donev, P. L. McEuen, and D. C. Ralph. The Kondo Effect in the Presence of Ferromagnetism. *Science*, 306:86–89, 2004.

[98] J. R. Hauptmann, J. Paaske, and P. E. Lindelof. Electric-field-controlled spin reversal in a quantum dot with ferromagnetic contacts. *Nature Phys.*, 4:373–376, 2008.

[99] G. Salis, Y. Kato, K. Ensslin, D. C. Driscoll, A. C. Gossard, and D. D. Awschalom. Electrical control of spin coherence in semiconductor nanostructures. *Nature (London)*, 414(6864):619–22, 2001.

[100] K. C. Nowack, F. H. L. Koppens, Y. V. Nazarov, and L. M. K. Vandersypen. Coherent Control of a Single Electron Spin with Electric Fields. *Science*, 318(5855):1430–1433, 2007.

[101] S. Nadj-Perge, S. M. Frolov, E. P. A. M. Bakkers, and L. P. Kouwenhoven. Spin-orbit qubit in a semiconductor nanowire. *Nature (London)*, 468(7327):1084–1087, 2010.

[102] M. Leijnse and K. Flensberg. Parity qubits and poor man's Majorana bound states in double quantum dots. *Phys. Rev. B*, 86(13):134528, 2012.

[103] W. Izumida, K. Sato, and R. Saito. Spin-Orbit Interaction in Single Wall Carbon Nanotubes: Symmetry Adapted Tight-Binding Calculation and Effective Model Analysis. *J. Phys. Soc. Jpn.*, 78(7):074707, 2009.

[104] T. Ando. Spin-Orbit Interaction in Carbon Nanotubes. *J. Phys. Soc. Jpn.*, 69(6):1757–1763, 2000.

[105] G. Széchenyi and A. Pályi. Shape-sensitive Pauli blockade in a bent carbon nanotube. *Phys. Rev. B*, 91:045431, 2015.

[106] Y. Li, S. C. Benjamin, G. A. D. Briggs, and E. A. Laird. Electrically driven spin resonance in a bent disordered carbon nanotube. *Phys. Rev. B*, 90:195440, 2014.

[107] J. S. Lim, R. López, and R. Aguado. Josephson Current in Carbon Nanotubes with Spin-Orbit Interaction. *Phys. Rev. Lett.*, 107:196801, 2011.

[108] R. I. Shekhter, O. Entin-Wohlman, M. Jonson, and A. Aharony. Rashba Splitting of Cooper Pairs. *Phys. Rev. Lett.*, 116:217001, 2016.

[109] The data underpinning the results in this work can be found at. `http://dx.doi.org/10.17630/df2aa84f-36f2-4c1f-b00c-34e102dcee1e`.

[110] A. Jellinggaard, K. Grove-Rasmussen, M. H. Madsen, and J. Nygård. Tuning Yu-Shiba-Rusinov states in a quantum dot. *Phys. Rev. B*, 94:064520, Aug 2016.

[111] G. Fülöp. *Cooper pair splitting in indium arsenide nanowires*. PhD thesis, Budapest University of Technology and Economics, 2016.

[112] J. Schindele, A. Baumgartner, R. Maurand, M. Weiss, and C. Schönenberger. Nonlocal spectroscopy of Andreev bound states. *Phys. Rev. B*, 89:045422, Jan 2014.

[113] M. Steinacher. *Low noise/high stability I to V converter SP 983*. Physics Basel.

[114] W. Liang, M. Bockrath, D. Bozovic, J. H. Hafner, M. Tinkham, and H. Park. Fabry - Perot interference in a nanotube electron waveguide. *Nature (London)*, 411(6838):665–669, 2001.

[115] S. Moriyama, T. Fuse, M. Suzuki, Y. Aoyagi, and K. Ishibashi. Four-electron shell structures and an interacting two-electron system in carbon-nanotube quantum dots. *Phys. Rev. Lett.*, 94(18):1–4, 2005.

[116] D. Griffiths. *Introduction to Quantum Mechanics*. Pearson international edition. Pearson Prentice Hall, 2005.

[117] A. Jellinggaard. *Quantum Dots Coupled to a Superconductor*. PhD thesis, University of Copenhagen, 2016.

[118] D. R. Hines, S. Mezhenny, M. Breban, E. D. Williams, V. W. Ballarotto, G. Esen, A. Southard, and M. S. Fuhrer. Nanotransfer printing of organic and carbon nanotube thin-film transistors on plastic substrates. *Applied Physics Letters*, 86(16):163101, April 2005.

[119] V. K. Sangwan, V. W. Ballarotto, M. S. Fuhrer, and E. D. Williams. Facile fabrication of suspended as-grown carbon nanotube devices. *Applied Physics Letters*, 93(11):113112, 2008.

[120] J. Gramich, A. Baumgartner, M. Muoth, C. Hierold, and C. Schönenberger. Fork stamping of pristine carbon nanotubes onto ferromagnetic contacts for spin-valve devices. *Physica Status Solidi B Basic Research*, 252:2496–2502, November 2015.

[121] M. Jung, J. Schindele, S. Nau, M. Weiss, A. Baumgartner, and C. Schönenberger. Ultraclean single, double, and triple carbon nanotube quantum dots with recessed re bottom gates. *Nano Letters*, 13(9):4522–4526, 2013.

[122] T. W. Ebbesen. Carbon Nanotubes. *Physics Today*, 49:26–32, June 1996.

[123] C. Dekker. Carbon nanotubes as molecular quantum wires. *Physics Today*, 52:22–28, May 1999.

[124] C. Qiu, Z. Zhang, M. Xiao, Y. Yang, D. Zhong, and L.-M. Peng. Scaling carbon nanotube complementary transistors to 5-nm gate lengths. *Science*, 355(6322):271–276, 2017.

[125] P. Krogstrup, H. I. Jørgensen, E. Johnson, M. H. Madsen, C. B. Sørensen, A. F. i Morral, M. Aagesen, J. Nygård, and F. Glas. Advances in the theory of iii–v nanowire growth dynamics. *Journal of Physics D: Applied Physics*, 46(31):313001, 2013.

[126] P. Krogstrup, N. L. B. Ziino, W. Chang, S. M. Albrecht, M. H. Madsen, E. Johnson, J. Nygård, C. M. Marcus, and T. S. Jespersen. Epitaxy of semiconductor-superconductor nanowires. *Nature Materials*, 14:400–406, April 2015.

[127] V. Mourik, K. Zuo, S. M. Frolov, S. R. Plissard, E. P. A. M. Bakkers, and L. P. Kouwenhoven. Signatures of majorana fermions in hybrid superconductor-semiconductor nanowire devices. *Science*, 336(6084):1003–1007, 2012.

[128] M. T. Deng, S. Vaitiekenas, E. B. Hansen, J. Danon, M. Leijnse, K. Flensberg, J. Nygård, P. Krogstrup, and C. M. Marcus. Majorana bound state in a coupled quantum-dot hybrid-nanowire system. *Science*, 354(6319):1557–1562, 2016.

[129] K. Maehashi, Y. Ohno, K. Inoue, and K. Matsumoto. Chirality selection of single-walled carbon nanotubes by laser resonance chirality selection method. *Applied Physics Letters*, 85(6):858–860, 2004.

[130] Y. Chen and J. Zhang. Chemical vapor deposition growth of single-walled carbon nanotubes with controlled structures for nanodevice applications. *Accounts of Chemical Research*, 47(8):2273–2281, 2014.

[131] H. Wang, Y. Yuan, L. Wei, K. Goh, D. Yu, and Y. Chen. Catalysts for chirality selective synthesis of single-walled carbon nanotubes. *Carbon*, 81(Supplement C):1 – 19, 2015.

[132] A. J. Page, Y. Ohta, S. Irle, and K. Morokuma. Mechanisms of single-walled carbon nanotube nucleation, growth, and healing determined using qm/md methods. *Accounts of Chemical Research*, 43(10):1375–1385, 2010.

[133] J.-P. Tessonnier and D. S. Su. Recent progress on the growth mechanism of carbon nanotubes: A review. *ChemSusChem*, 4(7):824–847, 2011.

[134] V. Jourdain and C. Bichara. Current understanding of the growth of carbon nanotubes in catalytic chemical vapour deposition. *Carbon*, 58(Supplement C):2 – 39, 2013.

[135] F. Domínguez and A. L. Yeyati. Quantum interference in a Cooper pair splitter: The three sites model. *Physica E Low-Dimensional Systems and Nanostructures*, 75:322–329, January 2016.

[136] S. Kawabata. Test of bell's inequality using the spin filter effect in ferromagnetic semiconductor microstructures. *Journal of the Physical Society of Japan*, 70(5):1210–1213, 2001.

[137] N. M. Chtchelkatchev, G. Blatter, G. B. Lesovik, and T. Martin. Bell inequalities and entanglement in solid-state devices. *Phys. Rev. B*, 66(16):161320, October 2002.

[138] W. Kłobus, A. Grudka, A. Baumgartner, D. Tomaszewski, C. Schönenberger, and J. Martinek. Entanglement witnessing and quantum cryptography with nonideal ferromagnetic detectors. *Phys. Rev. B*, 89:125404, Mar 2014.

[139] P. Samuelsson, E. V. Sukhorukov, and M. Büttiker. Orbital entanglement and violation of bell inequalities in mesoscopic conductors. *Phys. Rev. Lett.*, 91:157002, Oct 2003.

[140] C. W. J. Beenakker, C. Emary, M. Kindermann, and J. L. van Velsen. Proposal for production and detection of entangled electron-hole pairs in a degenerate electron gas. *Phys. Rev. Lett.*, 91:147901, Oct 2003.

[141] O. Sauret, T. Martin, and D. Feinberg. Spin-current noise and bell inequalities in a realistic superconductor-quantum dot entangler. *Phys. Rev. B*, 72:024544, Jul 2005.

[142] A. Schroer, B. Braunecker, A. Levy Yeyati, and P. Recher. Detection of spin entanglement via spin-charge separation in crossed tomonaga-luttinger liquids. *Phys. Rev. Lett.*, 113:266401, Dec 2014.

[143] M. Leijnse and K. Flensberg. Coupling spin qubits via superconductors. *Phys. Rev. Lett.*, 111:060501, Aug 2013.

[144] A. Yazdani, B. A. Jones, C. P. Lutz, M. F. Crommie, and D. M. Eigler. Probing the local effects of magnetic impurities on superconductivity. *Science*, 275(5307):1767–1770, 1997.

[145] A. Y. Kitaev. 6. QUANTUM COMPUTING: Unpaired Majorana fermions in quantum wires. *Physics Uspekhi*, 44:131, October 2001.

[146] F. Pientka, L. I. Glazman, and F. von Oppen. Topological superconducting phase in helical shiba chains. *Phys. Rev. B*, 88:155420, Oct 2013.

[147] S. Nadj-Perge, I. K. Drozdov, J. Li, H. Chen, S. Jeon, J. Seo, A. H. MacDonald, B. A. Bernevig, and A. Yazdani. Observation of majorana fermions in ferromagnetic atomic chains on a superconductor. *Science*, 346(6209):602–607, 2014.

[148] Z. Su, A. B. Tacla, M. Hocevar, D. Car, S. R. Plissard, E. P. A. M. Bakkers, A. J. Daley, D. Pekker, and S. M. Frolov. Andreev Molecules in Semiconductor Nanowire Double Quantum Dots. *ArXiv e-prints*, November 2016.

[149] B. W. Smith and D. E. Luzzi. Electron irradiation effects in single wall carbon nanotubes. *Journal of Applied Physics*, 90(7):3509–3515, 2001.

[150] G. A. Steele, G. Gotz, and L. P. Kouwenhoven. Tunable few-electron double quantum dots and Klein tunnelling in ultraclean carbon nanotubes. *Nature Nano.*, 4(6):363–367, 2009.

[151] U. Schmid. The impact of thermal annealing and adhesion film thickness on the resistivity and the agglomeration behavior of titanium/-platinum thin films. *Journal of Applied Physics*, 103(5):054902, 2008.

[152] E. J. H. Lee, X. Jiang, M. Houzet, R. Aguado, C. M. Lieber, and S. De Franceschi. Spin-resolved Andreev levels and parity crossings in hybrid superconductor-semiconductor nanostructures. *Nature Nano.*, 9(1):79–84, 2014.

[153] Stanford Research Systems, 1290-D Reamwood Avenue, Sunnyvale, California 94089. *MODEL SR830 DSP Lock-In Amplifier*, 2.5 edition, 2011.

[154] M. Spiegel, S. Lipschutz, and J. Liu. *Schaum's Outline of Mathematical Handbook of Formulas and Tables, 3ed.* Schaum's Outline Series. McGraw-Hill Education, 2008.